NASA/TM–2016-219352
NESC-RP-14-00962

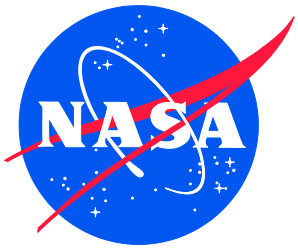

Investigation of Unsteady Pressure-Sensitive Paint (uPSP) and a Dynamic Loads Balance to Predict Launch Vehicle Buffet Environments

David M. Schuster/NESC
Langley Research Center, Hampton, Virginia

Jayanta Panda, James C. Ross, Nettie H. Roozeboom, Nathan J. Burnside, Christina L. Ngo, and Hiro Kumagai
Ames Research Center, Moffett Field, California

Marvin Sellers
Aerospace Testing Alliance, Arnold Air Force Base, Tennessee

Jessica M. Powell
Johnson Space Center, Houston, Texas

Martin K. Sekula and David J. Piatak
Langley Research Center, Hampton, Virginia

November 2016

NASA STI Program . . . in Profile

Since its founding, NASA has been dedicated to the advancement of aeronautics and space science. The NASA scientific and technical information (STI) program plays a key part in helping NASA maintain this important role.

The NASA STI program operates under the auspices of the Agency Chief Information Officer. It collects, organizes, provides for archiving, and disseminates NASA's STI. The NASA STI program provides access to the NTRS Registered and its public interface, the NASA Technical Reports Server, thus providing one of the largest collections of aeronautical and space science STI in the world. Results are published in both non-NASA channels and by NASA in the NASA STI Report Series, which includes the following report types:

- TECHNICAL PUBLICATION. Reports of completed research or a major significant phase of research that present the results of NASA Programs and include extensive data or theoretical analysis. Includes compilations of significant scientific and technical data and information deemed to be of continuing reference value. NASA counter-part of peer-reviewed formal professional papers but has less stringent limitations on manuscript length and extent of graphic presentations.

- TECHNICAL MEMORANDUM. Scientific and technical findings that are preliminary or of specialized interest, e.g., quick release reports, working papers, and bibliographies that contain minimal annotation. Does not contain extensive analysis.

- CONTRACTOR REPORT. Scientific and technical findings by NASA-sponsored contractors and grantees.

- CONFERENCE PUBLICATION. Collected papers from scientific and technical conferences, symposia, seminars, or other meetings sponsored or co-sponsored by NASA.

- SPECIAL PUBLICATION. Scientific, technical, or historical information from NASA programs, projects, and missions, often concerned with subjects having substantial public interest.

- TECHNICAL TRANSLATION. English-language translations of foreign scientific and technical material pertinent to NASA's mission.

Specialized services also include organizing and publishing research results, distributing specialized research announcements and feeds, providing information desk and personal search support, and enabling data exchange services.

For more information about the NASA STI program, see the following:

- Access the NASA STI program home page at *http://www.sti.nasa.gov*

- E-mail your question to help@sti.nasa.gov

- Phone the NASA STI Information Desk at 757-864-9658

- Write to:
  NASA STI Information Desk
  Mail Stop 148
  NASA Langley Research Center
  Hampton, VA 23681-2199

NASA/TM–2016-219352
NESC-RP-14-00962

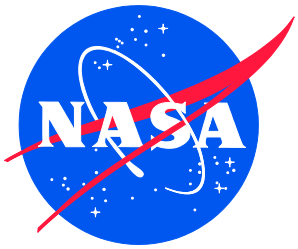

Investigation of Unsteady Pressure-Sensitive Paint (uPSP) and a Dynamic Loads Balance to Predict Launch Vehicle Buffet Environments

David M. Schuster/NESC
Langley Research Center, Hampton, Virginia

Jayanta Panda, James C. Ross, Nettie H. Roozeboom, Nathan J. Burnside, Christina L. Ngo, and Hiro Kumagai
Ames Research Center, Moffett Field, California

Marvin Sellers
Aerospace Testing Alliance, Arnold Air Force Base, Tennessee

Jessica M. Powell
Johnson Space Center, Houston, Texas

Martin K. Sekula and David J. Piatak
Langley Research Center, Hampton, Virginia

National Aeronautics and
Space Administration

Langley Research Center
Hampton, Virginia 23681-2199

November 2016

Available from:

NASA STI Program / Mail Stop 148
NASA Langley Research Center
Hampton, VA 23681-2199
Fax: 757-864-6500

Investigation of Unsteady Pressure-Sensitive Paint (uPSP) and a Dynamic Loads Balance to Predict Launch Vehicle Buffet Environments

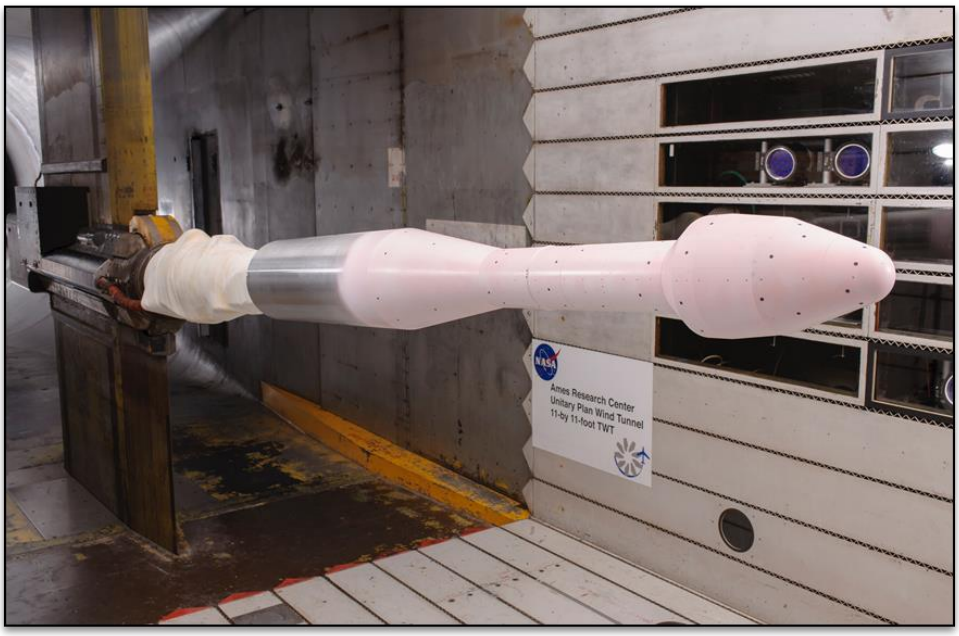

July 28, 2016

Report Approval and Revision History

NOTE: This document was approved at the July 28, 2016, NRB. This document was submitted to the NESC Director on September 29, 2016, for configuration control.

Approved:	*Original Signature on File (MK)*	10/3/16
	NESC Director	Date

Version	Description of Revision	Office of Primary Responsibility	Effective Date
1.0	Initial Release	Dr. David M. Schuster, NASA Technical Fellow for Aerosciences, LaRC	7/28/16

Table of Contents

List of Figures

List of Tables

1.0 Notification and Authorization

This NASA Engineering and Safety Center (NESC) assessment investigated innovative test techniques for acquiring launch vehicle buffet data. Presently, buffet environment data for launch vehicles are acquired through wind tunnel testing of models on the order of 400 unsteady pressure transducers. Even with this apparently large number of sensors, unless the coherence of the pressure signals in the axial and azimuthal directions is accounted for, the resulting sensor density may not be sufficient to provide unsteady integrated loads on the vehicle. Also, the accuracy of the current coherence correction schemes has not been fully verified. Having a set of pressure data of sufficient sensor density to allow accurate estimates of the load without needing coherence corrections allows a comparison of the loads estimated using coherence corrections applied to a subset of the pressure data. Load estimates using sparse sensors have been shown to overestimate the buffet loads. This can result in additional structural weight to cover these conservative environments. This assessment used a combination of unsteady pressure-sensitive paint (uPSP) and a dynamic loads balance to investigate the potential of these innovative and emerging test techniques to more accurately predict launch vehicle buffet environments.

Dr. David Schuster, NASA Technical Fellow for Aerosciences, served as the NESC assessment lead. The key stakeholders for this assessment are the Space Launch System (SLS) Aerosciences group, SLS Loads and Dynamics group, and the NASA Aeronautics Test Program.

2.0 Signature Page

Submitted by:

Team Signature Page Added – 10/17/16

Dr. David M. Schuster Date

Significant Contributors:

Dr. Jayanta Panda Date	Dr. James C. Ross Date
Mr. Marvin Sellers Date	Ms. Nettie H. Roozeboom Date
Mr. Nathan J. Burnside Date	Dr. Martin K. Sekula Date
Mr. David J. Piatak Date	Ms. Christina L. Ngo Date
Ms. Jessica M. Powell Date	Dr. Hiro Kumagai Date

Signatories declare the findings, observations, and NESC recommendations compiled in the report are factually based from data extracted from program/project documents, contractor reports, and open literature, and/or generated from independently conducted tests, analyses, and inspections.

3.0 Team List

Name	Discipline	Organization
Core Team		
David Schuster	NESC Lead	LaRC
James Ross	Technical Co-Lead	ARC
Jayanta Panda	Technical Co-Lead	ARC
Marvin Sellers	Unsteady PSP Lead	Aerospace Testing Alliance
John LaNeave	MTSO Program Analyst	LaRC
Nettie Roozeboom	Time Averaged PSP Lead	ARC
James Bell	PSP	ARC
Nathan Burnside	Kulite® Measurement Lead	ARC
Christina Ngo	Unsteady Balance Lead	ARC
Hiroyuki Kumagai	On-board Digitizer	ARC
Scott Christa	On-board Digitizer	ARC
David Piatak	Buffet	LaRC
Martin Sekula	Buffet	LaRC
Russ Rausch	Buffet	LaRC
Darren Reed	Buffet	MSFC
Andy Herron	Buffet	MSFC
Bil Kleb	Aerosciences	LaRC
Jessie Powell	Unsteady Balance	JSC
Kenneth Johnson	Statistics	MSFC
Administrative Support		
Pamela Sparks	Project Coordinator	LaRC/AMA
Linda Burgess	Planning and Control Analyst	LaRC/AMA
Phillip Wirtz	Technical Writer	LaRC/NGC

4.0 Executive Summary

This NESC assessment examined the accuracy of estimating buffet loads on in-line launch vehicles without booster attachments using sparse unsteady pressure measurements. The buffet loads computed using sparse sensor data were compared with estimates derived using measurements with much higher spatial resolution. The current method for estimating launch vehicle buffet loads is through wind tunnel testing of models with approximately 400 unsteady pressure transducers. Even with this relatively large number of sensors, the coverage can be insufficient to provide reliable integrated unsteady loads on vehicles. In general, sparse sensor spacing requires the use of coherence-length-based corrections in the azimuthal and axial directions to integrate the unsteady pressures and obtain reasonable estimates of the buffet loads. Coherence corrections have been used to estimate buffet loads for a variety of launch vehicles with the assumption methodology results in reasonably conservative loads. For the Space Launch System (SLS), the first estimates of buffet loads exceeded the limits of the vehicle structure, so additional tests with higher sensor density were conducted to better define the buffet loads and possibly avoid expensive modifications to the vehicle design. Without the additional tests and improvements to the coherence-length analysis methods, there would have been significant impacts to the vehicle weight, cost, and schedule. If the load estimates turn out to be too low, there is significant risk of structural failure of the vehicle.

This assessment used a combination of unsteady pressure-sensitive paint (uPSP), unsteady pressure transducers, and a dynamic force and moment balance to investigate the integration schemes used with limited unsteady pressure data by comparing them with direct integration of extremely dense fluctuating pressure measurements. An outfall of the assessment was to evaluate the potential of using the emerging uPSP technique in a production test environment for future launch vehicles. *The results show that modifications to the current technique can improve the accuracy of buffet estimates.* More importantly, the uPSP worked remarkably well and, with improvements to the frequency response, sensitivity, and productivity, will provide an enhanced method for measuring wind tunnel buffet forcing functions (BFFs).

5.0 Introduction

Aerodynamic buffet on launch vehicles is a recurring problem for vehicle designers. Structural analyses require accurate buffet forcing function (BFF) measurements consisting of time-correlated and time-accurate section loads along the entire vehicle length.

Measuring BFFs on a wind tunnel model is difficult for a variety of reasons, notably:

- The required number of sensors is not well defined in the literature. Generally, far fewer sensors than optimal are used to estimate BFF, particularly for configurations like the Space Launch System (SLS) that have strap-on boosters requiring increased measurement density to obtain accurate load estimates.
- Unsteady pressure sensors are expensive and can require long lead times when purchased in the necessary quantities (e.g., hundreds for a given wind tunnel model).
- Buffet is configuration sensitive, and early design configurations may not represent the eventual vehicle geometry, which can increase BFF uncertainty.

The SLS most recently suffered from overly conservative BFF estimates. The initial estimates, based on best practice wind tunnel testing, indicated potentially excessive low-frequency buffet. Subsequent wind tunnel tests were performed with additional pressure sensors and proposed geometry modifications to reduce the buffet loading showed. These follow-on tests showed that the high BFF estimates resulted from too-sparse pressure measurements and a simplified booster attachment. Subsequent BFF estimates based on the new wind tunnel data with additional instrumentation indicated lower-amplitude buffet load than the earlier results and no need for the proposed geometric modifications. More accurate buffet data methodology would make this kind of iterative effort less likely.

Computational fluid dynamics (CFD) is potentially capable of producing these environments but is currently too computationally intensive and not fully validated for unsteady loads. Until CFD is proven accurate and dependable for estimating buffet loads, NASA and the aerospace industry need a defendable, reliable method to estimate BFFs from the limited unsteady pressure data available from wind tunnel testing.

There is also a significant need for a new wind tunnel-based measurement capability to estimate buffet loading to supplement the use of unsteady transducers. There has been a tremendous development in the ability of unsteady pressure-sensitive paint (uPSP) to measure unsteady pressures. The state of the art indicates that full-surface measurements are possible for simple geometries at frequencies to about 5 kHz.

This assessment was undertaken to address the shortcomings in buffet measurement and prediction by developing a comprehensive set of unsteady pressure measurements on a simple launch vehicle geometry using uPSP as the primary instrumentation and assess its accuracy using unsteady pressure transducers. The measurements show that the current practice of integrating a

sparse distribution of unsteady pressure measurements usually results in over-conservative BFF estimates. There are some instances where the estimated loads are lower than the full-resolution integrations produce. Further refinements of the coherence-length corrections may improve the accuracy sufficiently for future buffet testing and data analysis. Finally, the uPSP measurements were sufficiently accurate for the simplified launch vehicle model to provide reliable BFF estimates. Continued development of the uPSP technique should improve the accuracy-response, making this an attractive measurement technique for determining launch vehicle BFF.

6.0 Test Objectives

There were three specific test objectives: (1) examine the current buffet measurement technique to identify shortcomings and improvements, (2) verify the accuracy of uPSP for measuring unsteady pressures in the appropriate frequency range for launch vehicle buffet, and (3) provide a comprehensive set of unsteady pressure data to validate CFD techniques for estimating BFF.

The geometrically simple model was instrumented with uPSP, 213 Kulite® unsteady pressure transducers, static pressure taps, and a force and moment balance. The Kulite® and static pressure measurements were used to verify the PSP measurements. Figure 6.0-1 shows the model mounted in the 11- by 11-Foot Transonic Wind Tunnel. The model was copied from the Model 11 geometry tested by Coe and Nute [ref. 1]. It is a simple axisymmetric launch vehicle shape with a payload section larger than the second-stage diameter. This shape ensures a separated flow region downstream of the payload. The first-stage diameter is larger than the second stage, providing a second pressure gradient that affects the flow reattachment downstream of the payload fairing. These flow features are found on many launch vehicles, and this geometry is intentionally simple to facilitate the BFF computations and CFD validation work.

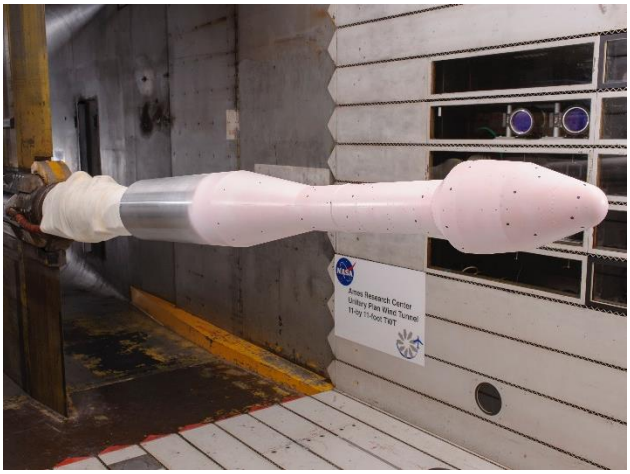

Figure 6.0-1. Model Mounted in the 11- by 11-Foot Transonic Test Section

Processing of the unsteady pressure data from either the transducers of the uPSP was performed using the same algorithms to ensure the comparisons are all valid. The accompanying CFD will also incorporate the common processing methods.

7.0 Model Design and Fabrication

7.1 Model Configuration

The model geometry definition, show in Figure 7.1-1, was taken from Coe and Nute [ref. 1]. Force measurements were made on the model's blue-shaded section, which was the model skin mounted to an internal balance with labyrinth seals between the model's forward and aft ends and the nonmetric sections. The effect of a protuberance on the unsteady pressures was studied using two bolt-on flanges as shown in Figure 7.1-2. These faired flanges are commonly used to connect adjacent sections of a launch vehicle and are known to cause high local aeroacoustic loads, which could affect the buffet loads.

The model's shaded section in Figures 7.1-1 and 7.1-2 is the metric portion of the model skin. This section was chosen because it encompasses the separated flow region and extends into the reattachment zone. The unsteady aerodynamic loads on this section were measured directly with a 4-component internal balance. The uPSP data were integrated over this region for direct comparison. The pressures measured using the rings of Kulite® transducers on the metric section were integrated using the current best practice for estimating BFF for comparisons with the other two measurements. The inertial loads acting on the internal balance due to model oscillation were estimated from 4 strategically placed accelerometers. The process of removing inertial loads is discussed in Section 8.0.

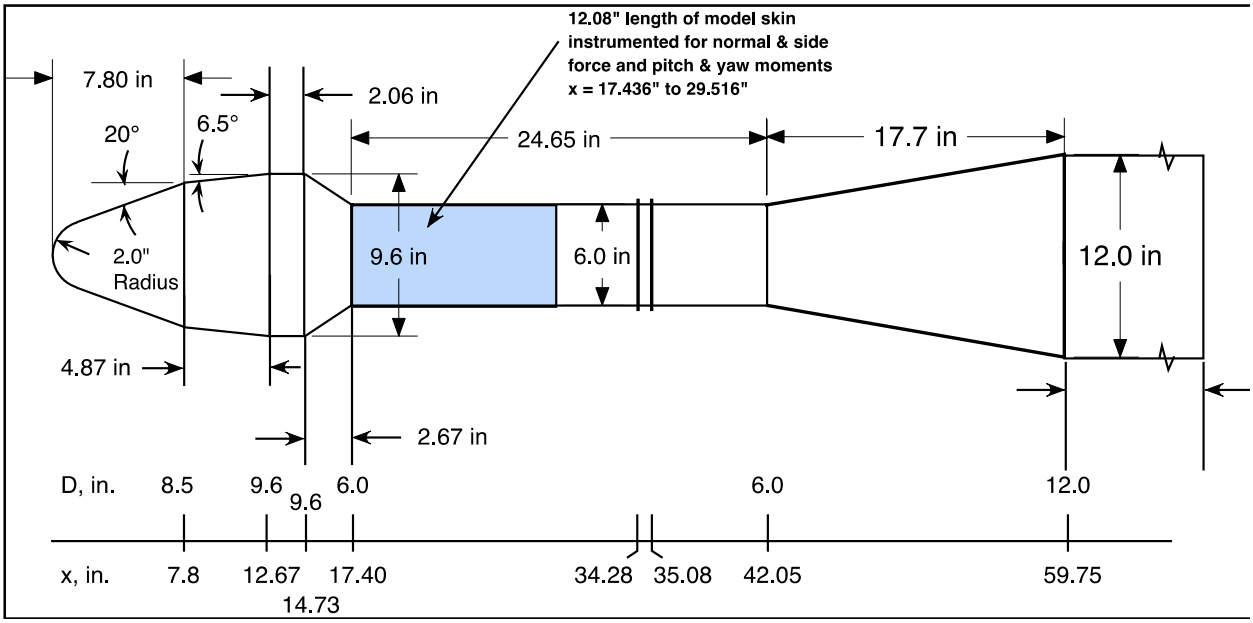

Note: The model reference length is 6.0 inches and the reference area is 28.274 square inches. The moment reference point is at the centerline midpoint of the metric section (23.476, 0, 0) inches.

Figure 7.1-1. Definition of Model Geometry

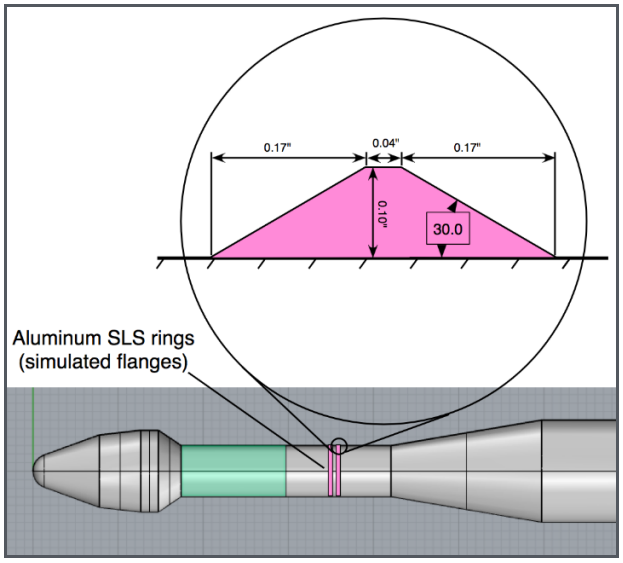

Note: Dimensions are inches. Rings are located at x = 34.28 inches and 35.08 inches in the model coordinate system (configuration 1—no flanges; configuration 2—forward flange; configuration 3—both flanges).

Figure 7.1-2. Simulated Flanges for Determining Aeroacoustic Increments

7.2 Model Layout

Figure 7.2-1 shows the model's coordinate system. The model is built around a stiff sting running through nearly its entire length. Figure 7.2-2 shows the overall layout of the model. The "wagon wheel" at the front of the sting (the bulkheads are referred to as wagon wheels due to the look of hub, spokes, and rim in an end view) transfers the axial force acting on the payload to the sting. The rest of the wagon wheels are machined to a snug fit around the sting but are fastened only to the model skins. The axial load acting on the model's metric section is carried through the balance to the sting, while the axial force acting on the booster and adapter are carried into the sting at the front of the booster adapter, which is pinned and bolted to the sting. The skins are machined in two pieces and are typically 0.5-inch thick for stiffness. The metric section skins are machined thinner for reduced mass (see Section 7.5). There is a collar attached to the sting to capture the booster close out in case of an attachment failure.

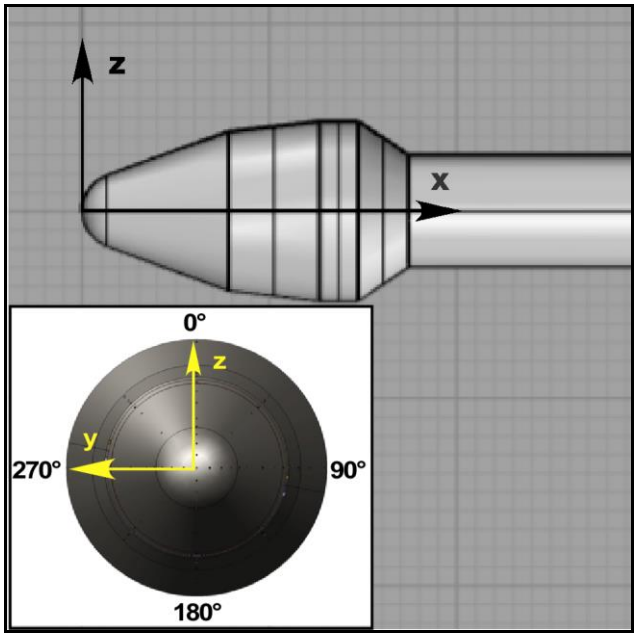

Figure 7.2-1. Model Coordinate System

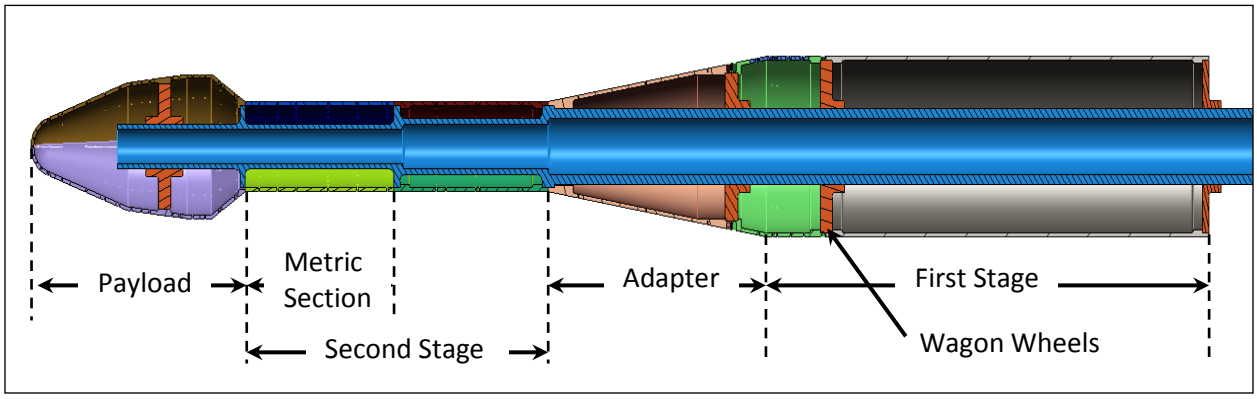

Figure 7.2-2. Model Layout Showing Central Sting and Bulkheads/Wagon Wheels (in red)

The model was mounted on the 20-inch primary extension from the Ames Unitary Plan Wind Tunnel (UPWT) inventory. This placed the model in an optimum location relative to the test section windows providing for good model illumination and camera views to maximize the uPSP signal. It also provided the stiffest available mount, which minimized model motion during the test. Additional model drawings are provided in Appendix A.

7.3 Static Pressure Taps

Figure 7.3-1 shows that 61 static pressure taps were located on the model's payload section. The taps were located every 90° in each row except as noted in the figure. These taps were plumbed to an electronically scanned pressure (ESP) transducer mounted in the payload section. An additional 60 pressure taps were located on the adapter and first stage of the model. These taps were used to verify the time-averaged pressures measured using the PSP during the test. The pressure tap locations are provided in Appendix B.

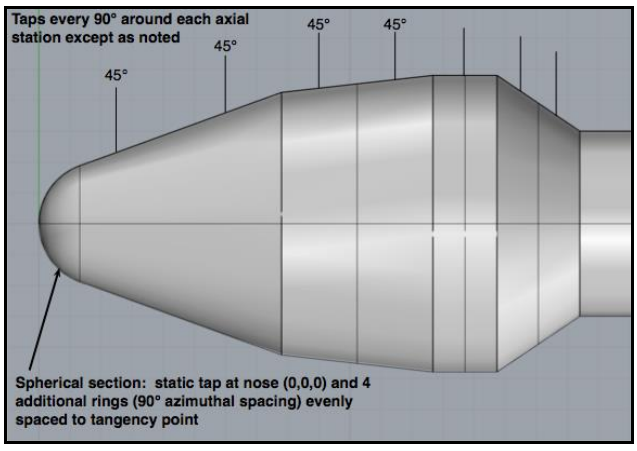

Figure 7.3-1. Locations of Static Pressure Taps on Payload Section of Model

7.4 Unsteady Pressure Transducers

Rings of unsteady pressure transducers were located on the model at 18 axial locations (Figure 7.4-1). Between 4 and 32 transducers were located in each of the rings.

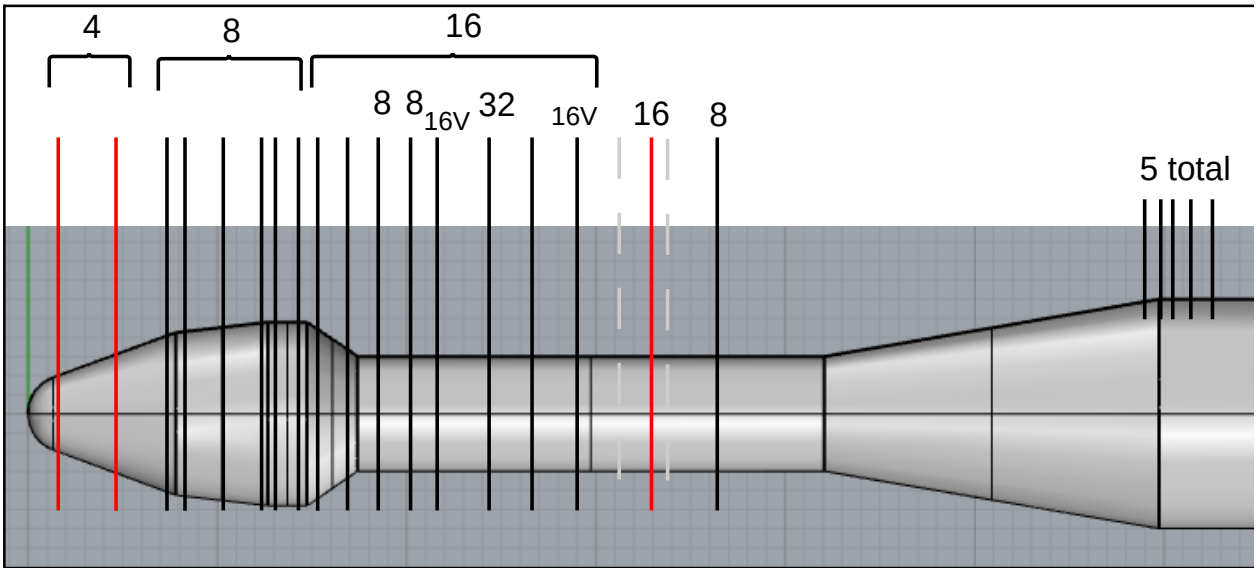

Note: Stations marked in black are identical to Coe and Nute [ref. 1]. Greyed-out dashed locations are ones from this reference that were not used. Stations marked in red are locations not duplicated from this reference.

Figure 7.4-1. Axial Location of the Rings of Kulite® Pressure Transducers Showing Number of Sensors in Each Ring

The transducers were evenly spaced in the azimuthal direction, except for those rings marked 16V. The sensors in these two rings were concentrated near the top of the model, as shown in Figure 7.4-2, with the spacing determined by interference between installed sensors. The unsteady pressure tap locations are provided in Appendix C.

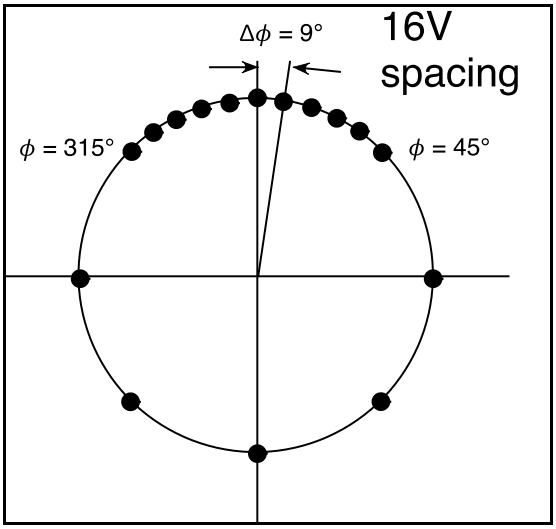

Figure 7.4-2. Azimuthal Distribution of Sensors for the 16V Ring Stations in Figure 7.4-1

7.5 4-Component Balance

A custom 4-component internal balance was used to measure the unsteady load on the model's metric section. Figure 7.5-1 shows the balance arrangement inside the model. The nonmetric side of the balance is pinned and bolted to the sting. The flexures connect to the metric model skin section.

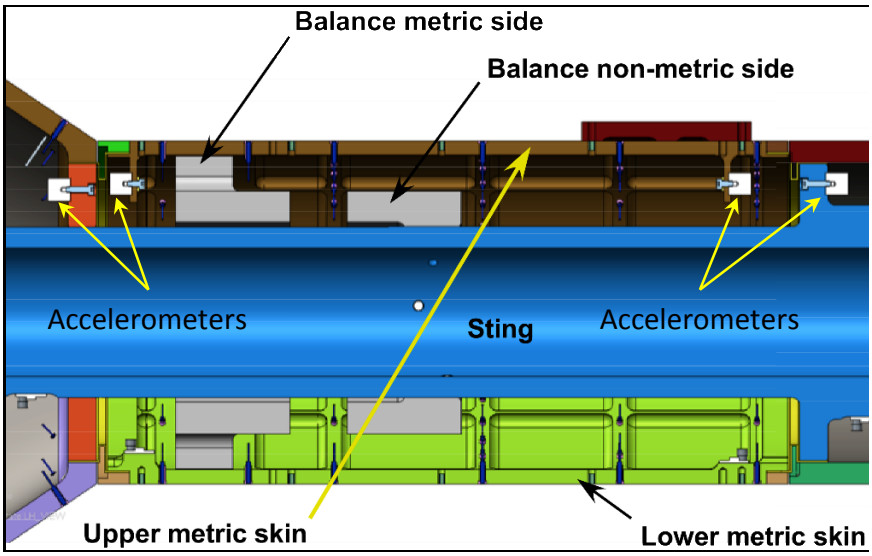

Note: Balance flexures are not shown.

Figure 7.5-1. Section Cut through Metric Part of the Model

Since one of the test objectives was to measure the unsteady aerodynamic forces and moments acting on the metric section, the inertia properties of the metric components needed to be characterized. In addition, it was important to minimize the inertial loads relative to the unsteady aerodynamic loads of interest. The metric skins were therefore made lighter by removing as much of the 0.5-inch thickness as possible. This was done by cutting pockets into the interior surface. Leaving a pattern of full thickness ribs kept significant stiffness, which helped in the second area of concern: structural vibration of the metric section itself.

A structural dynamics analysis of an early design of the model and balance showed the natural frequency of the balance-skin combination occurring at ~150 Hz. The assessment team was interested in the buffet loads to 680 Hz, so the low natural frequency was a problem. The original balance design had flexures sized for the maximum static and dynamic loads estimated using measured model accelerations from a test of the SLS configuration at a similar scale. The flexures sized for these loads were flexible to get high output from the strain gages for the expected loads. The team decided that a better overall measurement would result from driving that natural frequency much higher, so the skins were lightened and the flexures stiffened to raise the resonance to an estimated ~670 Hz. This meant lower sensitivity for the balance, but the less intrusive resonance relative to the frequency range of interest was more important.

Removal of the inertial loads and filtering of the structural dynamics modes of the model and balance is presented in Section 10.2.

7.6 Predicted Loads

The maximum loads were estimated using a CFD analysis of the model in free air at a variety of Mach numbers at 0°, 2°, and 4° angle of attack and the maximum Reynolds number (Re) for the test (9×10^6/ft). The maximum loads were predicted to be at $M = 1.2$ and $\alpha = 4°$. The predicted maximum loads are given in Appendix D. Table D-1 shows the body-axis, time-averaged force and moment coefficients, and the loads at the various test conditions for the overall model configuration. The moment reference point is the model nose.

8.0 Instrumentation

8.1 Unsteady Pressure-Sensitive Paint

The uPSP selected for the test was polymer-ceramic PSP, from Innovative Scientific Solutions, Inc. (ISSI), because it can detect pressure fluctuations to 20 kHz. The uPSP on the test article was imaged using four Vision Research Phantom® v1211 high-speed cameras at speeds of 5,000, 10,000, and 20,000 frames/sec. An Arnold Engineering Development Complex (AEDC) prototype uPSP data acquisition system (DAS) was used to control and acquire data from the high-speed cameras. In addition, the NASA Ames lifetime PSP system was used to measure the steady-state pressure distribution over the model surface. This system used eight Photometrics® CoolSNAP™ K4 cameras to capture images of the PSP fluorescence. The uPSP was excited with 40 ISSI 400nm light-emitting diode (LED) units for steady-state and unsteady systems. The

LEDs operated in pulsed mode for the steady-state system, and in continuous mode for the unsteady system.

The data acquisition sequence was set up to first acquire the conventional steady-state pressures, using ESP transducers, and the steady-state PSP data. Next, the unsteady pressure transducers, balance, accelerometer, and uPSP data were acquired. The facility unsteady DAS and the uPSP data system were not time synchronized and were recorded at different sample rates. The facility unsteady system acquired data at dual rates of 10,000 and 100,000 samples/sec. For the majority of the test series, 62,000 image frames were acquired for each Phantom camera at 5,000, 10,000, or 20,000 frames per second. Approximately 130 gigabytes (GB) of uPSP images were acquired for each data point with a total of 14 terabytes (TB) acquired for the test. During the entire test, a total of just under 6 minutes of uPSP image acquisition was used to generate the 14.7 TB of data.

A pilot study was performed in Test Cell 3 of the Ames Fluid Mechanics Laboratory to determine important parameters of the fast PSP measurements [ref. 11]. This test confirmed that the illumination levels expected in the 11-Foot Transonic Wind Tunnel would provide adequate uPSP signals.

The model was painted with a two-part epoxy base coat (white Awlgrip® 545), which was applied to the model before it was installed in the wind tunnel. This coat was wet-sanded to a smooth surface. The uPSP consists of two additional layers: a polymer-ceramic layer applied over the epoxy coat and a PSP dye applied as a very thin final coat. The uPSP coatings are very fragile and sensitive to contamination so they were applied to the model after it was mounted and otherwise fully prepared for testing. The polymer-ceramic base coat is relatively thick and is sprayed and suspended in water for application. The uPSP dye is carried by a volatile solvent and is applied as an overspray. The hole pattern in the unsteady pressure transducer holders was masked during application of both the epoxy and polymer-ceramic base coats. The masking dots were removed prior to spraying the uPSP dye coat. This process left small steps around each of the pressure transducers, which the test team tried to smooth with little success.

8.2 Unsteady Pressure Transducers

The model had 213 unsteady pressure transducers that were recovered from previously tested wind tunnel models. The Kulite® transducers were 0.072 inch in diameter and a mix of 5 and 15 psid (pounds per square inch differential) pressure range. Table 8.2-1 shows the sensor model numbers. The locations of the 5 and 15 psid transducers were determined by the expected mean pressure distribution so as not to over-range the transducers. Lead length was used to decide on specific sensor locations to facilitate the sensor wiring to the DAS. The sensor type is included in Appendix C's tables, which show the unsteady pressure transducer locations on the model.

Table 8.2-1. Kulite® Model Numbers Used for the Test

Model	XCL-18A-072-5D	XCL-18D-072-5D	XCL-18-072-15D	XCL-18C-072-15D	XCL-18E-072-15D	XCL-32-072-15D
Lead Length	75"	49.5"	76.5"	50"	135"	15"
Pressure	5 psid	5 psid	15 psid	15 psid	15 psid	15 psid
Type	18A	18D	18	18C	18E	32
On hand	50	88	10	29	15	33
Assigned	48	88	10	24	14	32

Because many of the sensors had been used in one or more models prior to this test, a number of the reference tubes were damaged and leaky. This meant that although the sensor reference tubes were connected to a driven reference pressure, the leaks from the damaged reference tubes occasionally showed slow changes in pressure that were caused by the driven reference pressure trying to set the desired pressure. These pressure changes were eliminated in the data processing by applying a polynomial de-trending to the data streams before doing any other processing.

Figures 8.2-1 and 8.2-2 show the details of the Kulite® pressure transducer holder. The holders accurately locate the transducer relative to the model's outer surface. Reference 7 describes the multi-hole holders and demonstrates the reduced high-frequency resonance and excellent frequency response relative to holders previously used with a single 0.040-inch diameter hole.

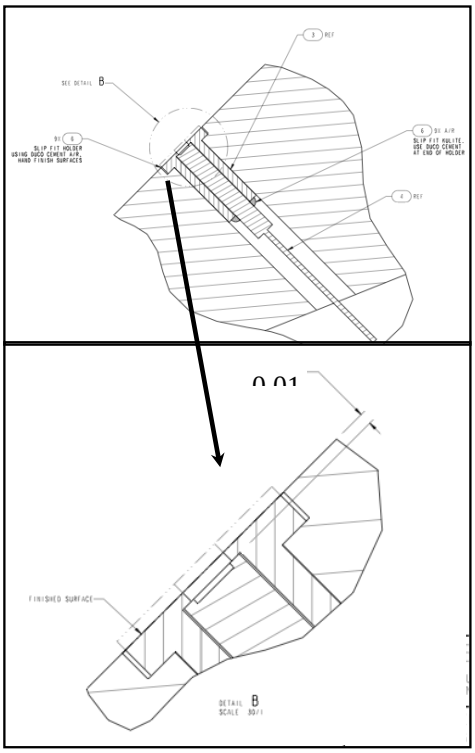

Figure 8.2-1. Section Cut through Kulite® Holder Showing Detail of Press Fit in Model Skin and Sensor Setback

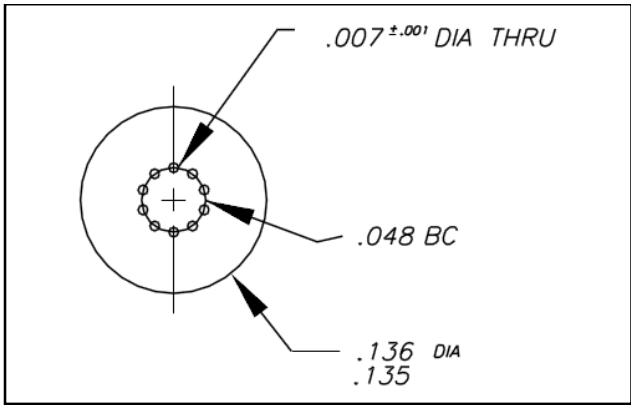

Figure 8.2-2. Holes in Kulite® Holder [ref. 4]

8.3 Electronically Scanned Static Pressures

The model had 120 static pressure taps. The pressure was acquired using an Initium DTC system with two PSI model 8800 64-port 15 psid electronically scanned modules. This system acts as a front end to the wind tunnel's DAS. The static pressure taps were used to anchor the time-averaged PSP measurements which was necessary because of the temperature sensitivity of the uPSP. The payload section pressure tap layout is shown in Figure 7.3-1, and Appendix B contains all of the pressure tap locations and numbering.

8.4 Four-Component Balance

A 12.1-inch-long section of the model was instrumented to measure the unsteady load directly using a custom balance (Figure 8.4-1). Two sets of gages were installed on the balance so that measurements could be acquired separately by the Ames UPWT high-speed data system and by an on-board DAS. Four components of forces and moments were acquired (i.e., normal force, side force, pitching moment, and yawing moment). Axial force and rolling moments were not measured, as they are not normally part of the launch vehicle BFF. In addition, including them would have compromised the balance design for the primary force and moment measurements.

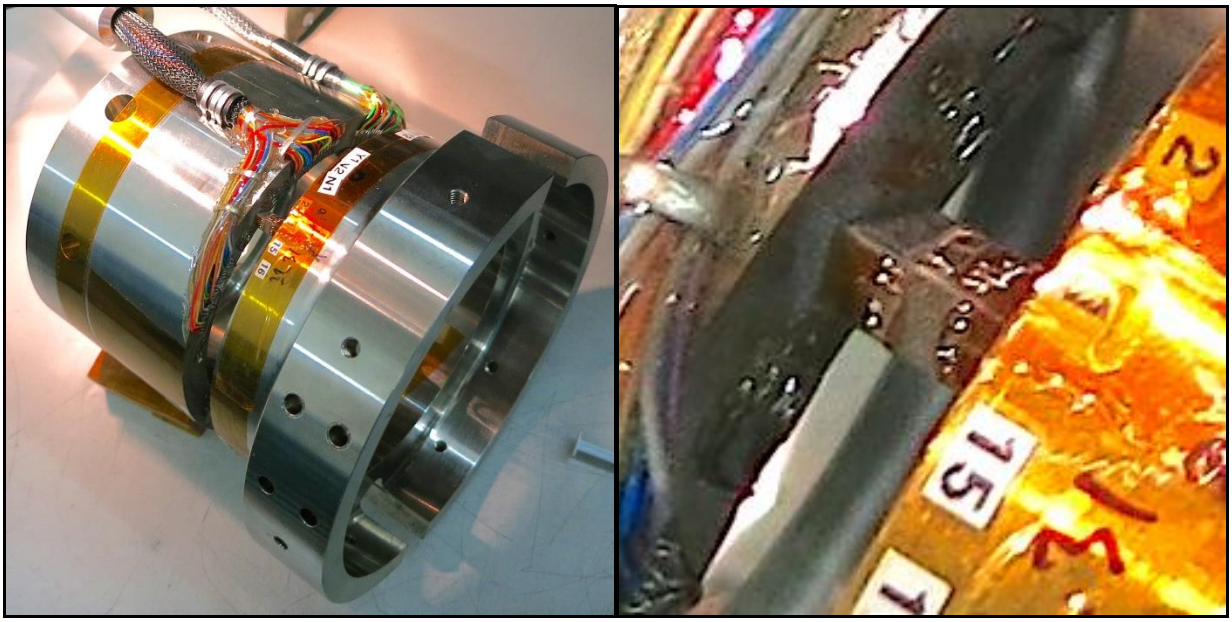

Note: The larger diameter is the metric side. The close-up on the right image shows one of the four flexures with the strain gages attached.

Figure 8.4-1. Four-Component Balance

Because the Kulite® cables and reference tubes cross the break from the nonmetric to the metric side of the balance, their contribution to the balance calibration was required. The balance and instrumentation were first installed in the model with the cabling secured. Figure 8.4-2 shows the inside surface of the metric skin section with the cable and tubing bundles and their anchor points.

After all instrumentation cables were secured and the model fully assembled, the complete system was shipped to the balance manufacturer (Triumph Force Measurement Systems, Inc.) for calibration. The model design included provision for the balance to fit between the model skin and the strong back/sting.

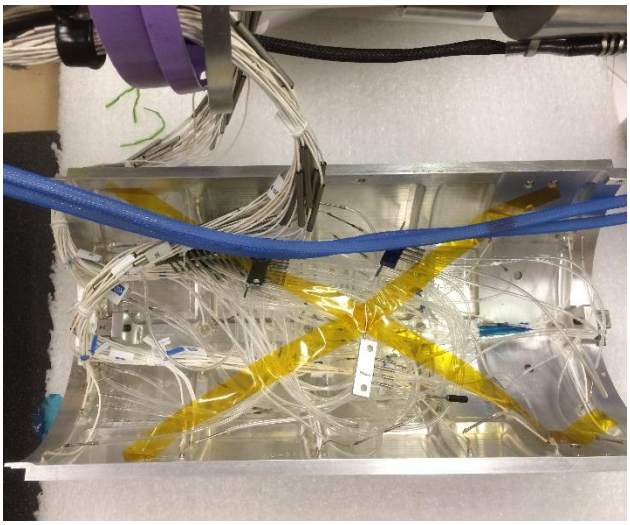

Note: This skin attaches to the balance on the right end in this image.

Figure 8.4-2. Cabling and Tubing on Inner Surface of the Lower Metric Skin

8.5 Tri-axial Accelerometers

A total of eight tri-axial accelerometers were installed to measure linear and angular acceleration of the metric and nonmetric portions of the model. Four of these were Endevco® 65-100 transducers, while the other four were digital devices that were part of the onboard balance DAS. These data were used to document the model accelerations on both sides of the break between the metric and nonmetric parts of the model. The sensor locations are shown in Figure 7.5-1. Use of the accelerometer data is discussed in Section 10.2.

8.6 Angle of Attack

A QA-2000 accelerometer was installed in the model's payload section to measure angle of attack (α). The device was electrically connected to provide the time history of the angle of attack rather than its more normal use for measuring the time-averaged value. An angle resolver was mounted to the base of the sting for the primary angle-of-attack measurement and was used to set angle of attack during the test.

8.7 Shadowgraph Imaging

High-speed shadowgraph video (up to 40,000 fps) was acquired to visualize shock motion around the model that contributes to the fluctuating pressure field. A series of runs was done at the start of the test to acquire those high-speed videos for the full range of selected test conditions. These videos with the unsteady pressure transducer measurements were used to identify the Mach numbers for the uPSP measurements.

8.8 Infrared Imaging

High-speed IR video was acquired at ~400 fps. This information provided verification of the transition location on the nose cone. A lower frame rate IR camera was used to image the metric section of the model to help locate flow reattachment.

9.0 Calibrations

9.1 Electronically Scanned Pressure Modules

The ESP modules were calibrated prior to and during test using the manufacturer's procedures. Transducers with greater than 0.5-percent error were to be flagged, but none exceeded this threshold during the test.

9.2 Unsteady Pressure Transducers

The factory calibrations for the Kulite® transducers were used for the test with checks for sensitivity and phase. A piston phone was used to check the sensor health after installation into the model and prior to running in the wind tunnel. Failed Kulite® transducers were not replaced during the test. The Kulite® transducers calibration checks were performed in the Ames Aeroacoustics Lab before installation. The calibration consisted of a static-pressure sensitivity and phase checks relative to a reference Dantec 0.25-inch microphone. Only transducers that matched their data-sheet calibration specs within 1 percent in sensitivity and 10° in phase were used.

9.3 Four-Component Balance

The balance had a preliminary calibration before being shipped to the model manufacturer for installation. This calibration checked the balance linearity, range, and flexibility to ensure it was electrically sound and would provide accurate measurements over the expected load range. The assessment team waited for the final calibration until the instrumentation (particularly the Kulite® transducers) was installed. This ensured that the calibration would capture the effect of the reference tubing and cables that bridged the metric to nonmetric break.

The balance was calibrated using weight-pan loadings at a total of 20 points on the metric skins. Threaded holes in the skins at 5 axial locations at 0°, 90°, 180°, and 270° azimuth angles allowed gravity loading in those directions. The moment reference center was defined at the geometric center of the metric model section. Figure 9.3-1 shows the model in the calibration rig. The model was rolled to align the desired azimuth angle with gravity. A weight pan was attached at each of the 5 load points and the balance loaded to the expected maximum load of 80 lb. The model was re-leveled at every loading. The balance has two sets of gages, one for the standard analog wind tunnel data system and the other for the on-board data system. Two American Institute of Aeronautics and Astronautics (AIAA) standard matrices [ref. 8] were generated for the balance, one for each set of gages.

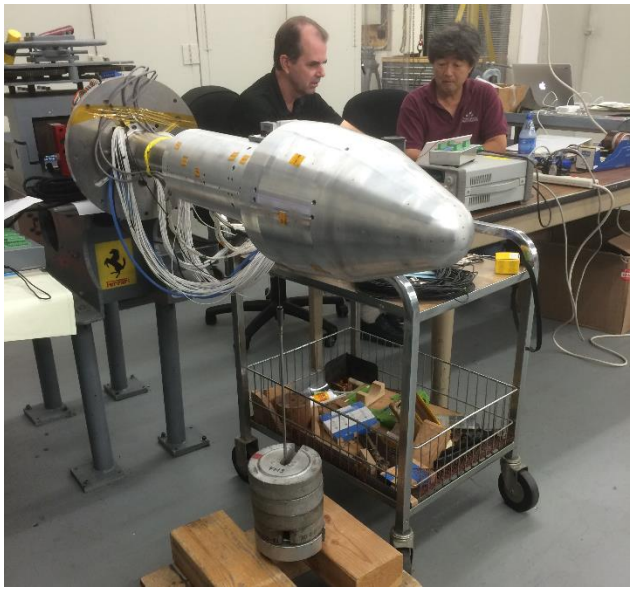

Figure 9.3-1. Model in Pitch/Roll Fixture for Balance Calibration

10.0 Data Processing

10.1 Unsteady Transducer Data

Rapid data processing was needed to monitor sensor health and to provide test matrix guidance to ensure the most interesting conditions were measured during the test. Several analysts shared the task of monitoring and interpreting the data in order to make testing decisions quickly. Thirteen computers were used to process the Kulite® data. Typically eight of those machines were used to process the data. If the processing fell behind, additional processors could be added. The processed data were passed along to six workstations for analysis.

The processed data was stored in a Firebird database on the aero server—an IBM x3650m3 server running Red Hat® Linux. All of the processing machines were located on the Gigibit processed data network.

10.1.1 Software

A program called *SLSprocessScheduler.exe* conducted the data processing. Each instance of *SLSprocessScheduler* was responsible for processing one data point at a time. Several programs were called by *SLSprocessScheduler* to process, scale, and store the data.

To process a data point, the software would "check out" a data point by querying a stored procedure on the ProcQueue database. If all 12 files for a data point were present, the stored procedure would change the status flags of those files to a unique serial number. Once a serial number was assigned, those data files could no longer be processed by other CPUs. Once a set of 12 files was checked out, each file was opened and processed, and the results were placed in

the processed database and MATLAB® binary files containing all of the processed data. Upon completion of processing, *SLSprocessSchedule* changed the status flag of the files to "processed" and made a request to the ProcQueue database to look for another set of files to process.

Administration and monitoring of the processing was conducted using *ProcQueueAdmin.exe*. *ProcQueueAdmin* displayed a list of files that were in process and those to be processed. The list was updated once a minute. This software allowed the user to change the file status and to prioritize data files in the processing queue. By default, the oldest data was processed first, but by changing the priority, files could be processed out of order.

Information about each data point, including identification and condition information, was put into the processed database using shell scripts running on the aero server. Text files with condition info were sent to the aero server after the completion of every point by the wind tunnel Standard Data System (SDS) via secure copy. The login script of the aero server parsed each text file and placed the information into the database and then moved the file to a directory structure that organized the data so that it could be easily retrieved.

10.1.2 Spectra Calculation

Spectra were calculated using the Discrete Fourier Transform (DFT). The optimized DFT algorithm is known as a Fast Fourier Transform (FFT). The following equation shows the MATLAB® FFT algorithm used:

$$X(k) = \sum_{n=1}^{N} x(n) \cdot e^{-2j\pi \cdot (k-1) \cdot (n-1) \cdot \frac{1}{N}}, 1 \le k \le N,$$

where N is the number of points in the FFT, and k is the frequency bin index.

Narrowband spectra were calculated for each channel at both sample rates. The low-frequency data were processed with 1,024-point FFTs to produce spectra with a frequency resolution of 6.25 Hz. The high-frequency data were processed with 4,096-point FFTs for a resolution of 25 Hz. The low-frequency data were processed with 512-point FFTs to produce spectra with a frequency resolution of 9.375 Hz. The high-frequency data were processed with 4,096-point FFTs for a resolution of 37.5 Hz.

Prior to calculating the spectra, the time data were windowed with a Hanning window. The spectra were adjusted to contain the right overall energy by applying the standard Hanning window amplitude correction of 8/3. It is important to note that this correction accounts for the overall broadband energy, but is incorrect for tonal data analysis. The pure tone amplitude in the data will be lower than the true value.

The narrowband data are saved in MATLAB® binary files. Plotting and further processing can be done in that software package.

10.2 Unsteady Balance Data

There are several steps involved in removing the inertial tares from the balance data. The four accelerometers were used to fully characterize the motion of the metric and non-metric sections of the model and enabled calculation of the inertial loads generated by the metric section. This inertial load was subtracted from the load measured by the balance to isolate the aerodynamic loads acting on the metric section

Due to the complexity of the model dynamic characteristics, a simple rigid model analysis is not sufficient to capture the complete model motion. Therefore, a black-box state-space multiple input–single output (MISO) model was used to estimate the fluctuating aerodynamic loads. The following steps are the simplified procedures of determining the model.

Step 1: Aerodynamic load is simulated by a shaker with a load cell attached between it and the metric section shown in Figure 10.2-1. A white noise input was applied to the metric skin while acquiring accelerometer signals. This metric shake experiment is twofold. The resulting data was used to determine the dynamic characteristic of the model, locating the resonance frequencies of the metric portion. Since the shaker data also acted as a simulated aerodynamic load, they were used to create the system identification math model. The simulated aerodynamic load was applied at 5 locations along the 90° configuration, and 4 locations at 180°.

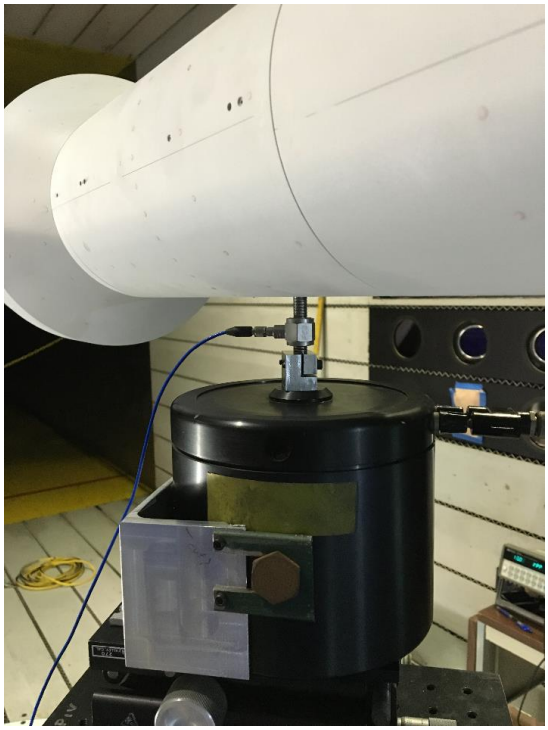

Figure 10.2-1. Shaker Installation in the Wind Tunnel Test Section Used to Characterize the Model's Structural Modes

Step 2: During model assembly and instrumentation installation, an intermittent noise was discovered in the Endevco® Isotron® accelerometers and balance strain gages that continued throughout the test. The acquired signal, *Y(f),* is assumed to contain the desired signal and the noise floor, *X(f)* and *N(f).* To increase the signal-to-noise ratio, a zero point was acquired to measure the noise floor for use to remove it using spectral subtraction on the metric shaker data. Similarly, a wind-off zero during the wind tunnel tests was used to remove the noise floor for the rest of the test data:

$$Y(f) = X(f) + N(f)$$

$$|X(f)| = |\gamma(f)| - \partial|N(f)|$$

Step 3: Two MISO models were created per direction (y and z) with a [20th] order continuous black-box state-space model in the time and frequency domain for comparison (Table 10.2-1). The order, input-output delay, and boundary conditions went through an intensive optimization analysis to determine the best state space model. The modeling equations are [ref. 14]:

$$\frac{dx(t)}{d(t)} = Ax(t) + Bu(t) + Ke(t)$$

$$y(t) = Cx(t) + Du(t) + e(t)$$

where A, B, C, D, and K are the state space matrices, *y(t)* is the input vector and *u(t)* is the output vector. The disturbance model, *K*, was fixed to zero to suppress the noise component estimation. Buffet loads typically contain random broadband frequencies and could be identified as noise. A, B, and C were estimated as free parameters, and D was fixed to zero assuming no feed-through since the model is assumed to be a linear mechanical system. The model was validated using additional data points that were not used to determine the modeling parameters.

Table 10.2-1. MISO Models per Direction

	MISO Y-Direction	**MISO Z-Direction**
Inputs	A1y A2y A3y A4y	A1z A2z A3z A4z
Outputs	Load Cell	Load Cell

Step 4: Once the model was completed, the predicted aerodynamic loads were separated into the 4-balance components relative to the dynamic balance coordinates of normal, side, yaw, and pitch.

At the higher Mach numbers and certain alpha configurations, the strut and sting vibrations propagated upstream into the model. Since the strut was never excited during the metric modal test, the math model was not able to account for the additional inertial load due to the strut

vibrations propagating upstream to the model. Fortunately, based on past tests and an additional post-test modal test, the strut frequencies were identified in the final data set.

10.3 PSP Data

10.3.1 Traditional uPSP Processing

The theory and practice of PSP measurements will not be discussed here in detail. The basics of the technique can be found in References 2 and 3. In general, PSP is made up of an oxygen-sensitive molecule (i.e., luminophore) in a binder. The paint is illuminated using high-intensity purple LED lights and the luminophore in the paint fluoresces red. The brightness of the radiated light is inversely proportional to the local concentration of oxygen. The data are acquired using sensitive, high-speed cameras looking at the model from multiple angles. The process to convert the intensity fluctuations to fluctuating pressures is nontrivial, and the amount of data to process is large (i.e., TB scale).

The specifics of the unsteady PSP processing used are covered by Sellers [ref. 4].
Figure 10.3.1-1 shows the model illuminated with the purple LEDs and the red fluorescence. Some of the lights and cameras are visible through the windows on the side and floor of the test section.

The paint was calibrated at AEDC in a pressure chamber for unsteady and steady-state processing prior to the test. The calibration documented the paint sensitivity to mean pressure and temperature. The normal procedures for steady-state PSP was followed along with additional procedures for unsteady PSP [ref. 4].

One of the drawbacks of the current generation of uPSPs is the temperature sensitivity. This makes accurate measurement of the time-averaged pressure distribution difficult. The time-averaged pressure is used in the uPSP processing because the sensitivity of the paint is a function of pressure. The time-averaged pressure is therefore used in the uPSP data processing and commonly seen temperature variations on the model can cause measureable errors in the sensitivity. The testing process was modified during the test to heat-soak the model by running at Mach 0.8 for up to 30 minutes. This reduced the temperature variations on the model significantly.

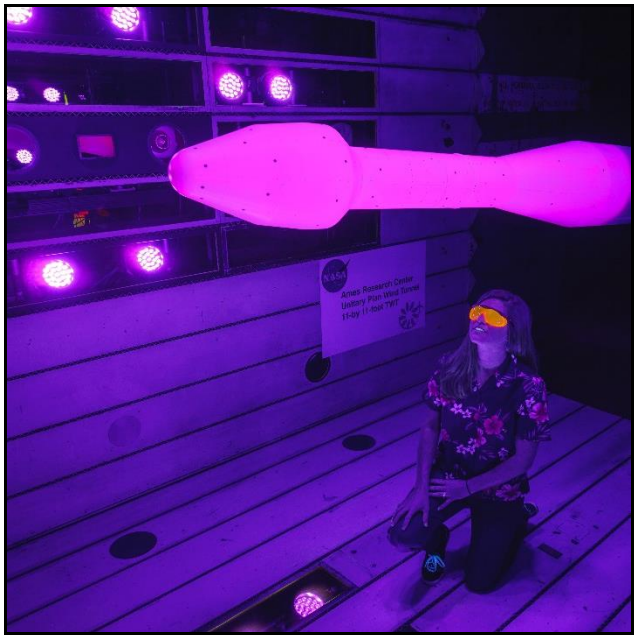

Figure 10.3.1-1. Model Illuminated by Blue LED Lamps

10.3.2 Direct Scaling from Kulite® Measurements

Another method of determining uPSP pressure sensitivity is to directly scale the rms (root mean square) of the pressure fluctuations measured by uPSP to match the Kulite® sensors. The ratio of the uPSP intensity ratio rms to the Kulite® rms provides the scaling to compute the pressure from the uPSP images. This method was quicker to compute but is potentially less accurate than the traditional method described in Reference 11. In this second method, the intensity ratio between a pixel in a reference image and the same pixel in a measurement image is multiplied by a calibration constant determined from the Kulite® rms measurements. This calibration constant ensures the uPSP rms matches the Kulite® values. There is some danger in using the direct scaling, particularly in areas of the model where the fluctuating pressure appears to be below the level detectable by the uPSP. The advantage of this method is that it may do a better job of accounting for the effect of temperature on the paint sensitivity. The direct scaling method was used for preliminary uPSP data analysis and is described in References 11 and 12, but was not used in the results presented in this report.

10.4 Force Integration

10.4.1 Current Integration Method

Complete descriptions of the integration techniques used to estimate BFF from unsteady pressure measurements are given by Piatak et al. [ref. 9] and Sekula et al. [ref. 10]. Integrating the pressures by assuming the pressures are perfectly correlated over a given sensor's area of influence produces unrealistically high buffet estimates. Current practice is to adjust the

integrated force for a given sensor by the ratio of the physical area of influence bounded by the half-distance to adjacent sensors in the axial and azimuthal directions and a "coherence area." The coherence area is defined as the rectangular surface region whose length in the axial and azimuthal directions are defined by the distance from the sensor at which the coherence in that direction falls to 0.707. This method produced improved BFF estimates for the SLS than the previous method that corrected the integration area using only the axial coherence length, and is significantly better than assuming perfect correlation of the pressures over the physical sensor area of influence [ref. 10].

11.0 Test Campaign

Trip dots were applied to the model near the same location shown in Coe and Nute [ref. 1] and were sized using the method outlined in Reference 6. These adhesive dots are commonly used in wind tunnel tests and measure 0.0086 inch in height, 0.05 inch in diameter, and are spaced 0.10 inch between centers. This height exceeds the minimum trip height for all test Mach numbers and Reynolds numbers for the test. Coe and Nute used a grit strip but did not report the grit size, or strip size and location. Regardless, no effect was reported on the static pressure distributions or measured rms pressure fluctuations.

The assessment team considered running with and without the trip dots, but the effort involved in repainting the model around the trips would have been prohibitively time consuming because it would require repainting the entire nose section. Therefore, the entire test was run with the trip dots.

IR thermography showed that transition occurred at the sphere-cone junction, likely caused by the discontinuous change in surface curvature. The trip dots did not appear to have any downstream influence that was visible in the IR images or the Cp_{rms} (rms of the pressure coefficient) measurements.

Figure 11.0-1 shows IR thermographs during startup for an early test run. As the Mach number increased, the transition location moved upstream, eventually passing forward of the trip dots and stabilizing at the sphere-cone junction. Videos of this behavior for several wind tunnel starts convinced the assessment team that the transition location would not vary during the test. In Figure 11.0-1a, M = 0.13 and transition occurs aft of the trip dots on the forward conical part of the payload section. At higher Mach numbers, transition moved forward (Figures 11.0-1b and c) and above M = 0.3, reached the sphere-cone junction.

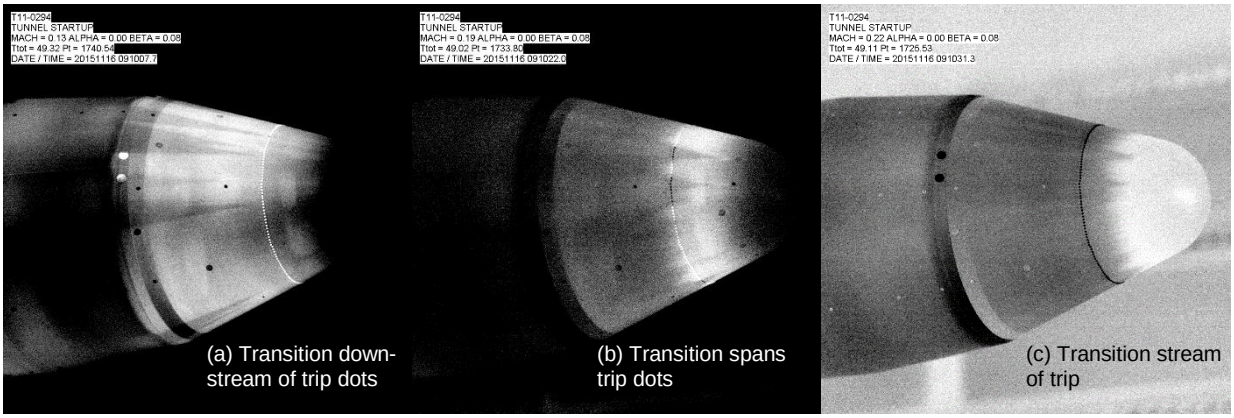

Figure 11.0-1. Transition Location Varying with Mach Number during a Wind Tunnel Start— $\alpha = \beta = 0°$, (a) M = 0.13, (b) M = 0.19, (c) M = 0.22

11.1 Test Operations

The test matrix is shown in Appendix E. Complete data sets including uPSP were acquired for a total of 78 test conditions (6, M; 3, Re; and 3, α). There were 11 repeat runs for the full instrumentation suite of dynamic data and uPSP images. The flush airdata sensing (FADS) calibration portion of the test included 20 free-stream conditions with 25 α/β combinations.

The test was run one shift per day, and ran November 9–17, 2015. Normally the NASA Ames UPWT runs two shifts per day, but a single shift was more effective for this test because the research team could spend some time every day after hours to solve problems identified during the run shift. The test held significant interest from the launch vehicle industry. Engineers from ATK/Orbital, SpaceX, ULA, Boeing, and ATA attended the team planning meetings or the test itself. There were six industry visitors who attended the actual test to better understand the techniques being applied to understand buffet measurements. The ATK engineers were particularly interested in the technique and wanted to see a flight test to learn how the wind tunnel measurements relate to the buffet experienced in flight.

As the test progressed, the importance of keeping the model temperature relatively constant became apparent from the time-averaged PSP measurements and IR images. Different portions of the model heated at different rates, primarily due to different skin thickness. The IR images showed this change, and it had an effect on the time-averaged PSP because of the relatively high sensitivity of the uPSP formulation to temperature. As mentioned in Section 10.3.1, the sensitivity of the uPSP varies with both mean pressure temperature. The paint is calibrated for both effects, but the temperature was not measured during this test. The temperature therefore affects the time-averaged PSP pressure measurements and also the computed sensitivity of the uPSP to the local pressure. For later runs, the model was heat-soaked by starting the shift with several FADS-specific test runs. After the tunnel had been run for approximately 30 minutes,

the model was sufficiently heat-soaked to reduce, but not eliminate, the surface temperature variations.

12.0 Test Results

The test ran November 9–17, 2015, with a total of 63 occupancy hours.

12.1 Static Pressure Measurements

12.1.1 Static Taps

The first data comparisons with Coe and Nute [ref. 1] were the static pressure distributions. In general, the comparisons were good, especially considering the 50-year span between the measurement and the fact that the 1962 test used a mahogany model with some uncertainty about how sharp the corners and transition from sphere to the cone on the nose were. Figures 12.1.1-1 through 12.1.1-4 show comparisons for M = 0.6, 0.8, 0.95, and 1.2. In each figure, the Reference 1 data are shown as dark circles while the four sets of open symbols are for this assessment. The four sets of assessment data are along the model ϕ = 0°, 90°, 180°, and 270° lines. The match between the pressure along these lines indicates that the model is symmetric and the angles of attack and sideslip were close to 0°.

Figures 12.1.1-5 and 12.1.1-6 show similar comparisons with Reference 1 data at α = 4°. In this case, the assessment data are at α = 4° and ϕ = 0° (top of model), α = –4° and ϕ = 180°, β = –4° and ϕ = 270°, and β = 4° and ϕ= 90°. The close correspondence between the data sets indicates good model symmetry and accurate $\boldsymbol{\alpha}$ and $\boldsymbol{\beta}$ settings, at least relative to the resolution of the Cp variations. The difference in the static pressure distribution on the model top and bottom at α = 4° and M = 0.8 is shown in Figure 12.1.1-7.

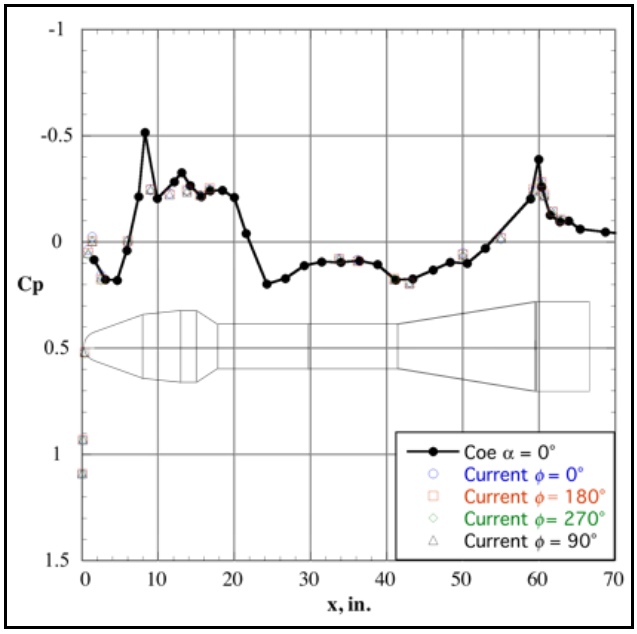

Figure 12.1.1-1. Static Pressure Distribution Comparison between Coe and Nute [ref. 1] and Assessment—M = 0.6, $\alpha = \beta = 0°$, Re = 3×10^6

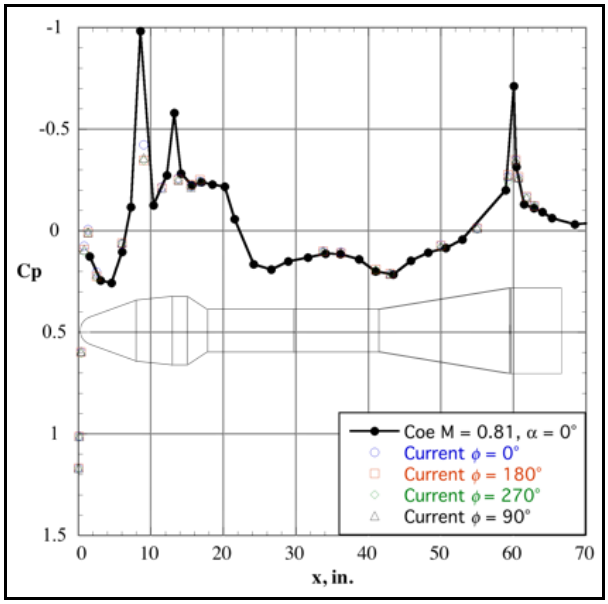

Figure 12.1.1-2. Static Pressure Distribution Comparison between Coe and Nute [ref. 1] and Assessment—M = 0.8, $\alpha = \beta = 0°$, Re = 3×10^6

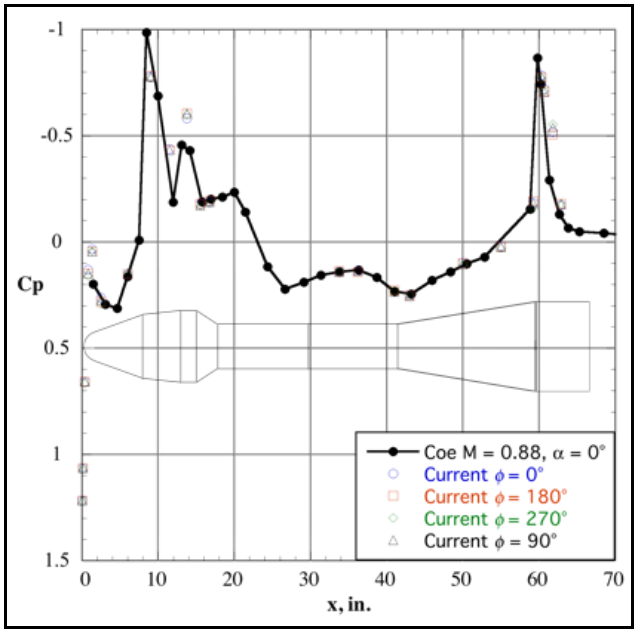

Figure 12.1.1-3. Static Pressure Distribution Comparison between Coe and Nute [ref. 1] and Assessment—M = 0.9, $\alpha = \beta = 0°$, Re = 3×10^6

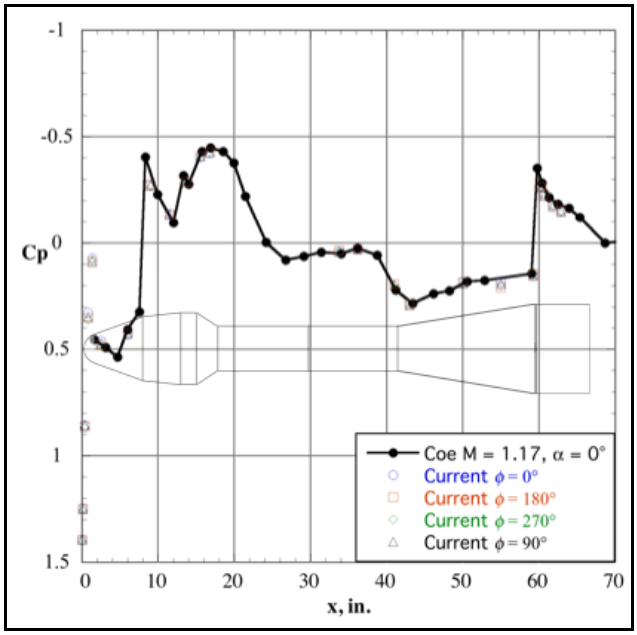

Figure 12.1.1-4. Static Pressure Distribution Comparison between Coe and Nute [ref. 1] and Assessment—M = 1.2, $\alpha = \beta = 0°$, Re = 3×10^6

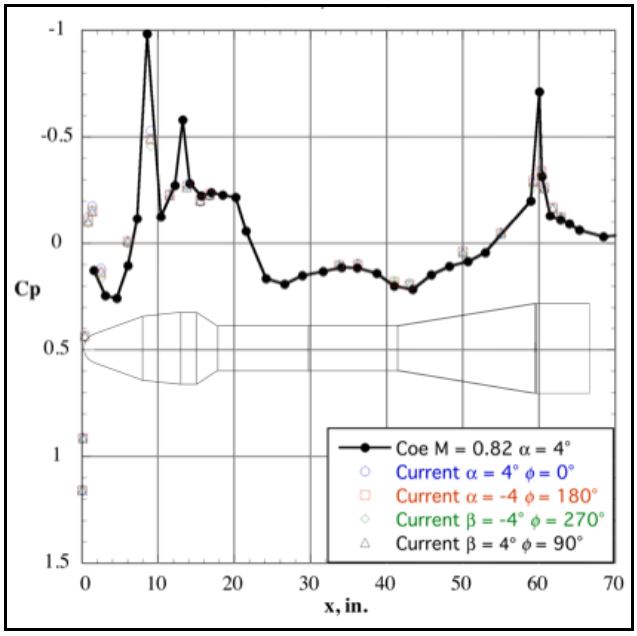

Figure 12.1.1-5. Leeward-side Static Pressure Distribution Comparison between Coe and Nute [ref. 1] and Assessment—M = 0.8, α or β = ±4°, Re = 3×10⁶

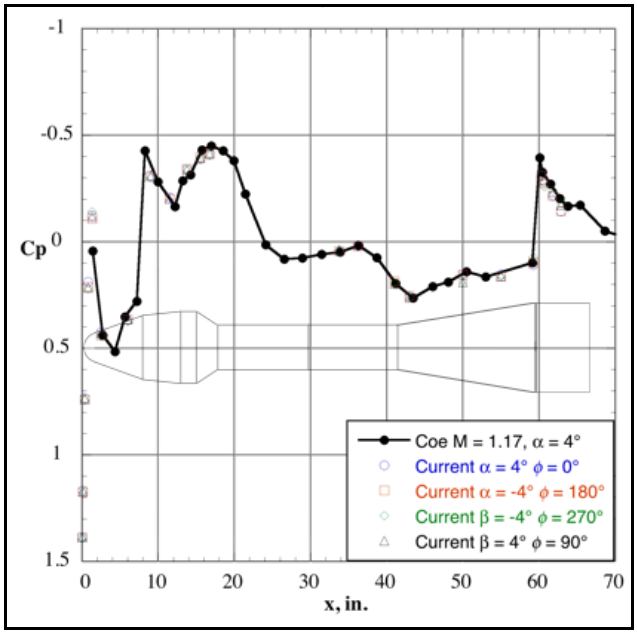

Figure 12.1.1-6. Leeward-side Static Pressure Distribution Comparison between Coe and Nute [ref. 1] and Assessment—M = 1.2, α or β = ±4°, Re = 3×10⁶

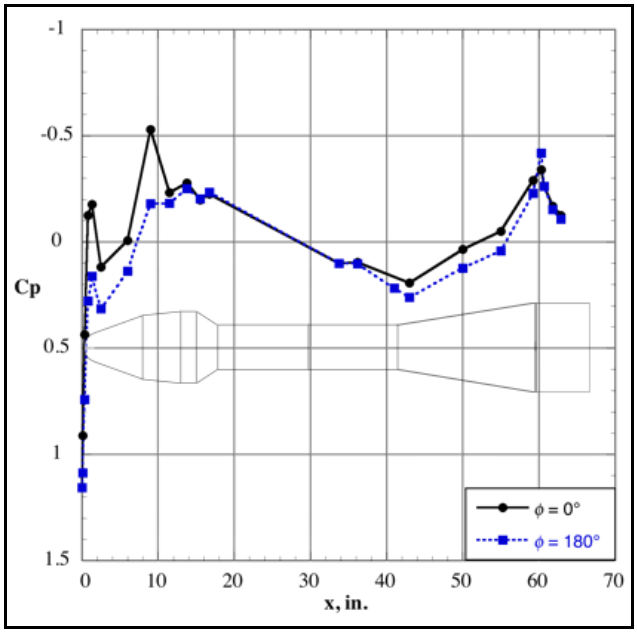

Figure 12.1.1-7. Static Pressure Distribution at Model's Top and Bottom—M = 0.8, α = 4°, Re = 3×10⁶

12.1.2 Time-averaged PSP

The time-averaged PSP results provide more detailed pressure distributions, in particular showing the pressure variation on the metric section where there were no static taps. The time-averaged PSP was not as accurate for this test as it would have been for a more typical wind tunnel test because the uPSP chemistry did not compensate for temperature variations. The time-averaged results were manually corrected for test conditions where the temperature variation was large. This was the case primarily for configuration 1 with no flange rings. After the initial runs, the assessment team determined that the model needed to be heat-soaked to reduce the pressure measurements errors due to temperature variations.

Figure 12.1.2-1 shows the pressure distribution mapped onto a three-dimensional surface grid for M = 0.8, 0.92, and 1.1; Re = 3×10^6, and $\alpha = 0°$. The figure shows the time-averaged pressure measured using PSP as color contours. The dots occasionally visible on the model are colored by the static pressure measured at those locations by the ESP modules. Ideally, these dots would be the same color as the surrounding surface in these images. The differences are primarily due to the non-uniform temperature of the model.

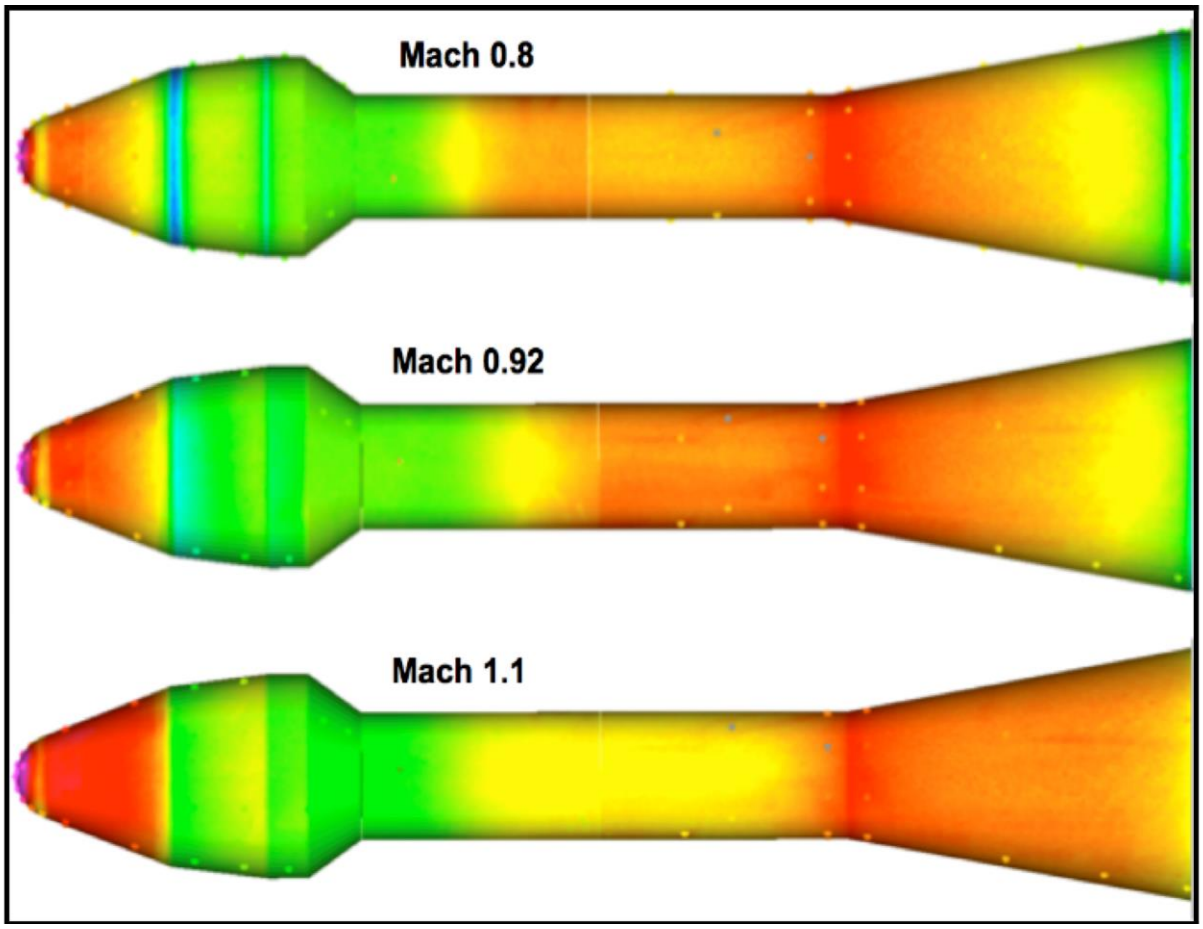

Figure 12.1.2-1. Static Pressure Distribution from Time-averaged PSP at Model's Top and Bottom—Configuration 1, $\alpha = 0°$, Re = 3×10^6

12.2 Unsteady Pressures from Transducers

The fluctuating pressure levels did not match those reported by Coe and Nute [ref. 1]. Figures 12.2-1a through c show comparisons of Cp_{rms} for various Mach numbers and angles of attack. In all cases, the assessment data show much higher pressure fluctuations than the reference results. The data acquisition and processing procedures used by Coe and Nute are likely the source of the disagreement since those data were high-pass filtered with filter characteristics, as shown in Figure 12.2-2 [ref. 2].

Figure 12.2-2 shows the filter characteristics used by Coe and Nute [ref. 15]. This filtering removed any contribution of low-frequency (below 10 Hz) fluctuations to the Cp_{rms} values and any contributions for frequency content above ~800 Hz. In this assessment, there was no high-pass filter, and the low-pass filter for anti-aliasing was set at 10 kHz.

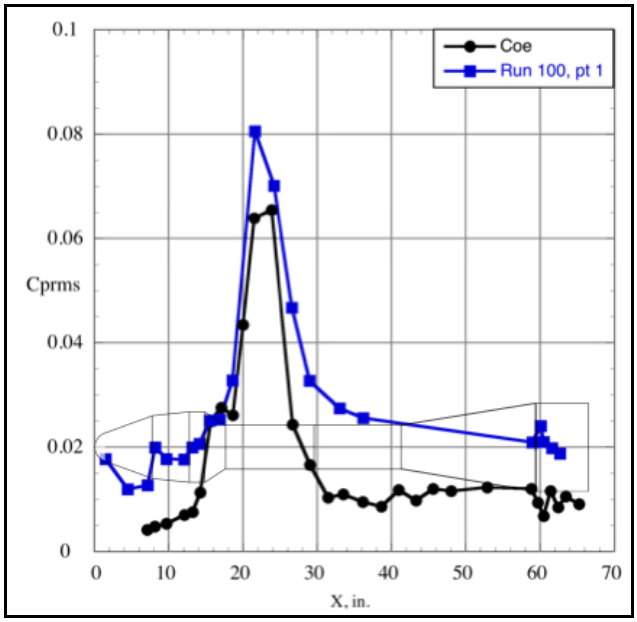

Figure 12.2-1a. Cp_{rms} along Top ($\phi = 0°$) from Coe and Nute [ref. 1] and Assessment—M = 0.6, $\alpha = -4°$, Re = 3×10^6

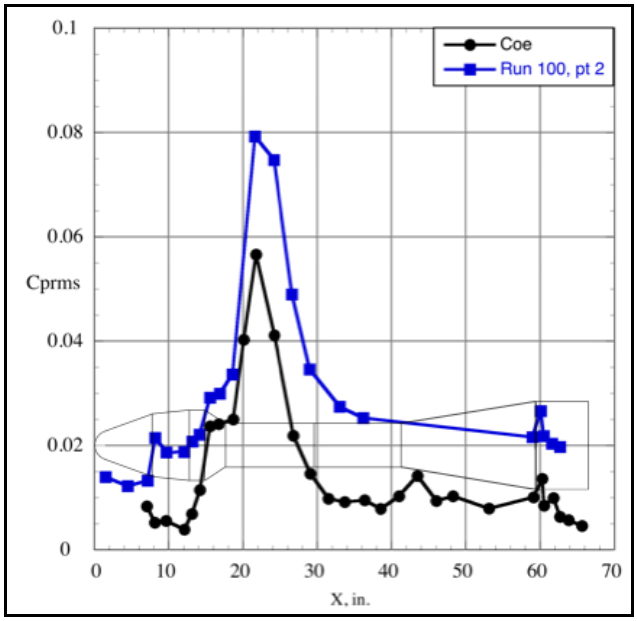

Figure 12.2-1b. Cp_{rms} along Top ($\phi = 0°$) from Coe and Nute [ref. 1] and Assessment—M = 0.6, $\alpha = 0°$, Re = 3×10^6

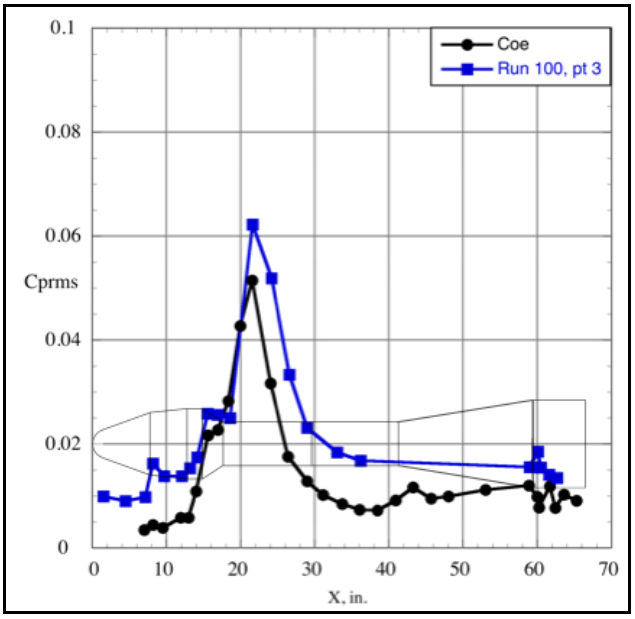

Figure 12.2-1c. Cp_{rms} along Top (ϕ = 0°) from Coe and Nute [ref. 1] and Assessment—M = 0.6, α = 0°, Re = 3×10^6

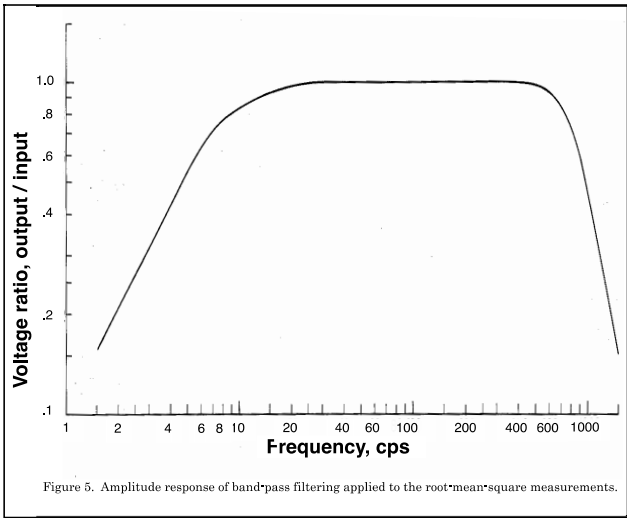

Figure 12.2-2. Characteristics of Filter Used by Coe and Nute [refs. 1 and 15]

The shapes of the assessment and previously reported Cp_{rms} distributions are similar with elevated levels from both data sets occurring in the same locations. The occasional extremely high levels occur at the same locations, and the narrowness and occasional lack of a high data point indicate areas of high fluctuating pressure. A Kulite® transducer located a fraction of an inch from the peak level location can significantly under-record the maximum fluctuating pressure level. This

is another potential advantage from uPSP use, since the high spatial density of the pressure measurements would capture the peak fluctuating pressure levels, thereby eliminating non-conservative measurements.

The run-to-run repeatability of the assessment data was excellent. Figures 12.2-3a through f show the Kulite® measurements from identical test conditions taken on consecutive days at different Mach numbers and angles of attack. Figure 12.2-3a shows the biggest difference in Cp_{rms} at M = 0.6, $\boldsymbol{\alpha}$ = 4°, and ϕ = 0°. The maximum Cp_{rms} difference was ~10 percent on the generally quiet payload section at M = 0.6.

At higher Mach numbers and higher dynamic pressures, the differences in Cp_{rms} between runs was smaller. Figures 12.2-3b shows the repeatability for M = 0.8 at α = 0°, and for the ϕ = 0° row of sensors. In this case, the difference between the two sets of data was small. Figures 12.2-3c through d show the repeatability for M = 0.8 and α = 4° for the leeward (ϕ = 0°) and windward (ϕ = 180°) sides. Again, the differences between data sets were small. Figures 12.2-3e through f show repeatability for M = 0.8 and α = 4° for ϕ = 90° and 270°, respectively, with little difference between the data sets.

Figure 12.2-3g shows the back-to-back repeatability along the sides of the model for M = 1.1 and α = 4°. The repeatability was good for each row of sensors individually, but there was a difference between the Cp_{rms} levels on the two sides indicating some level of asymmetry or measurements. The larger apparent differences in levels at x = ~17 and 36 inches result from failed sensors on ϕ = 90° at those stations.

Additional symmetry checks for the Kulite® sensors are shown in Figures 12.2-4a through c. Figure 12.2-4a shows a symmetry check and repeatability for M = 0.8 and α = 0° for the Kulites® on ϕ = 0°, 90°, 180°, and 270°. The figure shows that the repeatability along each of the rows is excellent, but the lateral and vertical symmetry is not as good as expected. Generally a symmetric model with carefully installed Kulite® sensors will have less than 0.5 dB variation. Figure 12.2-4a shows 1.3 dB variation between the symmetrically arranged sensors in the flow reattachment region (x = 22–27 inches). Figures 12.2-4b through c show similar variations in Cp_{rms} for conditions where the values should be identical. Figure 12.2-4b shows the Cp_{rms} distributions along ϕ = 0°, 90°, 180°, and 270° for $\boldsymbol{\alpha}$ and $\boldsymbol{\beta}$ angles of attack and sideslip that put the sensor row on the windward side of the model at 4° incidence angle (α or β). In this case, the scatter in the flow-reattachment region is ~1 dB, while it is around 2.5 dB on the payload section.

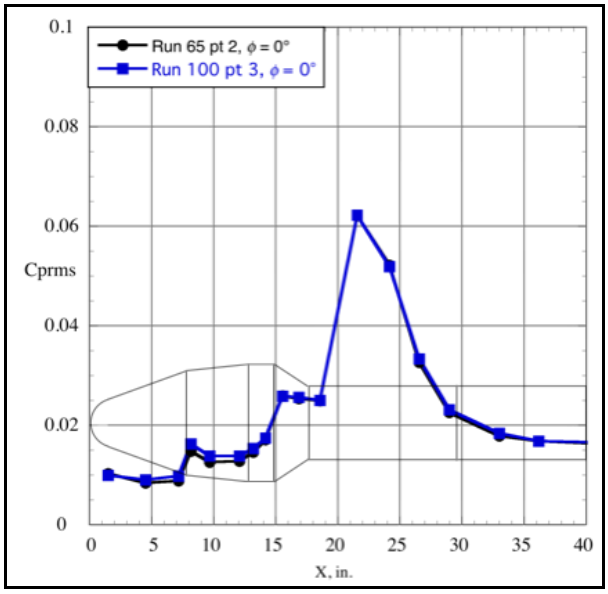

Figure 12.2-3a. Cp_{rms} Repeatability along $\phi = 0°$—Run 65 pt 2 versus Run 100 pt 3; M = 0.60, $\alpha = 4°$, Re = 3×10^6

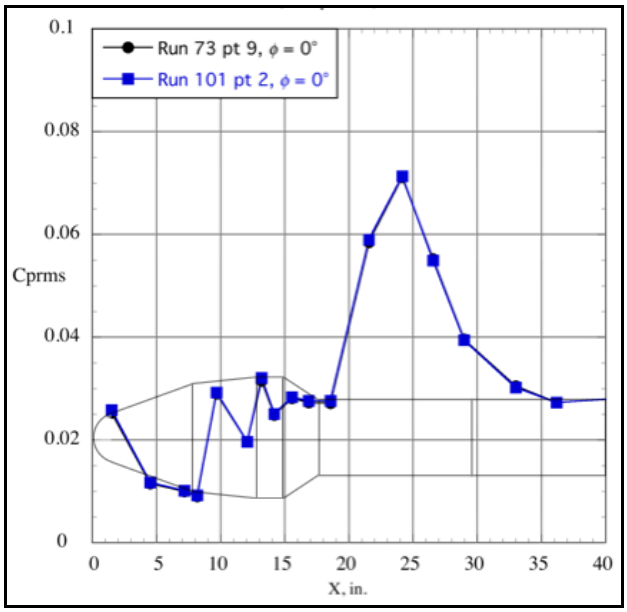

Figure 12.2-3b. Cp_{rms} Repeatability along Top ($\phi = 0°$)—Run 73 pt 9 versus Run 101 pt 2; M = 0.80, $\alpha = 0°$, Re = 3×10^6

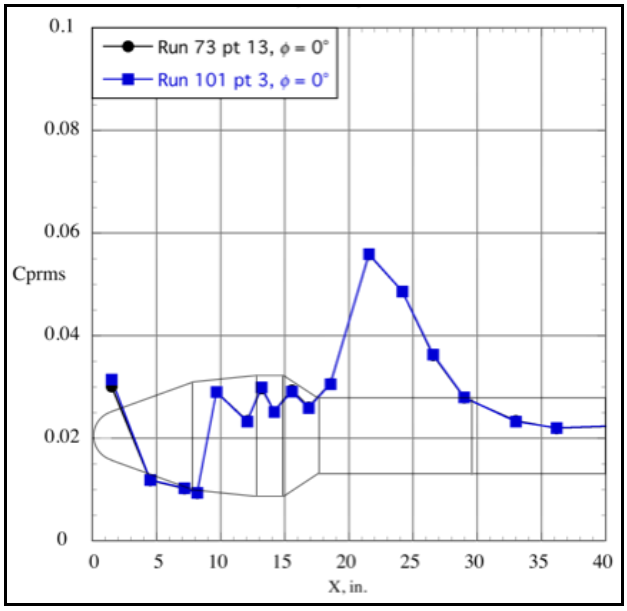

Figure 12.2-3c. Cp_{rms} Repeatability along Leeward Side (ϕ = 0°)—Run 73 pt 13 versus Run 101 pt 3; M = 0.80, α = 4°, Re = 3×10^6

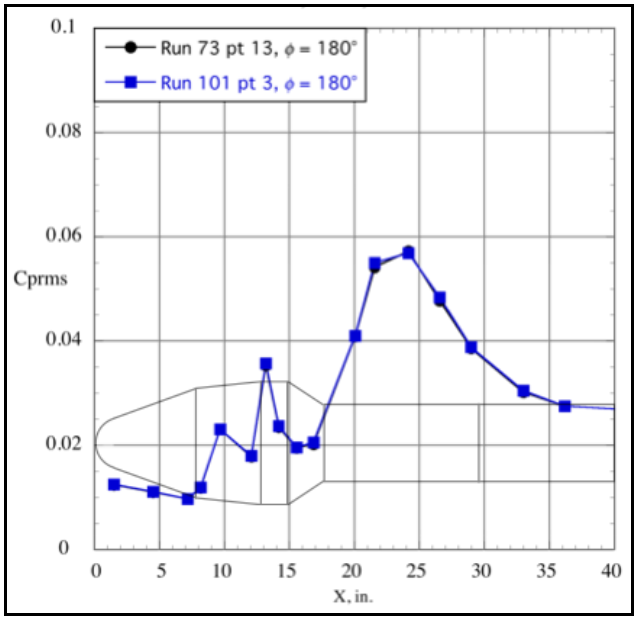

Figure 12.2-3d. Cp_{rms} Repeatability along Windward Side (ϕ = 180°)—Run 73 pt 13 versus Run 101 pt 3; M = 0.80, α = 4°, Re = 3×10^6

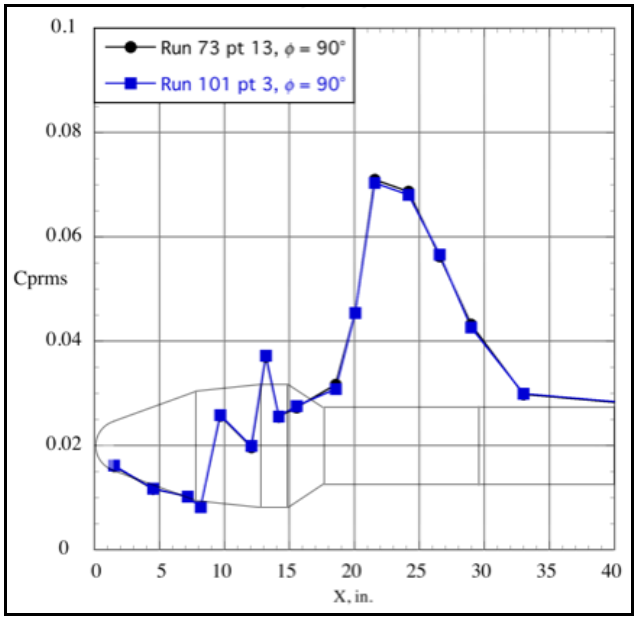

Figure 12.2-3e. Cp_{rms} Repeatability along Model Side (ϕ = 90°)—Run 73 pt 13 versus Run 101 pt 3; M = 0.80, α = 4°, Re = 3×10^6

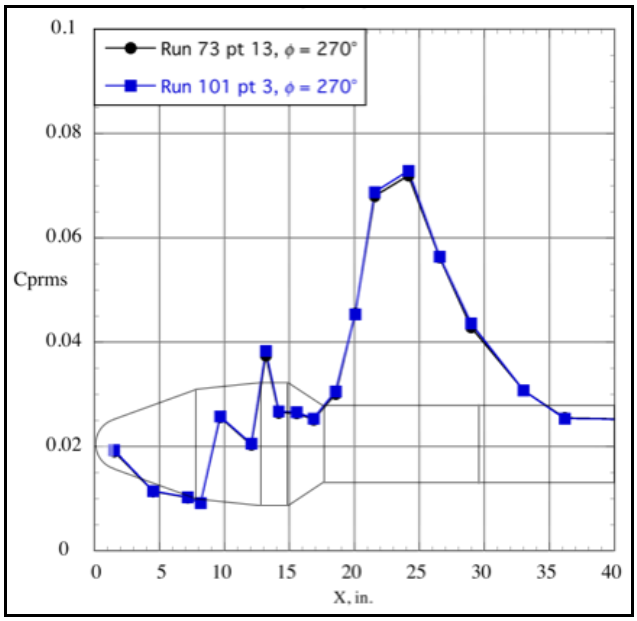

Figure 12.2-3f. Cp_{rms} Repeatability along Model Side (ϕ = 270°)—Run 73 pt 13 versus Run 101 pt 3; M = 0.80, α = 4°, Re = 3×10^6

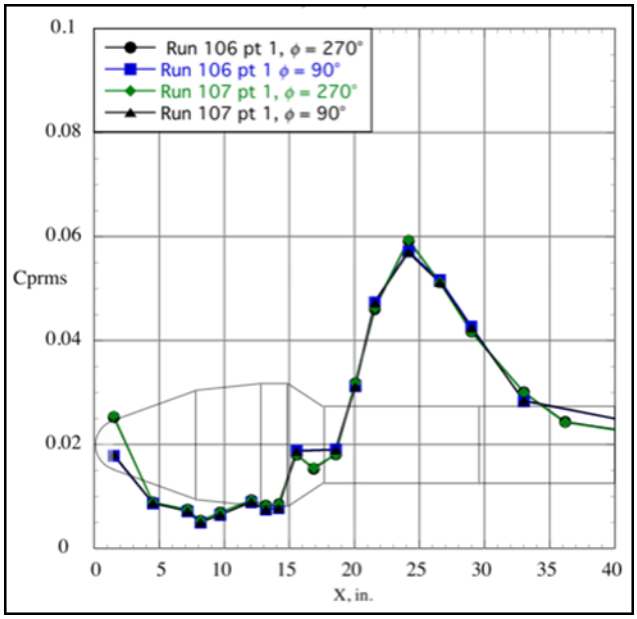

Figure 12.2-3g. Cp_{rms} Repeatability along Model Side (ϕ = 270°and 90°)—Run 106 pt 1 versus Run 107 pt 1; M = 1.10, α = 4°, Re = 3×10^6

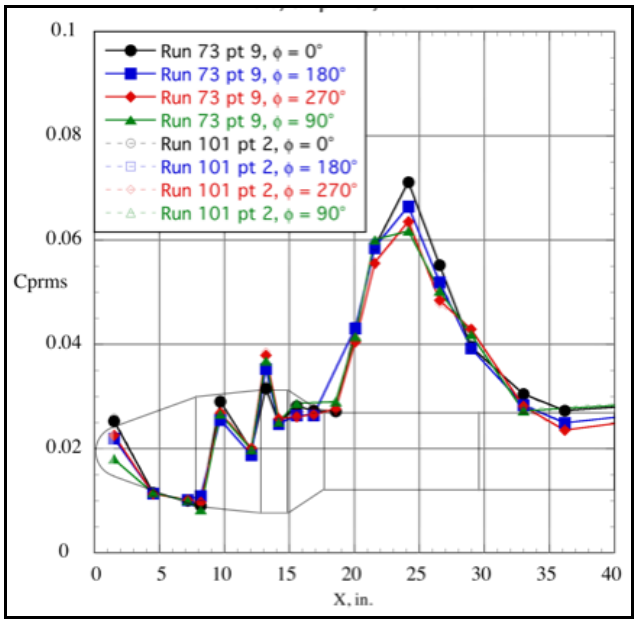

Figure 12.2-4a. Cp_{rms} Repeatability and Symmetry Check along Four Sides of Model (ϕ = 0°, 180°, 270°, and 90°)—Run 73 pt 9 and Run 101 pt 2; M = 0.80, α = 0°, Re = 3×10^6

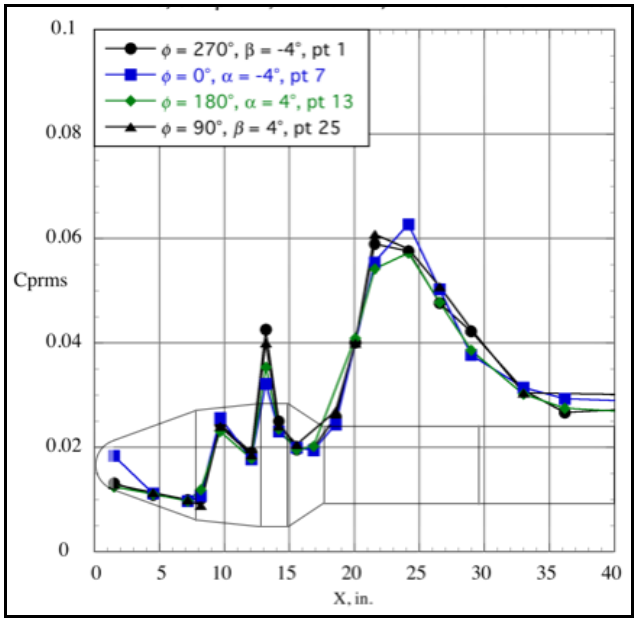

Figure 12.2-4b. Cp_{rms} Symmetry Check along Four Sides of Model (ϕ = 0°, 180°, 270°, and 90°)— Run 73; M = 0.80, Re = 3×10^6

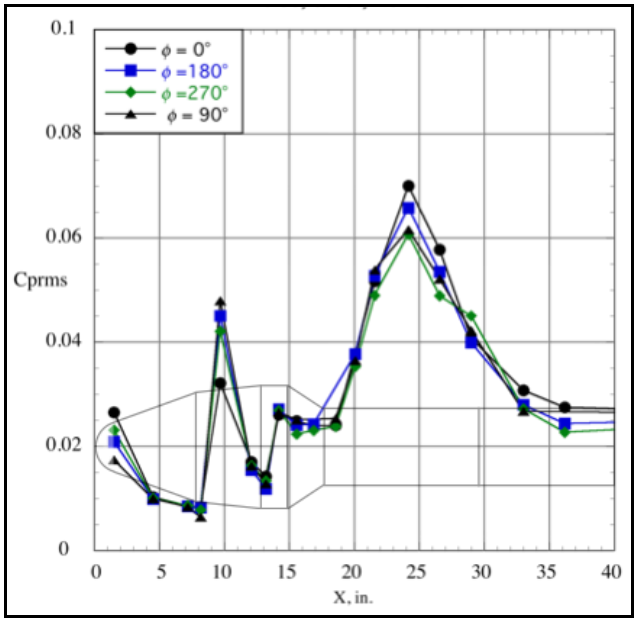

Figure 12.2-4c. Cp_{rms} Symmetry Check along Four Sides of Model (ϕ = 0°, 180°, 270°, and 90°)— Run 74 pt 9; M = 0.85, α = 0°, Re = 3×10^6

The variation in Cp_{rms} levels measured by different sensors that should be identical is likely caused by differences in the uPSP base coat edges around the Kulite® sensors. Figure 12.2-5 is a close-up image of several Kulite® sensors at x = 24.16-inch station (station 14).

While not obviously different to the eye, the edges of the paint around the sensors is measurably different. Profilometer measurements across a typical sensor installation are shown in Figure 12.2-6. The height of the paint step on the sensor downstream and upstream edges is ~0.00125 inch and ~0.0006 inch, respectively. Measurements across several other sensors showed similar heights and height differences between opposite edges. The maximum step height measured was ~0.0022 inch. Work by Hanly [ref. 13] showed that sensors protruding above the surrounding model surface distances of 0.002- to 0.004-inch measure pressure fluctuations that are high by 1 dB compared with flush mounted sensors. The measurement scans show the surface does not simply step down from the paint surface to the sensor holder. The paint edge has a narrow area of rapid increase in thickness approaching the edge, followed by a rapid drop to the holder surface. The variation in the paint-edge height and paint edges' locations relative to the sensor holes is sufficient to cause the level of inconsistency noted. Future testing with uPSP should include larger masking dots than the outer diameter of the Kulite® holder so the paint edges can be adequately smoothed.

Figure 12.2-5. Kulite® Sensors and Holders

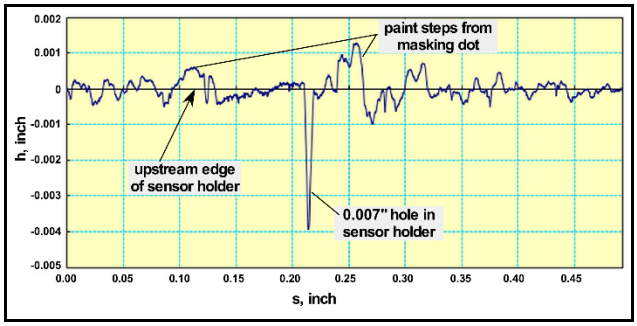

Figure 12.2-6. Surface Profile across Kulite® Sensor Holder K14-32

12.2.1 Effect of Faired Flange Joint on Local Pressure Fluctuations

Flange joints, even minimal protuberances, generally increase the local aeroacoustic levels. One goal of the test was to measure the acoustic-level changes in the vicinity of the flanges using the Kulite® sensors. Figure 12.2.1-1 shows the effect of the flange joints on the local fluctuating pressure. Figure 12.2.1-1a shows the Cp_{rms} at M = 0.92. The forward flange has the largest effect, doubling the fluctuating pressure upstream of the flange. The rms increase at the upstream sensor is the same for one or two flanges. The only effect of the second flange at this condition is to extend the region of elevated pressure fluctuations further downstream. For a low supersonic Mach number, the effect is similar with the upstream flange having a larger effect at the furthest upstream measurement location than at M = 0.92 but generating about the same maximum Cp_{rms} levels as it did at M = 0.92.

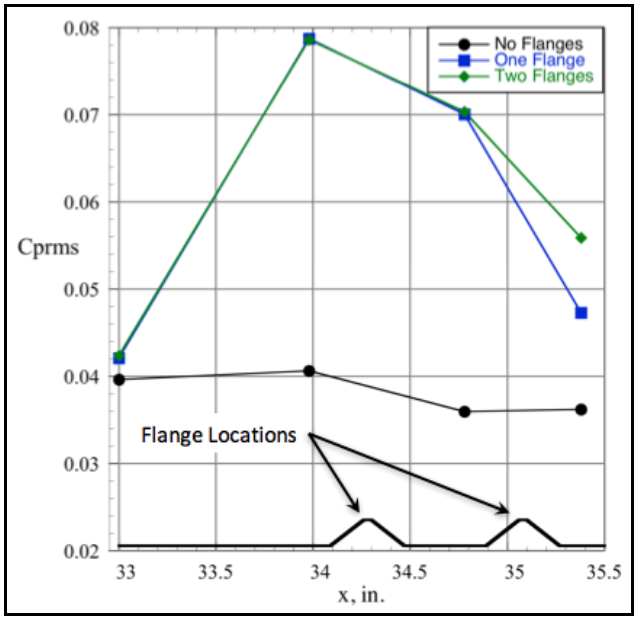

Figure 12.2.1-1a. Effect of Flanges on Cp_{rms}—Pressure Sensors at $\phi = 45°$; $M = 0.92$, $\alpha = -4°$, $Re = 3\times10^6$

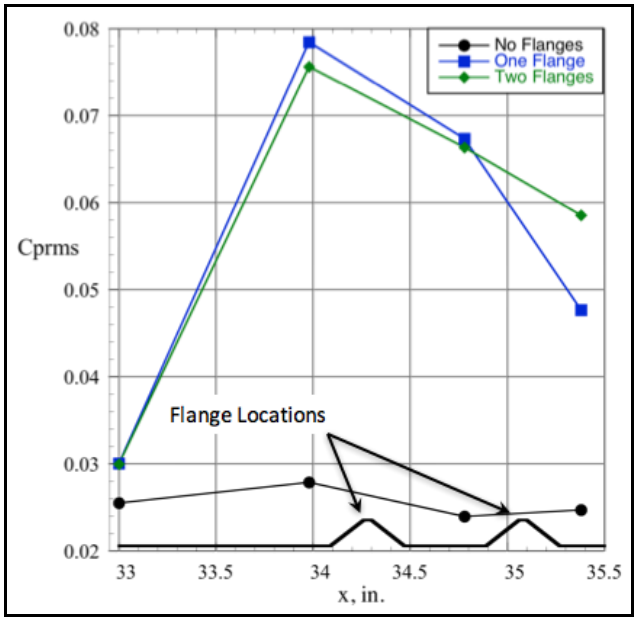

Figure 12.2.1-1b. Effect of Flanges on Cp_{rms}—Pressure Sensors at $\phi = 45°$; $M = 1.1$, $\alpha = -4°$, $Re = 3\times10^6$

12.3 Unsteady Pressures from uPSP

The uPSP provided a wealth of information about the flow over the model. The uPSP data were processed using the established method outlined in Section 10.3.1 using pre-test calibrations and in situ wind-off images at ~5 different static pressures. The final reduced data was mapped onto multiple surface grids with varying point densities in the axial and azimuthal directions. Figures 12.3-1a and b show portions of the grid, which contained a total of ~300,000 points. One of the lessons learned was that transferring the unsteady pressure data at this many grid points was burdensome and inefficient. An evaluation of the resolution requirements is discussed in the following section.

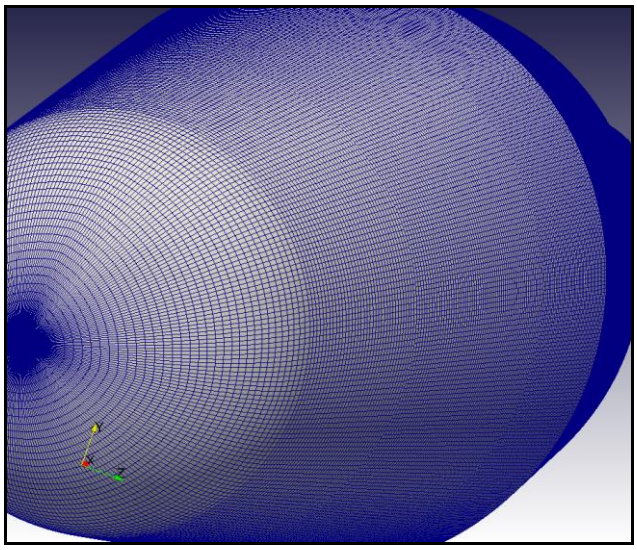

Figure 12.3-1a. Surface Grid onto Which the Traditionally Processed uPSP Data Were Mapped—Nose and Upper Payload Fairing Section

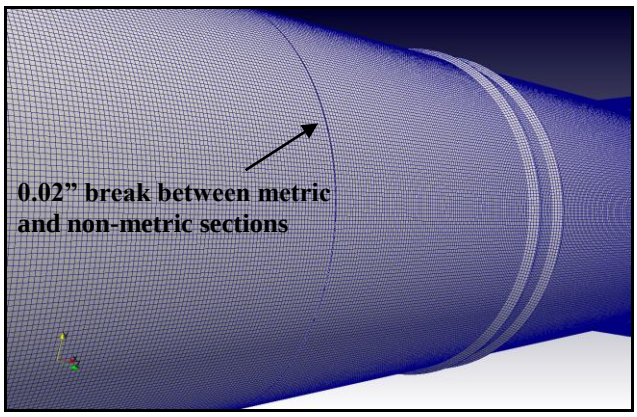

Figure 12.3-1b. Surface Grid onto Which the Traditionally Processed uPSP Data Were Mapped—Aft Part of Metric Section and Flange Rings

This section will primarily present results for M = 0.92, which are representative of a high-buffet flight environment.

12.3.1 uPSP Comparisons with Kulite® Signals

The first comparison between the uPSP and Kulite® transducers is the spectra determined from each method. Figure 12.3.1-1 shows the numbering of the Kulite® measurement stations. Adjacent to each of the Kulites® on the model, a region of uPSP was sampled. For the conventional processing, a 5×5 array of pixels were averaged at every time step to obtain a "virtual Kulite®" pressure time history. The spectra for the virtual and actual Kulite® signals were compared to obtain an idea of the ability of the uPSP to capture critical characteristics of the unsteady pressures acting on the model. Figure 12.3.1-2 shows one comparison for Kulite® 03-08. This plot is excerpted from a larger set of plots showing the comparisons for stations 3-17. At station 3, the uPSP does a poor job measuring the unsteady pressure, missing the levels by more than 2 orders of magnitude in some frequencies.

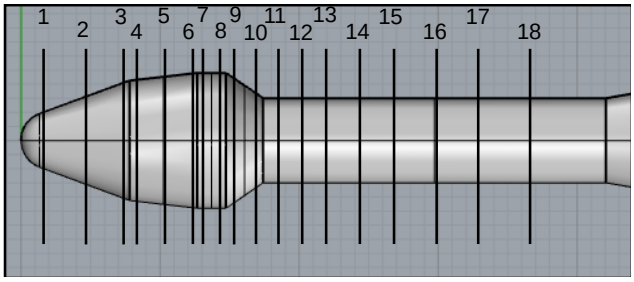

Figure 12.3.1-1. Numbering of Kulite® Measurement Stations

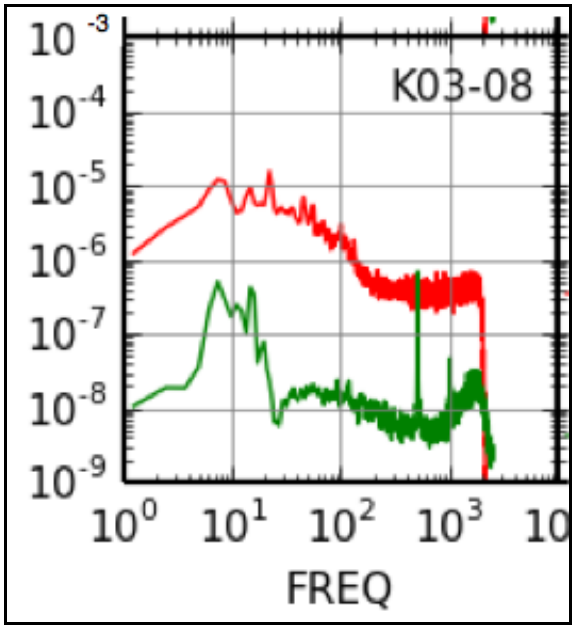

Figure 12.3.1-2. Kulite® K03-08 (green) versus Virtual Kulite® (red) Power-Spectral Density (psd) for Run 171 Point 1—M = 0.92, α = –4°, Re = 3×106—uPSP Data Acquired at 5 kHz; Vertical Axis Units Are psi²/Hz

A more complete understanding is shown in Figures 12.3.1-3a through d. The notable trend is that the agreement between uPSP and the Kulite® measurements improves with the overall level of pressure fluctuations. There appears to be a noise floor to the uPSP measurements between about 10^{-5} and 10^{-6} psi^2/Hz. The noise floor for the Kulite® sensors is lower so in the quiet payload fairing flow regions, uPSP is not adequate. Once the fluctuating pressures exceed 10^{-5} psi^2/Hz, in particular at station 8 and beyond, the agreement between the uPSP and Kulites® measurements is good across the entire frequency range to the maximum frequency analyzed (i.e., 2 kHz). Several stations had failed Kulite® sensors, so there are frames in the plots where there is only a red (i.e., uPSP virtual Kulite®) curve.

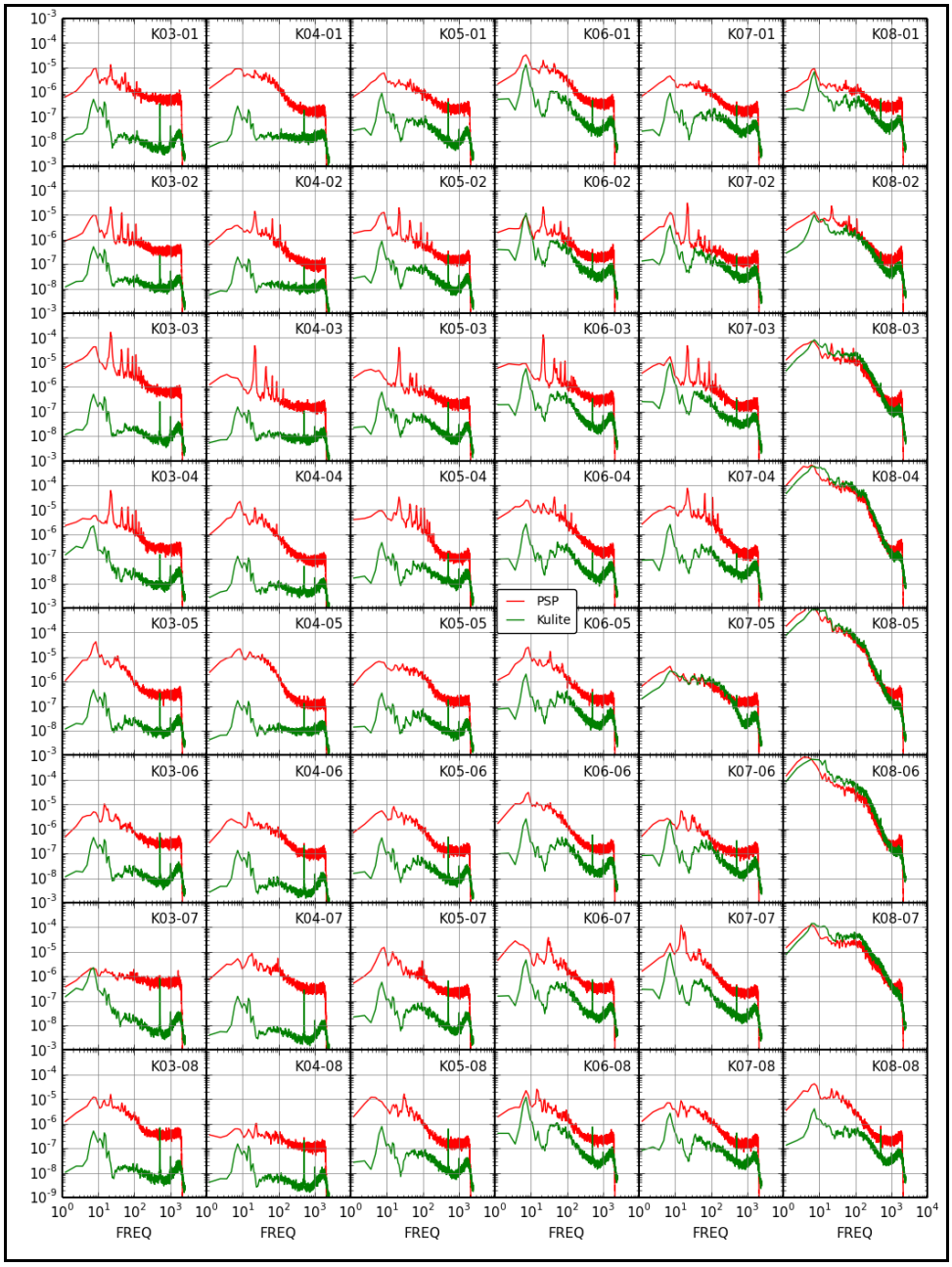

Figure 12.3.1-3a. uPSP (red) versus Virtual Kulite® (green) psd for Run 171 Point 1—M = 0.92, α = -4°, Re = 3×10⁶; uPSP Data Acquired at 5 kHz (measurement stations 3 through 8); Vertical Axis Units Are psi²/Hz

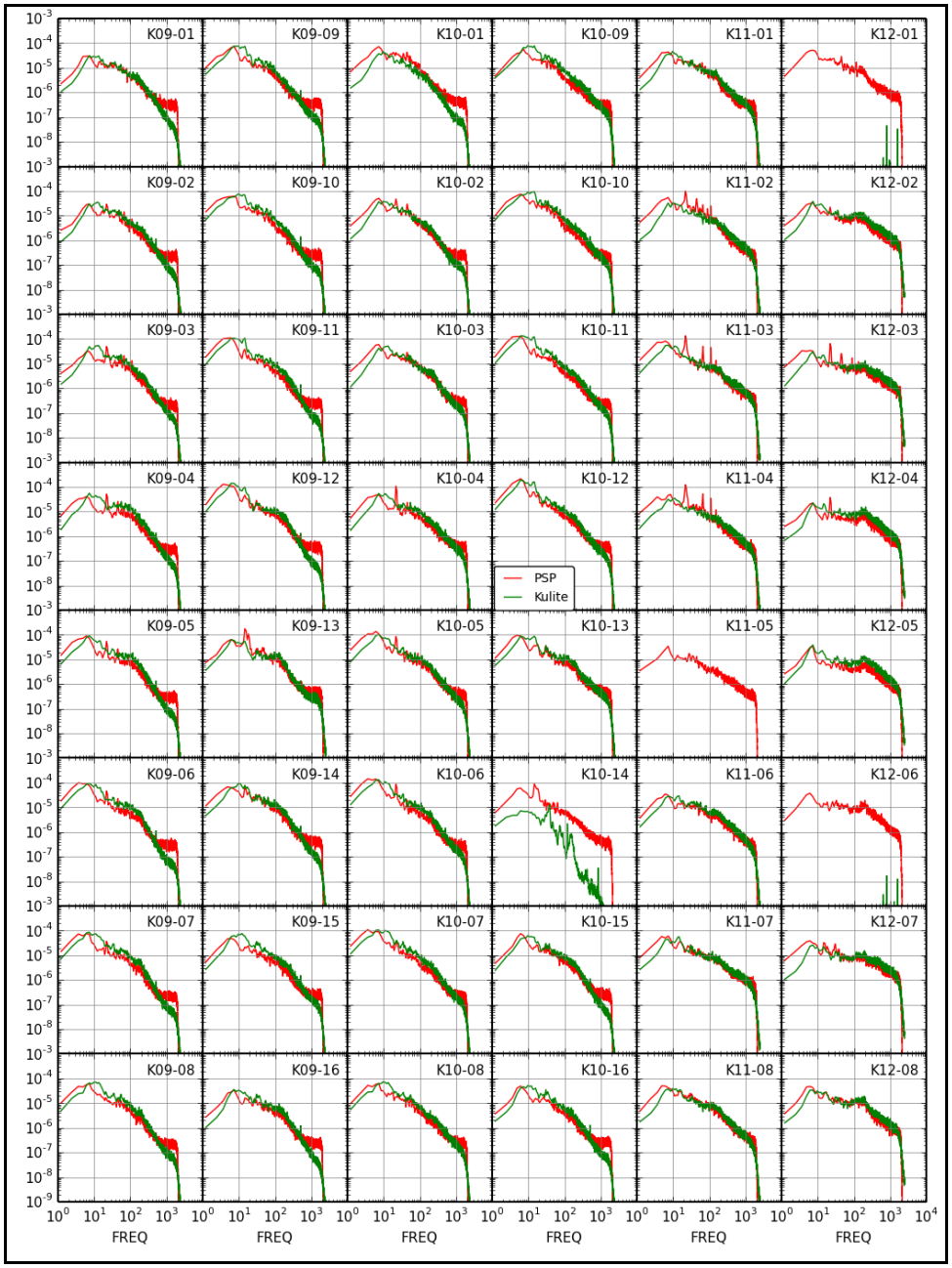

Figure 12.3.1-3b. uPSP (green) versus Virtual Kulite® (red) psd for Run 171 Point 1—M = 0.92, α = –4°, Re = 3×10⁶; uPSP Data Acquired at 5 kHz (measurement stations 9 through 12); Vertical Axis Units Are psi²/Hz

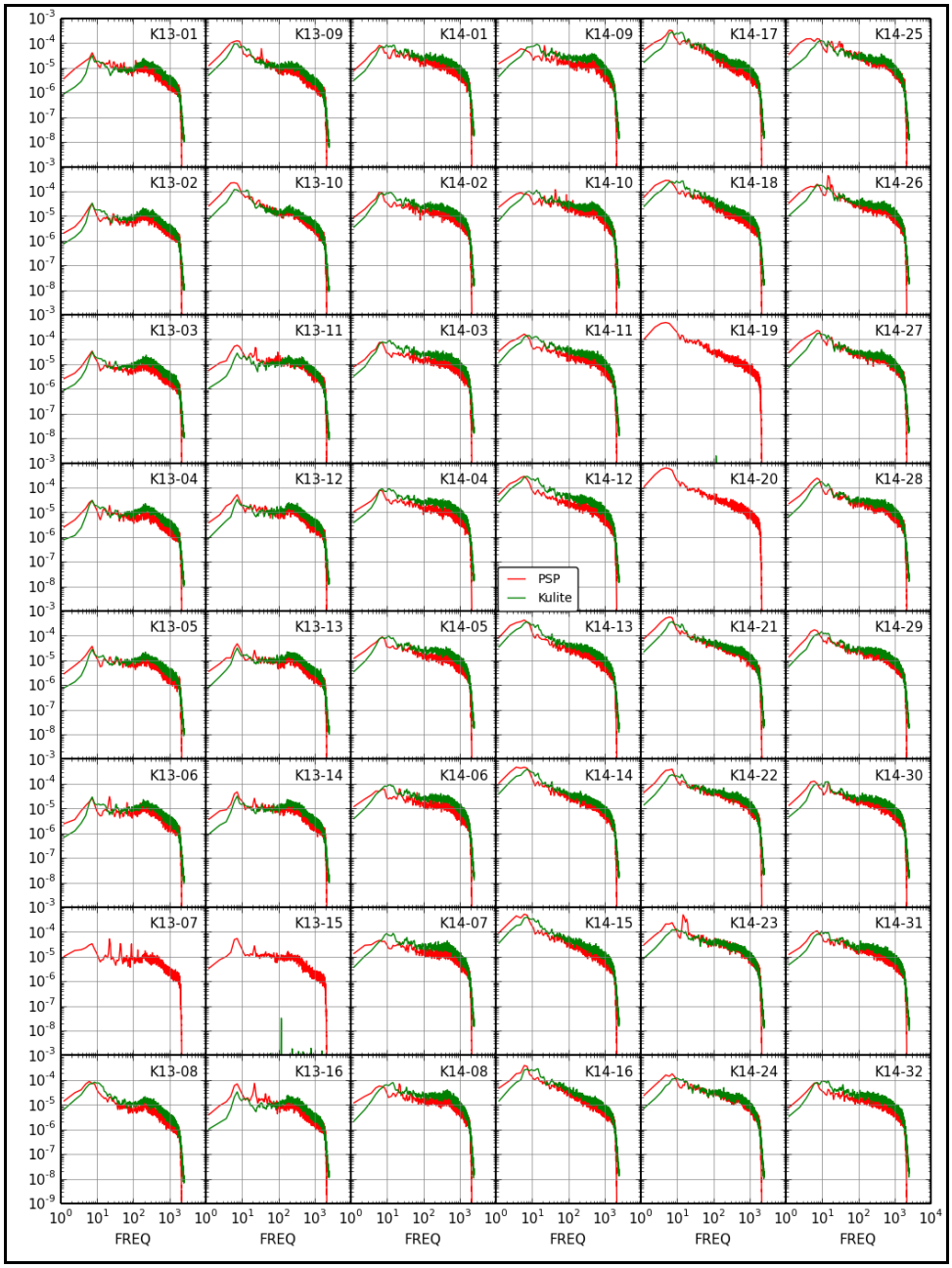

Figure 12.3.1-3c. uPSP (green) versus Virtual Kulite® (red) psd for Run 171 Point 1—M = 0.92, α = −4°, Re = 3×10⁶—uPSP Data Acquired at 5 kHz (measurement stations 13 through 14); Vertical Axis Units Are psi²/Hz

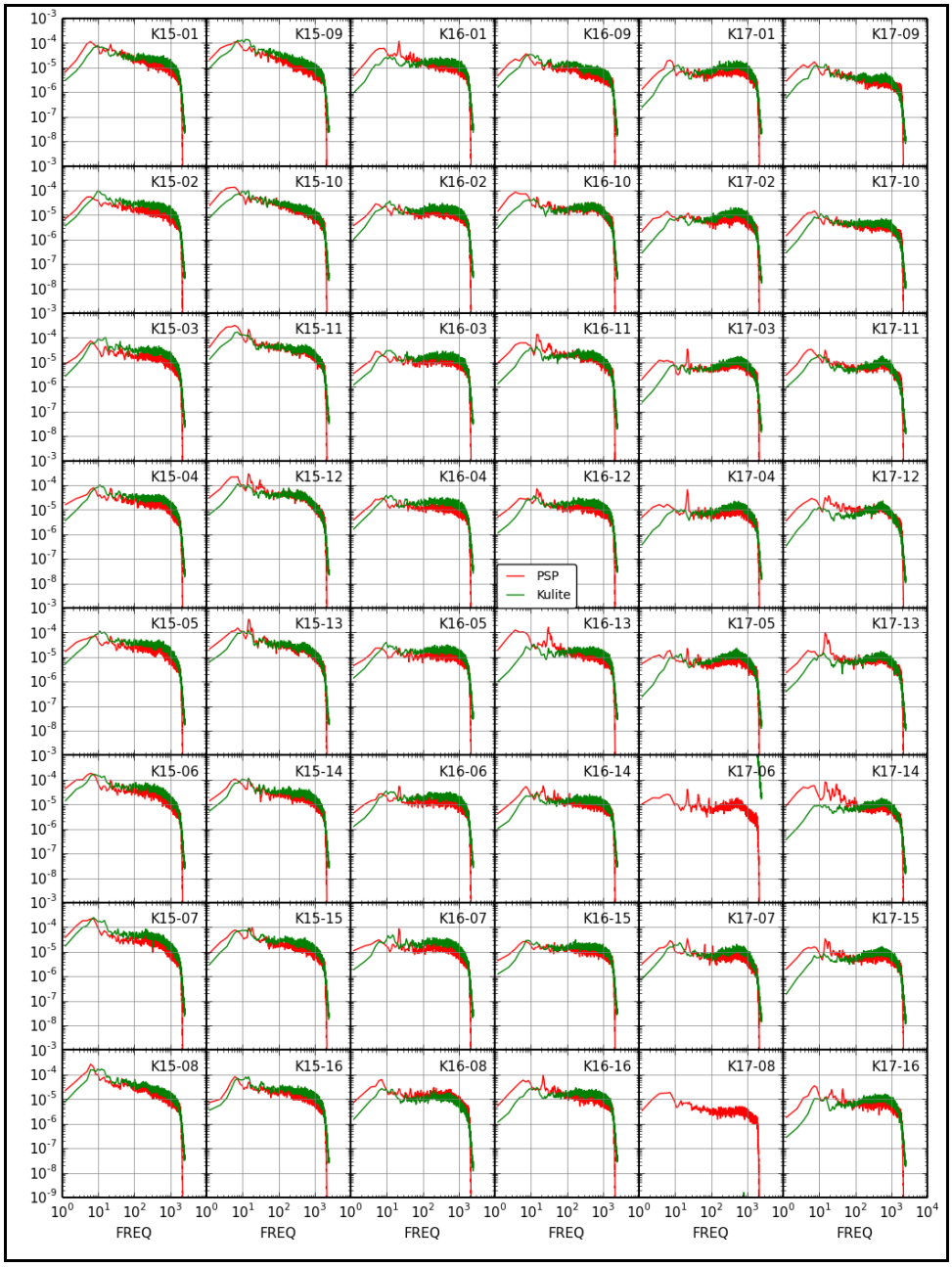

Figure 12.3.1-3d. uPSP (red) versus Virtual Kulite® (green) psd for Run 171 Point 1—M = 0.92, α = −4°, Re = 3×10⁶; uPSP Data Acquired at 5 kHz (measurement stations 15 through 17); Vertical Axis Units Are psi²/Hz

Figure 12.3.1-4 shows the same comparisons between Kulite® sensors and uPSP for different Mach numbers. These comparisons are for sensor 3 at stations 3 through 8. The general trend of

better agreement with larger fluctuating pressures, as in Figure 12.3.1-3 a through d, is consistent with having a noise floor below, which the uPSP is unable to detect due to camera noise. Once the fluctuating pressure level rises above this floor, the spectra from the two measurement techniques match more closely. The axial location where the fluctuating pressures increase changes with Mach number. For the supersonic cases, M = 1.02 and 1.1, the fluctuating pressure is still low at station 8, while the subsonic and transonic Mach numbers show increased noise at station 8.

Given the apparent accuracy of the uPSP measurements, at least in regions of high pressure fluctuations, uPSP measurements open a range of options for analysis, from integrating directly to obtain the BFF to interrogating smaller areas to estimate loads on individual panels. Figure 12.3.1-5 shows surface pressure contours for M = 0.92, $\alpha = -4°$, at three consecutive time steps. The sample rate for these data is 5 kHz. Flow structures are visible in the pressure coefficient contours showing various sizes and pressure levels that can be seen traveling along the model.

The high spatial and temporal resolution of uPSP enables wavenumber-frequency analysis, an important data processing technique. Panda et al. [ref. 11] present arguments for using this analysis method based on data acquired for this assessment [ref. 12].

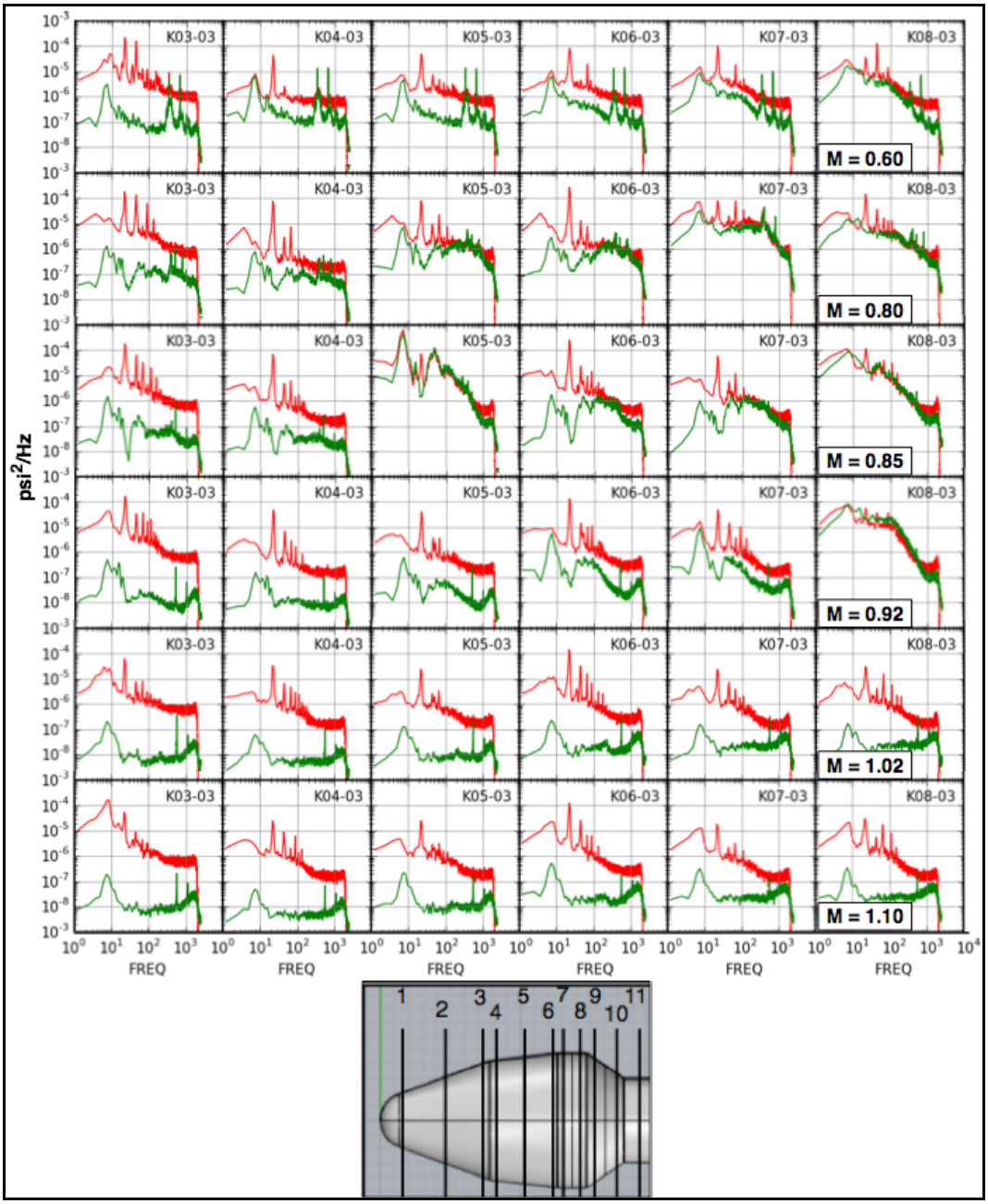

Figure 12.3.1-4. uPSP (red) versus Virtual Kulite® (green) psd for Different M at $\alpha = -4°$, $Re = 3\times10^6$; uPSP Data Acquired at 5 kHz (sensor 3 at Measurement Stations 3 through 8); Vertical Axis Units Are psi²/Hz

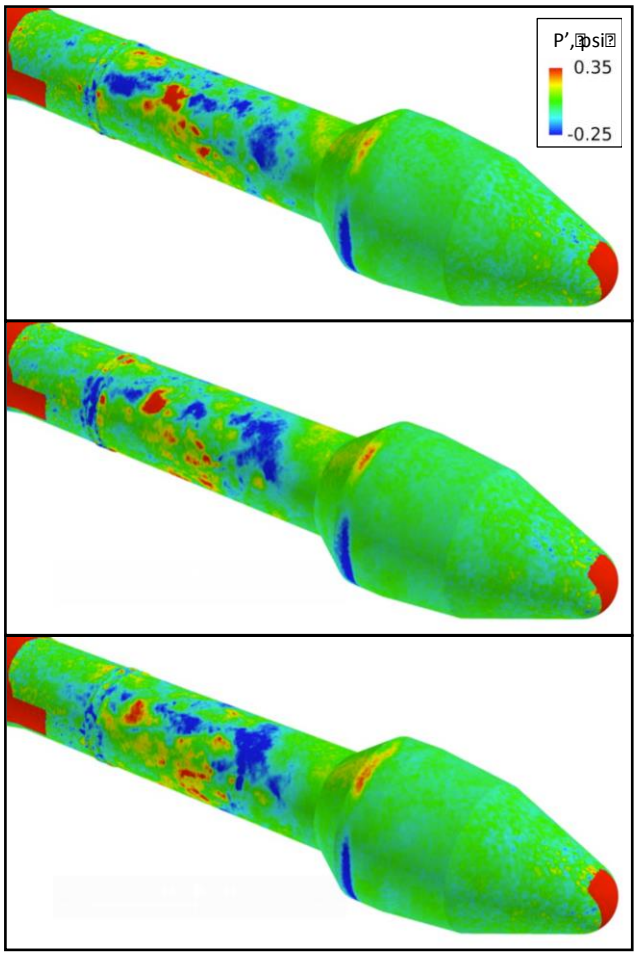

Figure 12.3.1-5. Fluctuating Pressure Distributions at Three Consecutive Time Steps—Run 170 Point 1; M = 0.92, α = –4°, Re = 3×10⁶

13.0 Unsteady Forces from Unsteady Pressure Integration

13.1 Simple Integration

The main focus of this assessment was to determine the accuracy of current integration techniques to estimate BFFs from sparse unsteady pressure data. The high-resolution uPSP data provided verification of the processing accuracy when the pressures from the "virtual Kulites®" were used in the analysis. Figure 13.1-1 shows a comparison of the rms section forces computed at each of the Kulite® stations. These simple integrations assume full coherence of the pressure over the area of influence. As the measurement density increases, this approximation becomes more accurate. Figure 13.1-1 shows that using either the Kulite® data or uPSP data at the Kulite® locations results in a large overestimate of the load at a given section. It is clear that simple integration assuming perfect coherence over the area of influence for each sensor leads to

over prediction of the actual loads. The dense uPSP grid should be sufficient to avoid the discretization errors, but more analysis is necessary to determine what grid density is sufficient to obtain sufficiently accurate estimation of the loads.

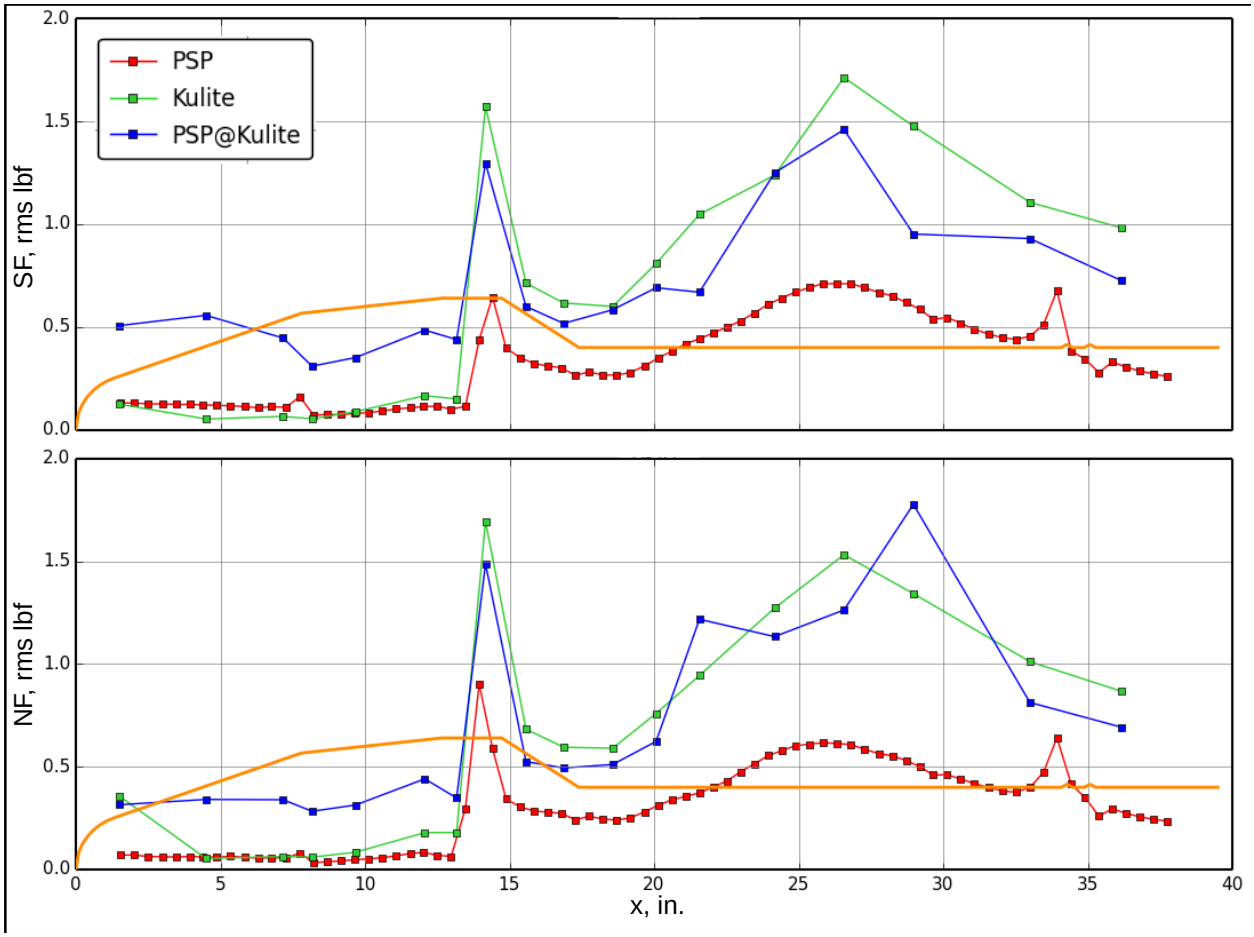

Figure 13.1-1. Integrated Section Pressure Forces Computed Using Simple Integration of Kulite® Signals, "Virtual Kulites®," and uPSP Grid—M = 0.92, α = –4°, Re = 3×10⁶

The integrated loads over the payload fairing show that the process of integrating noisy uPSP signals at high resolution results in relatively low forces similar to the forces computed using the Kulite® signals. Using the uPSP data at the Kulite® locations, however, results in much higher integrated forces. Determining why this uncorrelated noise integrates to higher resultant forces on the sparse grid is another area for future investigation.

An interesting feature in Figure 13.1-1 is the effect of the two flange rings on the side and normal force rms levels. The force rms levels increase upstream of the flanges and decrease downstream, appearing to match the downstream loads generated without the flanges at a relatively short distance of the second flange. Figure 13.1-2 shows the effect of one and two

flanges on the rms forces at the same test conditions as in Figure 13.1-1. A single flange (configuration 2) appears to affect the integrated loads over a more axial distance than do two flanges (configuration 3), but the peak integrated normal and side forces are the same for one or two flanges.

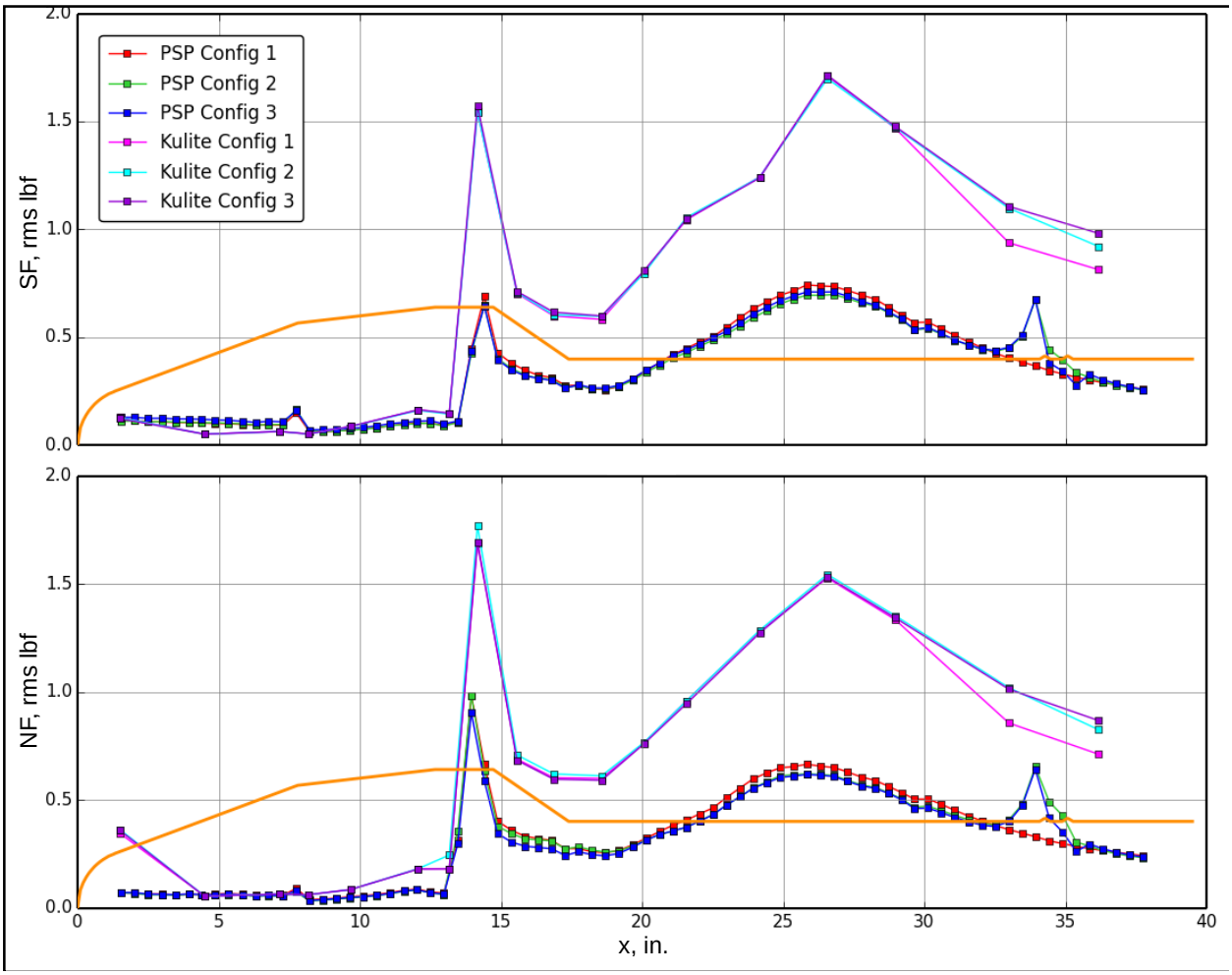

Figure 13.1-2. Effect of Faired Flanges on the Integrated Loads—M = 0.92, α = –4°, Re = 3×10⁶

Figure 13.1-3 shows the spectra of the model's section loads. Force spectra from both Kulite® transducers (without coherence adjustment) and uPSP signals are shown. In spite of the lack of agreement between the spectra of individual Kulites® and the adjacent uPSP pressures on the payload section (Figure 12.3.1-1), the spectra of the integrated forces are in relatively good agreement over the entire model, showing similar peaks and general shapes if somewhat different in level.

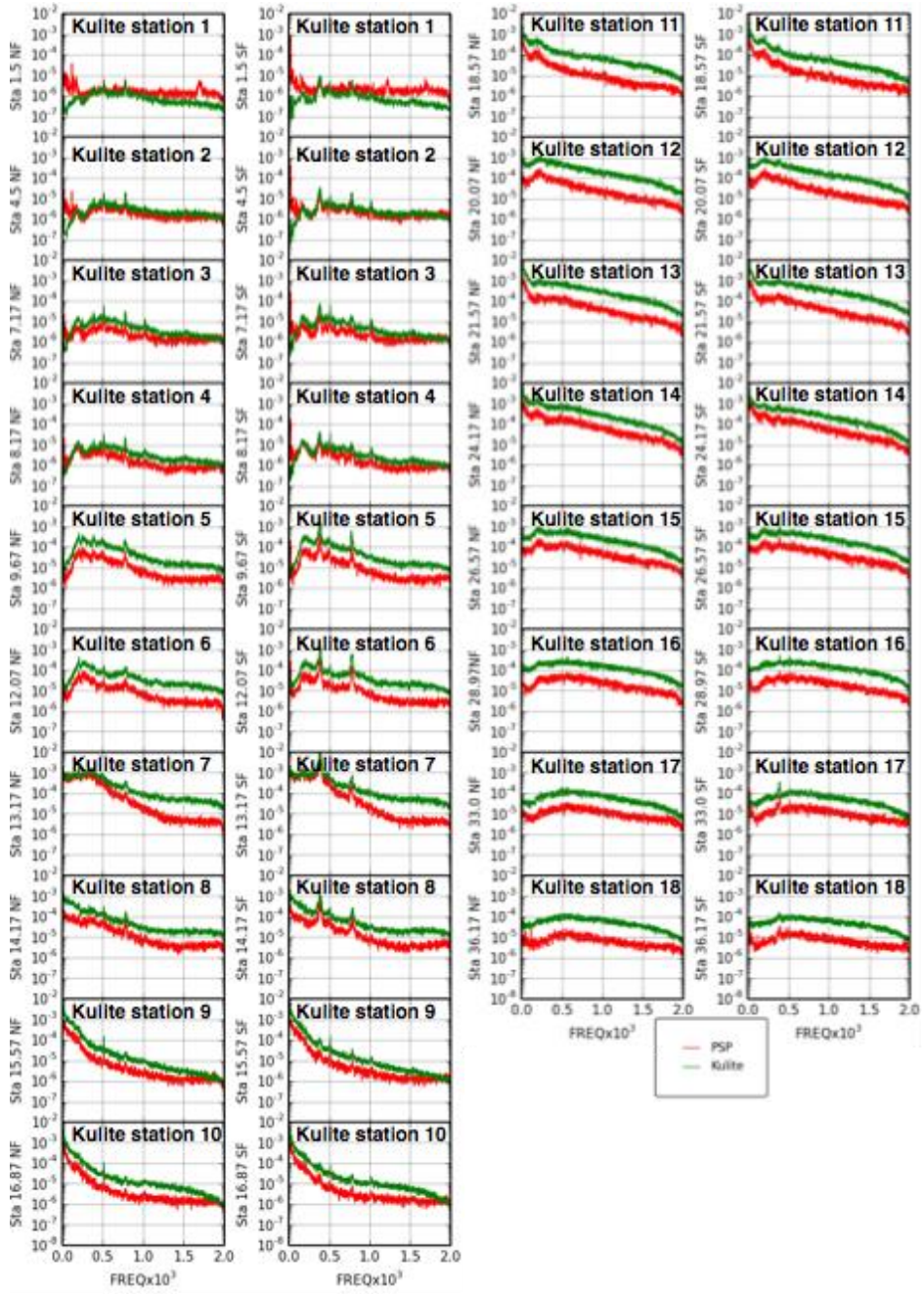

Figure 13.1-3. Spectra of Integrated Section Normal and Side Force Generated Using the Kulite® and uPSP Pressure-Time Histories—M = 0.92, α = –4°, Re = 3×10⁶

13.2 Comparison with Coherence-length Corrected Integration

An analysis determined the validity of BFFs developed by integrating sparse, discrete surface pressure measurements and adjusting the resultant loads using coherence factors. Three sets of BFFs were developed using both unsteady pressure transducer (PT) and uPSP data acquired at the same test condition. The three sets of BFFs are:

1. Discrete unsteady PT integration with longitudinal and azimuthal coherence factors developed using PT data
2. Discrete virtual PT (vPT) integration with longitudinal and azimuthal coherence factors developed using vPT data—vPTs are uPSP measurements in the vicinity of pressure transducers
3. Direct surface pressure integration using uPSP data.

Sets 1 and 2 were produced using the BFF development procedure outlined in Reference 10. In both cases, the same aerodynamic regions were used and determined by a coefficient of determination (R^2) moving block analysis. A representative output from this analysis conducted based on mean coherence in the 3 to 400 Hz range is presented in Figure 13.2-1. The aerodynamic boundaries are based on where the R^2 dips and then increases, signifying a change in the predominant aerodynamic phenomena. By examining similar plots produced with various frequency range data, five aerodynamic zones were identified for this test condition and are presented in Table 13.2-1. These same regions are used to develop both PT-based and vPT-based BFFs.

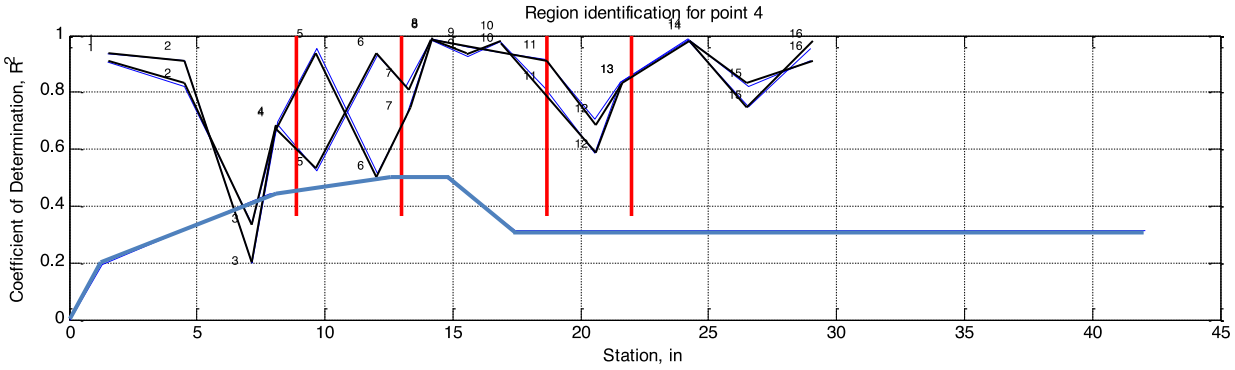

Note: Aerodynamic region boundaries are depicted in red.

Figure 13.2-1. Aerodynamic Region Identification Based on Transducer-Based Sectional Loads, 3 to 400 Hz

Table 13.2-1. Aerodynamic Region Definitions

Aerodynamic zone number	1	2	3	4	5
Starting transducer station number	1	4	7	13	16
Ending transducer station number	3	6	12	15	18

13.2.1 Coherence Factors

Longitudinal and azimuthal coherence factors were calculated using PT and vPT data using procedures outlined in Reference 10. The longitudinal coherence factors are presented in Figure 13.2.1-1. Coherence factors based on various frequency ranges are differentiated with different colors, while PT-based coherence factors are depicted by solid lines and vPT-based factors by dashed lines. Forward of transducer station 7, the coherence factors produced by the two sets of data differ significantly, indicating that the uPSP data on the forward portion of the model may not be reliable. From station 7 aft, the longitudinal coherence factors based on both data sets agree.

Azimuthal coherence angles for stations 2 through 17 are presented in Figure 13.2.1-2. Coherence angles are presented in lieu of coherence factors since, within a transducer ring, coherence factors can vary from transducer to transducer depending on spacing between functional transducers while the coherence angle is assumed constant. The vPT-based coherence angles are significantly different from the PT-based coherence angles at stations forward of station 8, echoing the trend noted for the longitudinal coherence factors. Unlike the longitudinal coherence factors, the vPT-based coherence angles for stations 8 through 17 are always larger than their PT-based counterparts, although they follow the same trends.

A possible cause for this higher coherence angle trend may be the PSP noise floor. The vPT-based coherence angles for stations 1 through 7 are roughly constant. Since the PSP measurements on the model's forward portion did not clearly resolve the unsteady pressures, the near constant coherence angles indicate that they may be an artifact of the uPSP measurement noise floor. On average, the coherence angles on the aft half of the model seem to be of the same magnitude as the noise floor, with deviation from this mean value that follows the trends in the PT-based coherence angles. Further analysis should be conducted to substantiate or refute this observation.

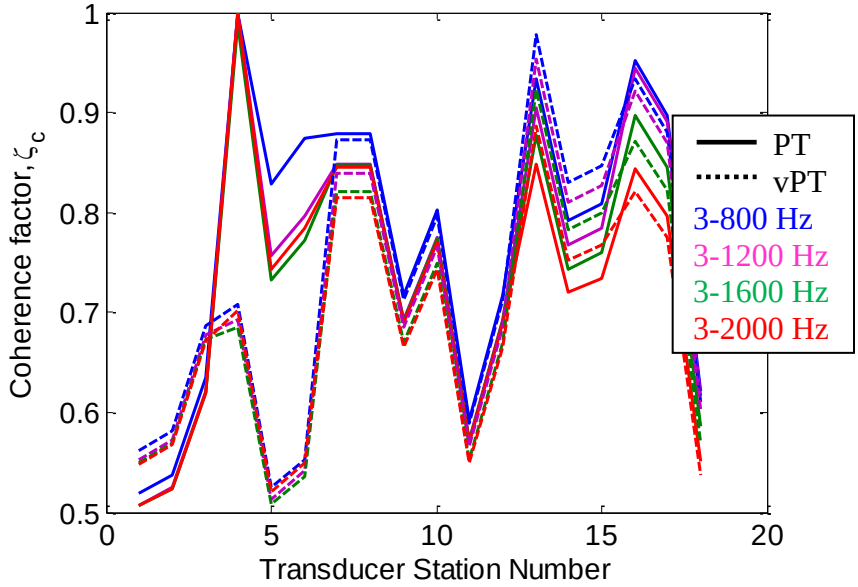

Figure 13.2.1-1. Comparison of Longitudinal Coherence Factors Calculated Using Unsteady PT and vPT Data

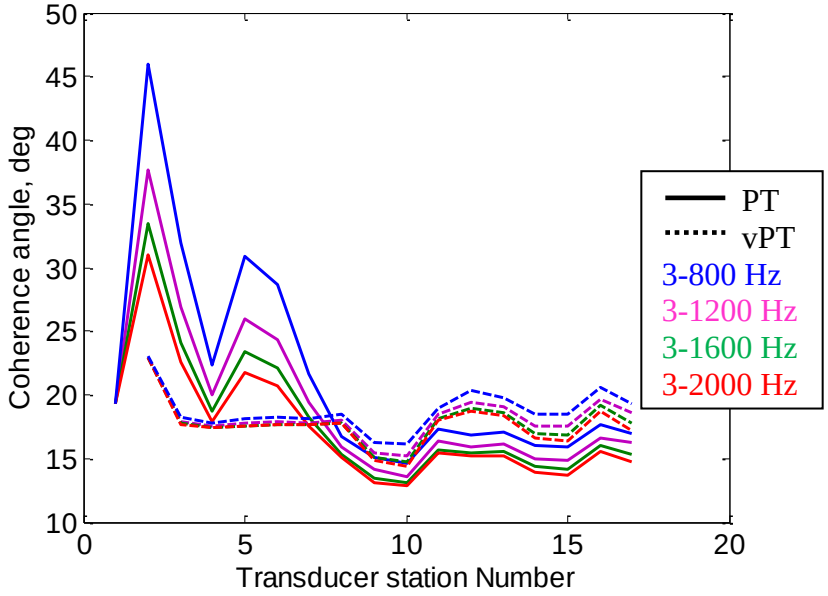

Figure 13.2.1-2. Comparison of Azimuthal Coherence Angles Calculated Using Unsteady PT and vPT Data

13.2.2 Root-Mean-Square Values of Buffet Forcing Functions

The rms values of BFFs for stations 2 through 17 are presented in Figure 13.2.2-1. Data for stations 1 and 18 are not presented because of the partial PSP coverage of the integration areas associated with those transducer rings. Likewise, only the BFFs for stations 8 through 17 will be discussed since the PSP did not resolve the unsteady pressures on the forward section of the model.

In Figure 13.2.2-1, the PT-based BFFs are represented by blue circles, the vPT-based BFFs by red squares, and the PSP surface pressure integrated BFFs by green diamonds. In general, the three sets of BFFs follow the same trends on the aft half of the model. The rms values of vPT-based BFFs are usually higher than those for the PT-based BFFs. These higher values are primarily due to the larger azimuthal coherence factors.

This assertion was substantiated by developing vPT-based BFFs, but using PT-based coherence factors. The rms values for this set of hybrid BFFs are represented by brown triangles in Figure 13.2.2-1. A comparison of the rms values of the PT-based BFFs (blue circles) and the hybrid BFFs (brown triangles) indicates that integrating vPT pressure time histories results in smaller fluctuating loads. Furthermore, the vPT-based azimuthal coherence factors are always larger than their PT-based counterparts, while the vPT-based longitudinal coherence factors are higher or lower than their PT-based counterparts, depending on the longitudinal station. This observation indicates that the azimuthal coherence factors play a more dominant role in affecting the BFF load magnitudes than the longitudinal coherence factors.

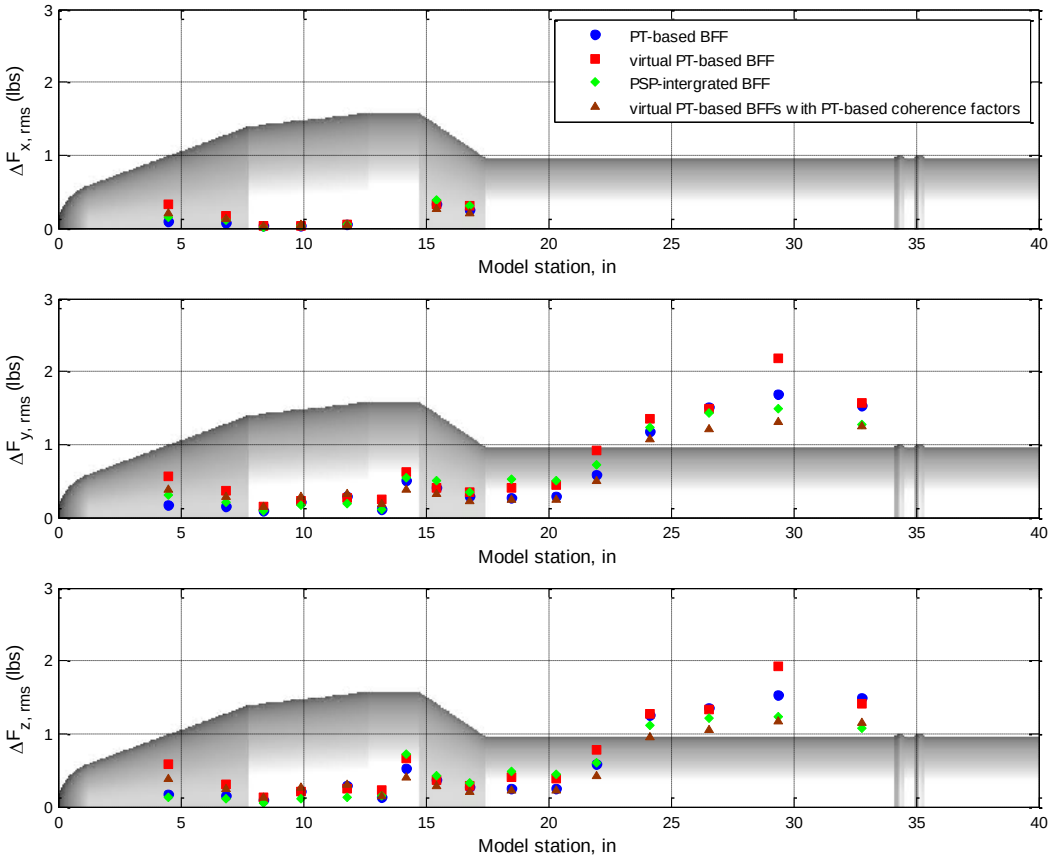

Figure 13.2.2-1. BFF rms Values

13.2.3 PSD Functions

The PSD functions of three sets of BFFs are presented in Figure 13.2.3-1. PSDs of PT-based BFFs are presented in blue, vPT-based BFFs in red, and PSP surface pressure integrated BFFs in green, in addition to PSDs for lateral and vertical components for stations 2 through 17. PSDs of PT-based BFFs for stations 2 through 7 differ significantly in magnitude and shape from the vPT-based BFFs and uPSP BFFs. These differences are most likely due to the PSP noise floor issue discussed previously.

The three sets of PSDs for stations 8 through 17 exhibit similar trends. A comparison of the PSDs for the vPT-based BFFs and the PSP-integrated BFFs indicates that, in general, the vPT-based BFFs underpredict the low-frequency PSDs while overpredicting the higher frequency signals. The crossover frequency usually occurs in the 400 to 800 Hz range.

This overprediction/underprediction trend and crossover frequency range may be associated with the calculation of coherence factors and their application in development of the BFFs. The coherence factors are determined using average coherence over various frequency ranges and

choosing the frequency range that produces the most conservative coherence factor. In the case of this analysis, this frequency range was 3 to 800 Hz (see Figures 13.2.1-1 and 13.2.1-2). The effect of multiplying the BFF/pressure time histories by these coherence factors is not limited to this frequency range—the magnitude of the PSDs at all frequencies are affected. Therefore, for higher frequencies, where the coherence is generally lower, the coherence factors based on the 3 to 800 Hz range are too high, resulting in overconservative BFF frequency content. Conversely, the averaged coherence approach in the 3 to 800 Hz range underestimates the coherence factors for frequencies that exhibit the highest coherence resulting in underpredicted BFFs at these frequencies. Further analysis will substantiate or refute this hypothesis. A more accurate calculation and application of coherence factors could be developed using of wavelet analysis in lieu of a frequency-based approach.

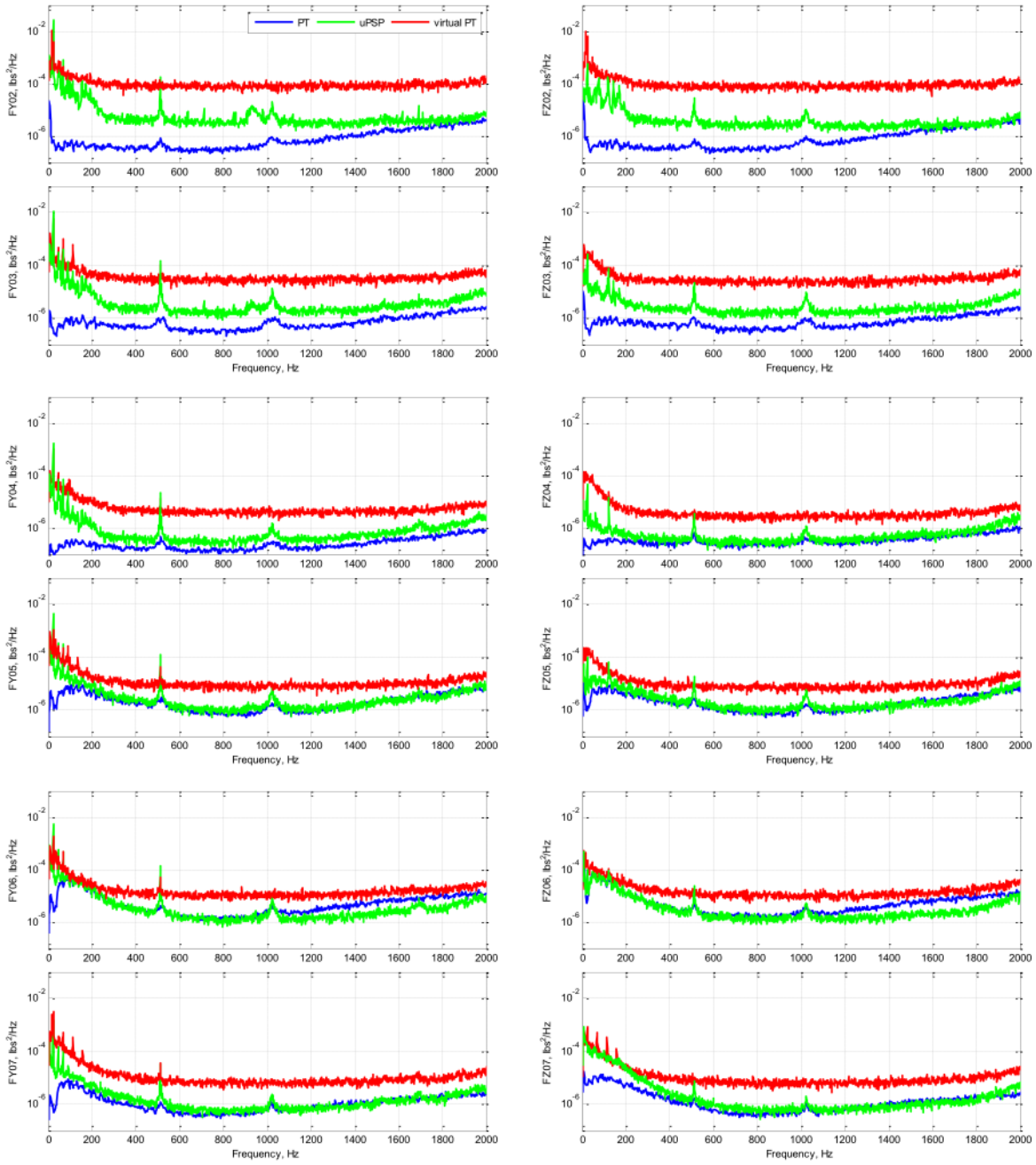

Figure 13.2.3-1. BFF PSDs—FY (Side Force or SF) and FZ (Normal Force or NF)

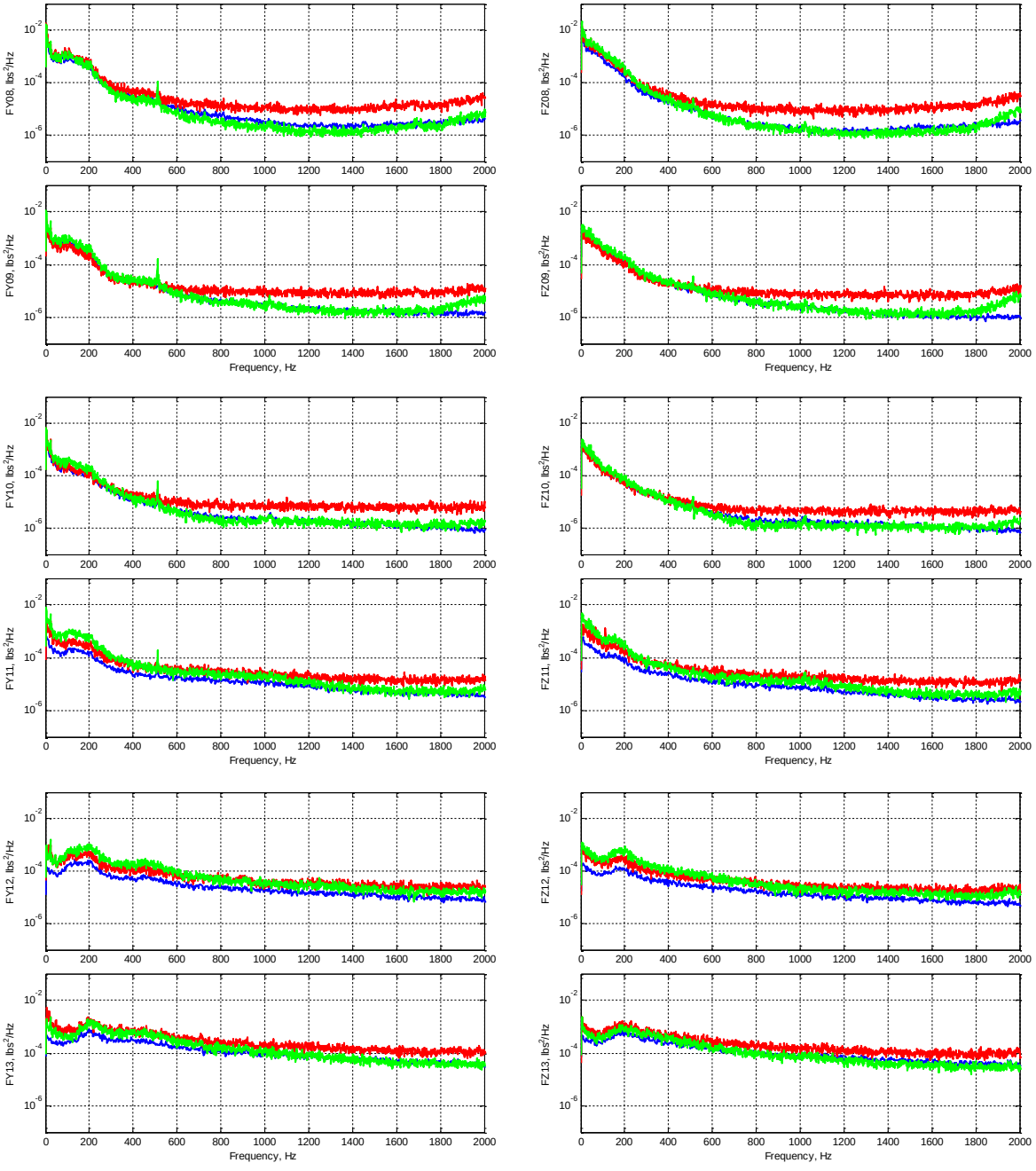

Figure 13.2.3-1—continued

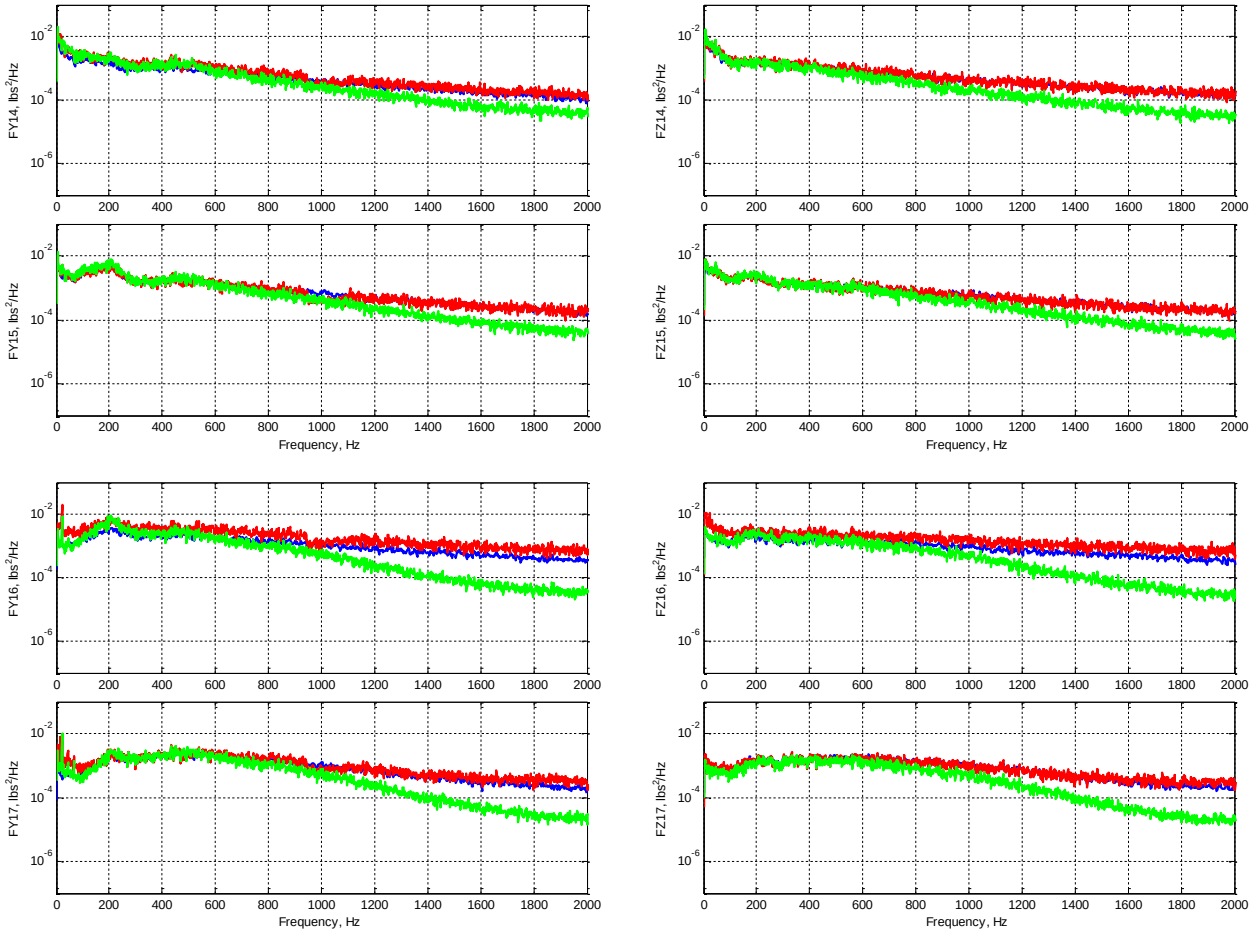

Figure 13.2.3-1—continued

13.3 Metric Section Loads

The loads on the metric section were determined by direct measurement with the 4-component balance and by integrating the uPSP pressures. The effect of filtering the balance measurements is shown in Figure 13.1-1 as spectra before and after filtering (units are N^2/Hz) for M = 0.92, $\alpha = -4°$, and Re = 3×10^6 (Run 171 point 1). The corrected balance signal and the integrated pressures from uPSP are compared in Figure 13.3-2. Some of the same features can be seen in the spectra, but the comparison indicates more work is needed to improve the balance filtering scheme accuracy.

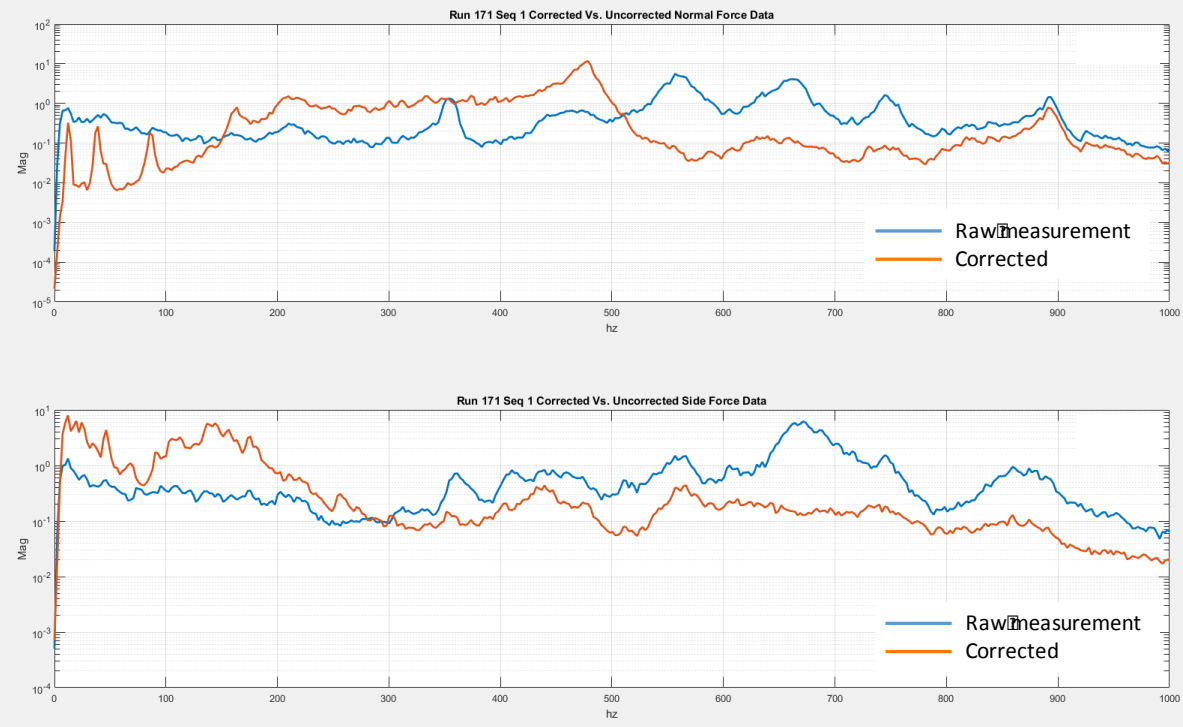

Figure 13.3-1. Comparison of Uncorrected and Corrected Balance Measurements of Unsteady Normal and Side Force—M = 0.92, α = –4°, Re = 3×10⁶

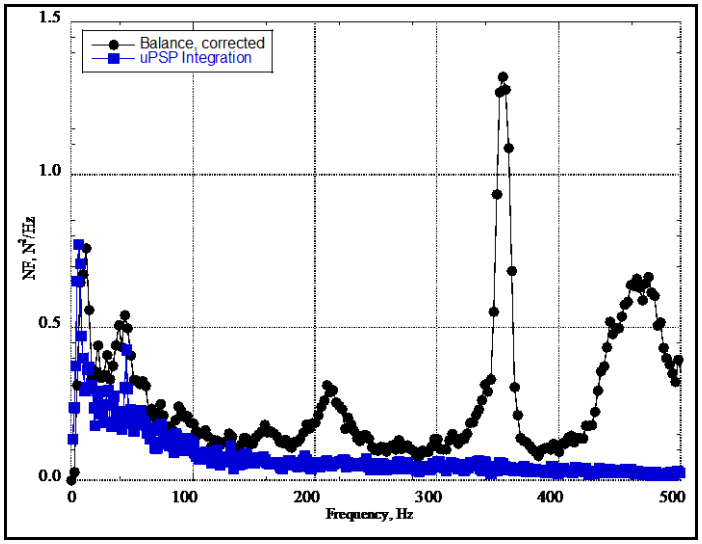

Figure 13.3-2. Comparison of Corrected Balance Measurements of Unsteady Metric Section Normal Force with Integrated uPSP Normal Force—M = 0.92, α = –4°, Re = 3×10⁶

Figure 13.3-2 shows a comparison of the filtered balance normal force power spectrum with that of the integrated uPSP over the metric section of the model. Below ~150 Hz, the agreement is very good, but the corrected balance data still have some structural dynamics that contaminates the final result. The technique shows promise, but additional work is needed to improve the filtering.

14.0 Findings, Observations, and NESC Recommendations

14.1 Findings

The following findings were identified:

F-1. uPSP has sufficient frequency response to accurately estimate launch vehicle aerodynamic buffet loads through integration of the high spatial resolution pressure measurements.

F-2. Integration of limited, sensor-based pressure measurements using coherence-length corrections generally overestimates the unsteady buffet forces for the simplified launch vehicle geometry examined.

- Expanding the frequency range over which the coherence length corrections are computed may improve the accuracy.
- The effect of more complex geometries (and associated flow fields) was not studied.

F-3. uPSP has a noise floor below which the unsteady pressure cannot be measured.

F-4. The time-accurate balance analysis technique shows promise in measuring unsteady aerodynamic forces and moments in spite of the large inertial loads present.

14.2 Observations

The following observations were made:

O-1. Several aspects of uPSP data acquisition and processing can be improved:

- The polymer-ceramic base coat surface roughness needs to be improved to expand the applicability of this technique to other aerospace vehicle testing (e.g., transonic transports).
- Kulite® or similar sensors should be used in limited numbers to ensure the accuracy of the uPSP data.
- Sensor installation methods need to be improved to reduce uPSP surface effects (e.g., thickness uniformity and transition steps).
- Unsteady pressure data density requirements as a function of configuration details need to be developed.

O-2. uPSP temperature sensitivity needs to be minimized to facilitate more efficient wind-tunnel operations (e.g., elimination of test article heat-soaking prior to data acquisition).

O-3. uPSP as a measurement technique has a wide interest in the aerospace community as witnessed by the number of company representatives who observed the test.

14.3 NESC Recommendations

The following NESC recommendations were identified and directed toward the SLS Program and the NASA Aeronautics Evaluation and Test Capabilities Project:

R-1. Continue developing uPSP materials and procedures for use in NASA wind tunnels. ***[F-1, F-4, and O-1]***

R-2. Continue evaluating the effects of the spatial density of unsteady pressure data on the integrated loads for increasingly complex launch vehicle configurations. ***[F-1]***

15.0 Alternate Viewpoint

There were no alternate viewpoints identified during the course of this assessment by the NESC team.

16.0 Other Deliverables

No unique hardware, software, or data packages, outside this contained in this report, were disseminated to other parties outside this assessment.

17.0 Lessons Learned

No applicable lessons learned were identified for entry into the NASA Lessons Learned Information System (LLIS) as a result of this assessment.

18.0 Recommendations for NASA Standards and Specifications

No recommendations for NASA standards and specifications were identified as a result of this assessment.

19.0 Definition of Terms

Finding	A relevant factual conclusion and/or issue that is within the assessment scope and that the team has rigorously based on data from their independent analyses, tests, inspections, and/or reviews of technical documentation.
Lessons Learned	Knowledge, understanding, or conclusive insight gained by experience that may benefit other current or future NASA programs and projects.

	The experience may be positive, as in a successful test or mission, or negative, as in a mishap or failure.
Observation	A noteworthy fact, issue, and/or risk, which may not be directly within the assessment scope, but could generate a separate issue or concern if not addressed. Alternatively, an observation can be a positive acknowledgement of a Center/Program/Project/Organization's operational structure, tools, and/or support provided.
Problem	The subject of the independent technical assessment.
Recommendation	A proposed measurable stakeholder action directly supported by specific Finding(s) and/or Observation(s) that will correct or mitigate an identified issue or risk.

20.0 Abbreviations

20.1 Acronym List

AEDC	Arnold Engineering Development Complex
BFF	Buffet Forcing Function
CFD	Computational Fluid Dynamics
DAS	Data Acquisition System
DFT	Discrete Fourier Transform
ESP	Electronically Scanned Pressure
fps	Frames Per Second
Hz	Hertz
IR	Infrared
LED	Light-Emitting Diode
MISO	Multiple Input–Single Output
psd	Power-Spectral Density
PSID	Pounds per Square Inch Differential
PSP	Pressure-Sensitive Paint
PT	Pressure Transducer
rms	Root Mean Square
SDS	Standard Data System
SLS	Space Launch System
uPSP	Unsteady Pressure-Sensitive Paint
UPWT	Unitary Plan Wind Tunnel
vPT	Virtual Pressure Transducer

20.2 Nomenclature

AF	Axial force, lb
NF	Normal force, lb

SF	Side force, lb
PM	Pitching moment measured at balance center, in-lb
YM	Yawing moment measured at balance center, in-lb
CA	Axial force coefficient, = AF/(q·S)
CN	Normal force coefficient, = N/F(q·S)
CY	Side force coefficient, = SF/(q·S)
CM	Pitching moment coefficient, = PM/(q·S·D)
CYM	Yawing moment coefficient, = YM/(q·S·D)
Cf	Skin friction coefficient, = τ/q
Cp	Pressure coefficient, = (p-p∞)/q
D	Reference diameter = 6.0”
f	Frequency, Hz
fps	Frames per second for image acquisition (uPSP, shadowgraph, and infrared)
M	Mach number
p	Static pressure, psf
q	Free-stream dynamic pressure, psf
Re	Reynolds Number per foot, V/ν, ft-1

21.0 References

1. Coe, C., and Nute, J., “Steady and Fluctuating Pressures at Transonic Speeds on Hammerhead Launch Vehicles,” NASA TMX-778, December 1962.
2. Liu, T, Campbell, B., Bruns, S., and Sullivan, J. P., “Temperature- and Pressure-Sensitive Luminescent Paints in Aerodynamics,” *Appl. Mech. Rev.*, 50:227–246, 1997.
3. Bell, J. H., Schairer, E. T., Hand L. A., and Mehta, R. D., “Surface Pressure Measurements Using Luminescent Coatings,” *Annu. Rev. Fluid Mech.*, 33:155–206, 2001.
4. Sellers, M. E., Nelson, M. A., and Crafton, J. W., “Dynamic Pressure-Sensitive Paint Demonstration in AEDC Propulsion Wind Tunnel 16T,” AIAA paper 2016-1146, 54th AIAA Aerospace Sciences Meeting, San Diego, CA, January 4–8, 2016.
5. UPWT/11x11 TWT Test Planning Guide.
6. Braslow, A. L. and Knox, E. C., “Simplified Method for Determination of Critical Height of Distributed Roughness Particles for Boundary-Layer Transition at Mach Numbers from 0 to 5,” NACA TN-4363, September 1958.
7. Herron, A. J., Reed, D. K., and Nance, D. K., “Reducing the Effect of Transducer Mount Induced Noise on Aeroacoustic Wind Tunnel Testing Data with a New Transducer Mount Design,” AIAA paper number 2015-3273, 21st AIAA/CEAS Aeroacoustics Conference, Dallas, TX, June 22–26, 2015.

8. "AIAA Recommended Practice for Calibration and Use of Internal Strain-Gage Balances with Application to Wind Tunnel Testing," AIAA R-091-2003, 2003.
9. Piatak, D. J., Sekula, M. K., and Rausch, R. D., "Ares Launch Vehicle Transonic Buffet Testing and Analysis Techniques," *Journal of Spacecraft and Rockets*, Vol. 49, No. 5, 798–807, September–October 2012.
10. Sekula, M. K., Piatak, D. J., and Rausch, R. D., "Effect of Surface Pressure Integration Methodology on Launch Vehicle Buffet Forcing Functions," AIAA paper 2016-0545, 54th AIAA Aerospace Sciences Meeting, San Diego, CA, January 4–8, 2016.
11. Panda, J., Roozeboom, N. H., and Ross, J. C., "Wavenumber-Frequency Spectra of Pressure Fluctuations Measured via Fast-Response Pressure-Sensitive Paint," AIAA paper 2016-3007, 22nd AIAA/CEAS Aeroacoustics Conference, Lyon, France, May 30–June 1, 2016.
12. Roozeboom, N., et al., "Unsteady PSP Measurements on a Flat Plate Subject to Vortex Shedding from a Rectangular Prism," AIAA paper 2016-2017, 54th AIAA Aerospace Sciences Meeting, San Diego, CA, January 4–8, 2016.
13. Hanly, R. D., "Effects of Transducer Flushness on Fluctuating Surface Pressure Measurements," AIAA paper 75-534, 2nd AIAA Aero-Acoustics Conference, Hampton, VA, March 24–26, 1975.
14. Van den Bosch, P.P.J., *Modeling, Identification, and Simulation of Dynamical Systems*, CRC Press, Inc., 1994.
15. Coe, C. F. and Kaskey, A. J., "The Effects of Nose Bluntness on the Pressure Fluctuations Measured on 15° and 20° Cone-Cylinders at Transonic Speeds," NASA TM X-779, January 1963.

22.0 Appendices

A. Model Drawings
B. Locations of Static Pressure Taps
C. Locations of Unsteady Pressure Transducers
D. Model Design Loads
E. Test Matrix
F. Data File/Folder Structure

Appendix A. Model Drawings

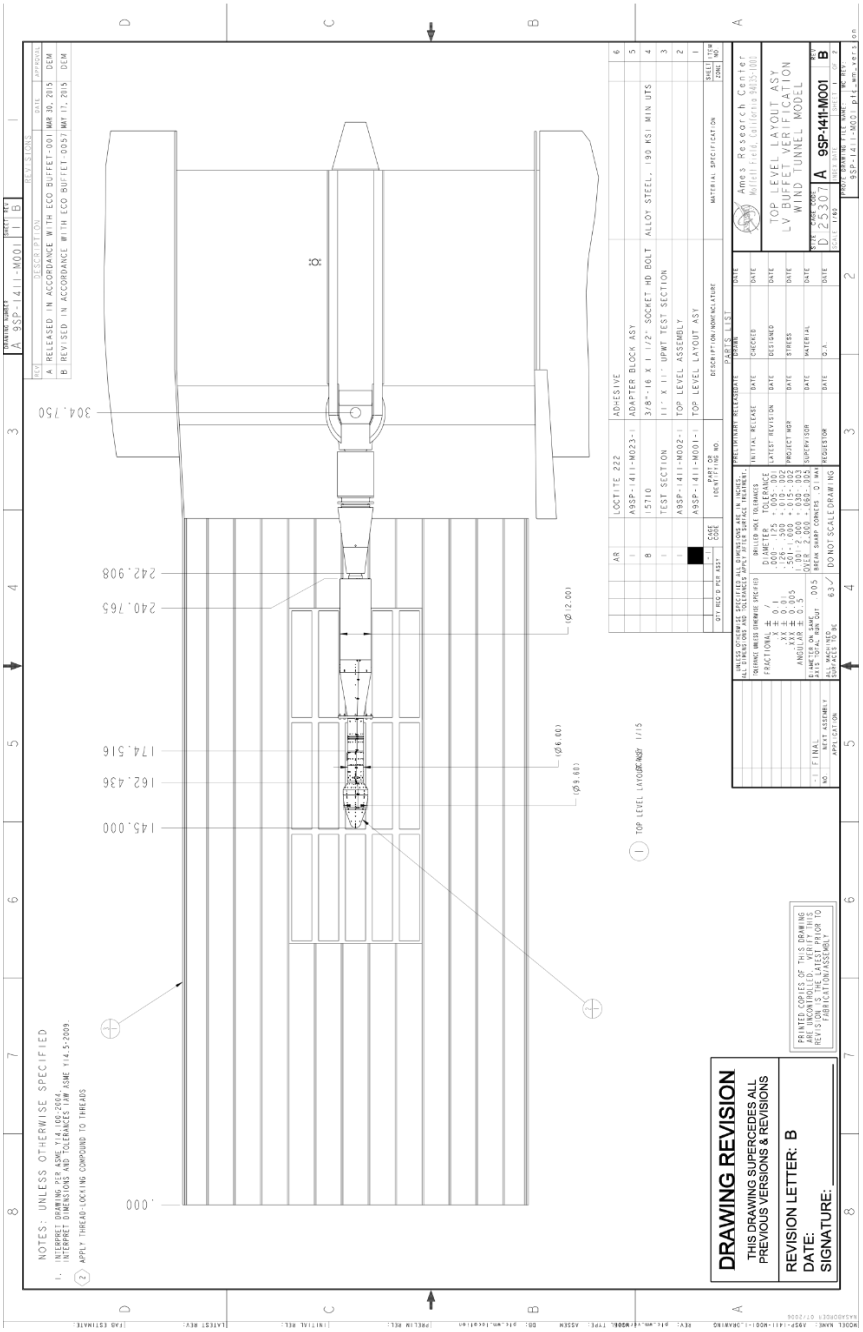

Figure A-1. Side View of Model in 11- by 11-Foot Transonic Wind Tunnel

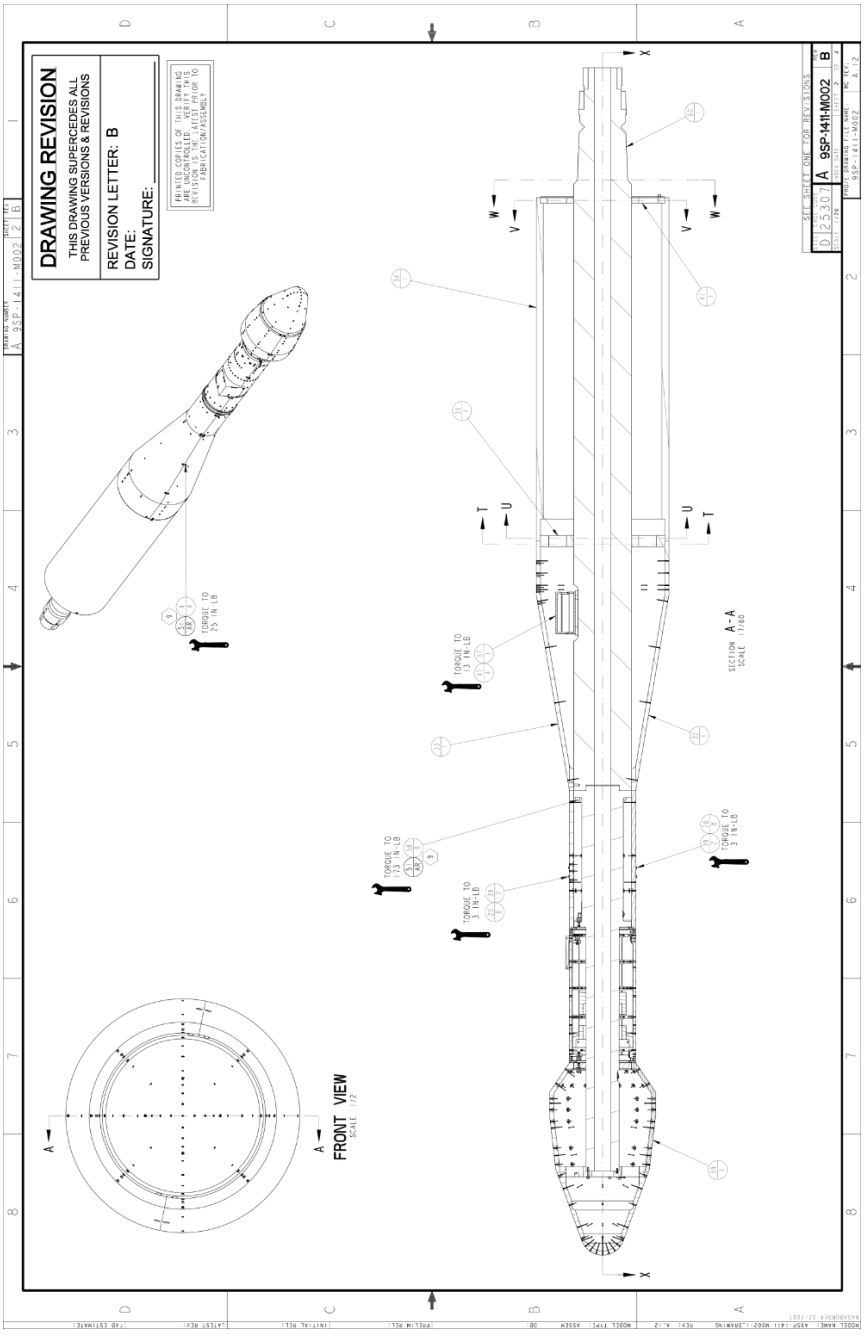

Figure A-2. Overview of Model Structure

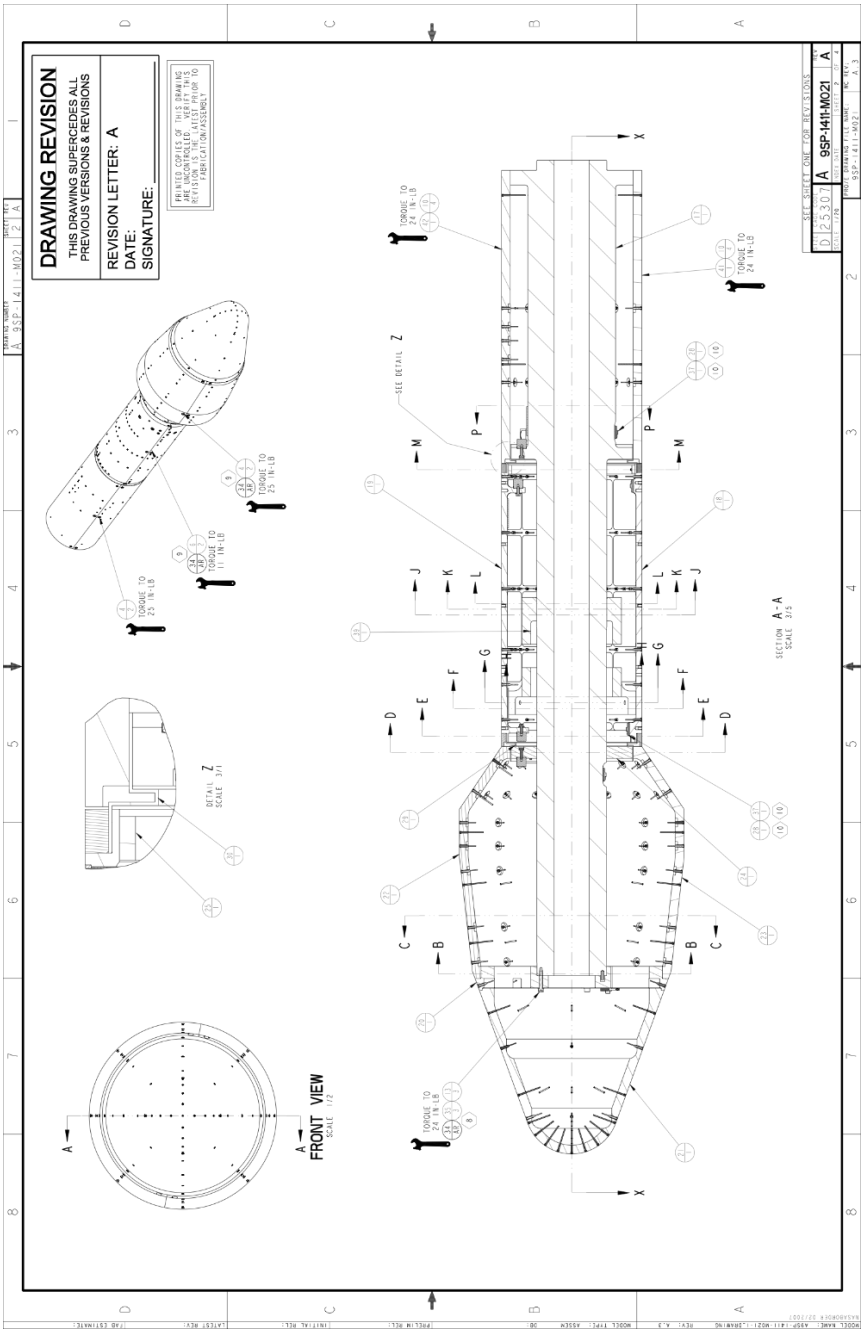

Figure A-3. Instrumentation Layout in Payload, Metric Section, and Second Stage

Appendix B. Locations of Static Pressure Taps

Table B-1. Locations of Static Pressure Taps (entries in grey denote plugged taps)

Tap #	Measured		
	X-dim	Y-dim	Z-dim
CP01-01	0.000	0.000	0.000
CP02-01	0.093	0.000	0.603
CP02-02		-0.603	0.000
CP02-03		-0.000	-0.603
CP02-04		0.603	-0.000
CP03-01	0.362	0.000	1.148
CP03-02		-1.148	0.000
CP03-03		-0.000	-1.148
CP03-04		1.148	-0.000
CP04-01	0.782	0.000	1.586
CP04-02		-1.586	0.000
CP04-03		0.006	-1.586
CP04-04		1.586	-0.000
CP05-01	1.316	0.000	1.879
CP05-02		-1.879	0.000
CP05-03		-0.000	-1.879
CP05-04		1.879	-0.000
CP06-01	2.500	0.000	2.310
CP06-02	2.500	-1.633	1.633
CP06-03	2.501	-2.310	0.011
CP06-04	2.503	-1.627	-1.641
CP06-05	2.507	0.005	-2.313
CP06-06	2.500	1.633	-1.633
CP06-07	2.500	2.310	-0.000
CP06-08	2.500	1.633	1.633
CP07-01	6.000	0.000	3.584
CP07-02		-2.534	2.534
CP07-03		-3.584	0.000
CP07-04		-2.534	-2.534
CP07-05		-0.000	-3.584
CP07-06		2.534	-2.534
CP07-07		3.584	-0.000
CP07-08		2.534	2.534

Table B.1—Continued

Tap #	Measured		
	X-dim	Y-dim	Z-dim
CP08-01	9.000	0.000	4.380
CP08-02		-3.097	3.097
CP08-03		-4.380	0.000
CP08-04		-3.097	-3.097
CP08-05		-0.000	-4.380
CP08-06		3.097	-3.097
CP08-07		4.380	-0.000
CP08-08		3.097	3.097
CP09-01	11.500	0.000	4.665
CP09-02		-3.299	3.299
CP09-03		-4.665	0.000
CP09-04		-3.299	-3.299
CP09-05		-0.000	-4.665
CP09-06		3.299	-3.299
CP09-07		4.665	-0.000
CP09-08		3.299	3.299
CP10-01	13.750	0.000	4.800
CP10-02		-4.800	0.000
CP10-03		-0.000	-4.800
CP10-04		4.800	-0.000
CP11-01	15.500	-4.209	4.292
CP11-02		-0.837	-4.209
CP11-03		4.209	-0.837
CP11-04		0.837	4.209
CP12-01	16.750	-3.383	3.449
CP12-02		-0.673	-3.383
CP12-03		3.383	-0.673
CP12-04		0.673	3.383
CP13-01	33.762	0.005	3.000
CP13-02	33.764	-3.000	0.007
CP13-03	33.762	-0.009	-3.000
CP13-04	33.763	3.000	-0.012
CP14-01	36.162	-2.769	1.153
CP14-02	36.163	-1.157	-2.768
CP14-03	36.163	2.766	-1.160
CP14-04	36.161	1.153	2.769

Table B-1—Continued

Tap #	Measured		
	X-dim	Y-dim	Z-dim
CP01-01	0.000	0.000	0.000
CP02-01	0.093	0.000	0.603
CP02-02		-0.603	0.000
CP02-03		-0.000	-0.603
CP02-04		0.603	-0.000
CP03-01	0.362	0.000	1.148
CP03-02		-1.148	0.000
CP03-03		-0.000	-1.148
CP03-04		1.148	-0.000
CP04-01	0.782	0.000	1.586
CP04-02		-1.586	0.000
CP04-03		0.006	-1.586
CP04-04		1.586	-0.000
CP05-01	1.316	0.000	1.879
CP05-02		-1.879	0.000
CP05-03		-0.000	-1.879
CP05-04		1.879	-0.000
CP06-01	2.500	0.000	2.310
CP06-02	2.500	-1.633	1.633
CP06-03	2.501	-2.310	0.011
CP06-04	2.503	-1.627	-1.641
CP06-05	2.507	0.005	-2.313
CP06-06	2.500	1.633	-1.633
CP06-07	2.500	2.310	-0.000
CP06-08	2.500	1.633	1.633
CP07-01	6.000	0.000	3.584
CP07-02		-2.534	2.534
CP07-03		-3.584	0.000
CP07-04		-2.534	-2.534
CP07-05		-0.000	-3.584
CP07-06		2.534	-2.534
CP07-07		3.584	-0.000
CP07-08		2.534	2.534

Table B-1—Continued

Tap #	Measured		
	X-dim	Y-dim	Z-dim
CP08-01	9.000	0.000	4.380
CP08-02		-3.097	3.097
CP08-03		-4.380	0.000
CP08-04		-3.097	-3.097
CP08-05		-0.000	-4.380
CP08-06		3.097	-3.097
CP08-07		4.380	-0.000
CP08-08		3.097	3.097
CP09-01	11.500	0.000	4.665
CP09-02		-3.299	3.299
CP09-03		-4.665	0.000
CP09-04		-3.299	-3.299
CP09-05		-0.000	-4.665
CP09-06		3.299	-3.299
CP09-07		4.665	-0.000
CP09-08		3.299	3.299
CP10-01	13.750	0.000	4.800
CP10-02		-4.800	0.000
CP10-03		-0.000	-4.800
CP10-04		4.800	-0.000
CP11-01	15.500	-4.209	4.292
CP11-02		-0.837	-4.209
CP11-03		4.209	-0.837
CP11-04		0.837	4.209
CP12-01	16.750	-3.383	3.449
CP12-02		-0.673	-3.383
CP12-03		3.383	-0.673
CP12-04		0.673	3.383
CP13-01	33.762	0.005	3.000
CP13-02	33.764	-3.000	0.007
CP13-03	33.762	-0.009	-3.000
CP13-04	33.763	3.000	-0.012
CP14-01	36.162	-2.769	1.153
CP14-02	36.163	-1.157	-2.768
CP14-03	36.163	2.766	-1.160
CP14-04	36.161	1.153	2.769

Appendix C. Locations of Unsteady Pressure Transducers

Table C-1. Locations of Kulite® Transducers (grey indicates broken sensor)

Kulite® #	Measured			
	Angle	X-dim	Y-dim	Z-dim
K01-01	0.000	1.500	0.000	1.945
K01-02	90.000	1.500	-1.945	0.000
K01-03	180.000	1.500	0.000	-1.945
K01-04	270.000	1.500	1.945	0.000
K02-01	0.000	4.500	0.000	3.038
K02-02	90.000	4.500	-3.038	0.000
K02-03	180.000	4.500	0.000	-3.038
K02-04	270.000	4.500	3.038	0.000
K03-01	0.000	7.170	0.000	4.010
K03-02	45.000	7.170	-2.835	2.835
K03-03	90.000	7.170	4.010	0.000
K03-04	135.000	7.170	-2.835	-2.835
K03-05	180.000	7.170	0.000	-4.010
K03-06	225.000	7.170	2.835	-2.835
K03-07	270.000	7.170	-4.010	0.000
K03-08	315.000	7.170	2.835	2.835
K04-01	0.000	8.170	0.000	4.285
K04-02	45.000	8.170	-3.030	3.030
K04-03	90.000	8.170	-4.285	0.000
K04-04	135.000	8.170	-3.030	-3.030
K04-05	180.000	8.170	0.000	-4.285
K04-06	225.000	8.170	3.030	-3.030
K04-07	270.000	8.170	4.285	0.000
K04-08	315.000	8.170	3.030	3.030
K05-01	0.000	9.670	0.000	4.456
K05-02	45.000	9.670	-3.151	3.151
K05-03	90.000	9.670	-4.456	0.000
K05-04	135.000	9.670	-3.151	-3.151
K05-05	180.000	9.670	0.000	-4.456
K05-06	225.000	9.670	3.151	-3.151
K05-07	270.000	9.670	4.456	0.000
K05-08	315.000	9.670	3.151	3.151

Table C-1—Continued

Kulite® #	Measured			
	Angle	X-dim	Y-dim	Z-dim
K06-01	0.000	12.070	0.000	4.729
K06-02	45.000	12.070	-3.344	3.344
K06-03	90.000	12.070	-4.729	0.000
K06-04	135.000	12.070	-3.344	-3.344
K06-05	180.000	12.070	0.000	-4.729
K06-06	225.000	12.070	3.344	-3.344
K06-07	270.000	12.070	4.729	0.000
K06-08	315.000	12.070	3.344	3.344
K07-01	0.000	13.170	0.000	4.800
K07-02	45.000	13.170	-3.394	3.394
K07-03	90.000	13.170	-4.800	0.000
K07-04	135.000	13.170	-3.394	-3.394
K07-05	180.000	13.170	0.000	-4.800
K07-06	225.000	13.170	3.394	-3.394
K07-07	270.000	13.170	4.800	0.000
K07-08	315.000	13.170	3.394	3.394
K08-01	0.000	14.170	0.000	4.800
K08-02	45.000	14.170	-3.394	3.394
K08-03	90.000	14.170	-4.800	0.000
K08-04	135.000	14.170	-3.394	-3.394
K08-05	180.000	14.170	0.000	-4.800
K08-06	225.000	14.170	3.394	-3.394
K08-07	270.000	14.170	4.800	0.000
K08-08	315.000	14.170	3.394	3.394

Table C-1—Continued

Kulite® #	Measured			
	Angle	X-dim	Y-dim	Z-dim
K09-01	0.000	15.570	0.000	4.244
K09-02	22.500	15.570	-1.624	3.921
K09-03	45.000	15.570	-3.001	3.001
K09-04	67.500	15.570	-3.921	1.624
K09-05	90.000	15.570	-4.244	0.000
K09-06	112.500	15.570	-3.921	-1.624
K09-07	135.000	15.570	-3.001	-3.001
K09-08	157.500	15.570	-1.624	-3.921
K09-09	180.000	15.570	-0.000	-4.244
K09-10	202.500	15.570	1.624	-3.921
K09-11	225.000	15.570	3.001	-3.001
K09-12	247.500	15.570	3.921	-1.624
K09-13	270.000	15.570	4.244	-0.000
K09-14	292.500	15.570	3.921	1.624
K09-15	315.000	15.570	3.001	3.001
K09-16	337.500	15.567	1.624	3.921
K10-01	0.000	16.870	0.000	3.368
K10-02	22.500	16.870	-1.289	3.111
K10-03	45.000	16.870	-2.381	2.381
K10-04	67.500	16.870	-3.111	1.289
K10-05	90.000	16.870	-3.368	0.000
K10-06	112.500	16.870	-3.111	-1.289
K10-07	135.000	16.870	-2.381	-2.381
K10-08	157.500	16.870	-1.289	-3.111
K10-09	180.000	16.870	-0.000	-3.368
K10-10	202.500	16.870	1.289	-3.111
K10-11	225.000	16.870	2.381	-2.381
K10-12	247.500	16.870	3.111	-1.289
K10-13	270.000	16.870	3.368	-0.000
K10-14	292.500	16.870	3.111	1.289
K10-15	315.000	16.870	2.381	2.381
K10-16	337.500	16.870	1.289	3.111

Table C-1—Continued

Kulite® #	Measured			
	Angle	X-dim	Y-dim	Z-dim
K11-01	0.000	18.559	0.000	3.000
K11-02	45.000	18.559	-2.121	2.121
K11-03	90.000	18.559	-3.000	0.000
K11-04	135.000	18.559	-2.121	-2.121
K11-05	180.000	18.559	-0.000	-3.000
K11-06	225.000	18.559	2.121	-2.121
K11-07	270.000	18.559	3.000	-0.000
K11-08	315.000	18.559	2.121	2.121
K12-01	0.000	20.059	0.000	3.000
K12-02	45.000	20.059	-2.121	2.121
K12-03	90.000	20.059	-3.000	0.000
K12-04	135.000	20.059	-2.121	-2.121
K12-05	180.000	20.059	-0.000	-3.000
K12-06	225.000	20.059	2.121	-2.121
K12-07	270.000	20.059	3.000	-0.000
K12-08	315.000	20.059	2.121	2.121
K13-01	0.000	21.570	0.000	3.000
K13-02	9.000	21.570	-0.469	2.963
K13-03	18.000	21.570	-0.927	2.853
K13-04	27.000	21.570	-1.362	2.673
K13-05	36.000	21.570	-1.763	2.427
K13-06	45.000	21.570	-2.121	2.121
K13-07	90.000	21.570	-3.000	0.000
K13-08	135.000	21.570	-2.121	-2.121
K13-09	180.000	21.570	-0.000	-3.000
K13-10	225.000	21.570	2.121	-2.121
K13-11	270.000	21.570	3.000	-0.000
K13-12	315.000	21.570	2.121	2.121
K13-13	324.000	21.570	1.763	2.427
K13-14	333.000	21.570	1.362	2.673
K13-15	342.000	21.570	0.927	2.853
K13-16	351.000	21.570	0.469	2.963

Table C-1—Continued

Kulite® #	Measured			
	Angle	X-dim	Y-dim	Z-dim
K15-01	0.000	26.559	0.000	3.000
K15-02	22.500	26.559	-1.148	2.772
K15-03	45.000	26.559	-2.121	2.121
K15-04	67.500	26.559	-2.772	1.148
K15-05	90.000	26.559	-3.000	0.000
K15-06	112.500	26.559	-2.772	-1.148
K15-07	135.000	26.559	-2.121	-2.121
K15-08	157.500	26.559	-1.148	-2.772
K15-09	180.000	26.559	-0.000	-3.000
K15-10	202.500	26.559	1.148	-2.772
K15-11	225.000	26.559	2.121	-2.121
K15-12	247.500	26.559	2.772	-1.148
K15-13	270.000	26.559	3.000	-0.000
K15-14	292.500	26.559	2.772	1.148
K15-15	315.000	26.559	2.121	2.121
K15-16	337.500	26.559	1.148	2.772
K16-01	0.000	28.959	0.000	3.000
K16-02	9.000	28.959	-0.469	2.963
K16-03	18.000	28.959	-0.927	2.853
K16-04	27.000	28.959	-1.362	2.673
K16-05	36.000	28.959	-1.763	2.427
K16-06	45.000	28.959	-2.121	2.121
K16-07	90.000	28.959	-3.000	0.012
K16-08	135.000	28.959	2.129	2.113
K16-09	180.000	28.959	-0.007	-3.000
K16-10	225.000	28.959	2.121	-2.121
K16-11	270.000	28.959	3.000	-0.000
K16-12	315.000	28.959	2.121	2.121
K16-13	324.000	28.959	1.763	2.427
K16-14	333.000	28.959	1.362	2.673
K16-15	342.000	28.959	0.927	2.853
K16-16	351.000	28.959	0.469	2.963

Table C-1—Continued

Kulite® #	Measured			
	Angle	X-dim	Y-dim	Z-dim
K17-01	0.000	32.992	0.006	3.000
K17-02	22.500	32.992	-1.145	2.773
K17-03	45.000	32.992	-2.116	2.127
K17-04	67.500	32.992	-2.769	1.153
K17-05	90.000	32.992	-3.000	0.005
K17-06	112.500	32.992	-2.775	-1.140
K17-07	135.000	32.992	-2.125	-2.117
K17-08	157.500	32.992	-1.154	-2.769
K17-09	180.000	32.992	-0.008	-3.000
K17-10	202.500	32.992	1.138	-2.776
K17-11	225.000	32.992	2.113	-2.130
K17-12	247.500	32.992	2.767	1.160
K17-13	270.000	32.992	3.000	-0.012
K17-14	292.500	32.992	2.773	1.144
K17-15	315.000	32.992	2.124	2.118
K17-16	337.500	32.992	1.151	2.771
K18-01	0.000	36.170	0.006	3.000
K18-02	45.000	36.170	-2.117	2.215
K18-03	90.000	36.170	-3.000	0.008
K18-04	135.000	36.170	-2.126	-2.116
K18-05	180.000	36.170	-0.010	-3.000
K18-06	225.000	36.170	2.112	-2.130
K18-07	270.000	36.170	3.000	-0.014
K18-08	315.000	36.170	2.125	2.117
K19-01	0.000	58.970	0.000	5.865
K20-01	0.000	60.070	0.000	6.000
K21-01	0.000	60.470	0.000	6.000
K22-01	0.000	61.570	0.000	6.000
K23-01	0.000	62.670	0.000	6.000
KF01	45.000	33.980	-2.121	2.121
KF02	45.000	34.773	-2.116	2.126
KF03	45.000	35.380	-2.116	2.126

Appendix D. Model Design Loads

Table D-1. Maximum Overall Model Loads (Highest Re at Each Mach Number)— Reference Area = 72.4 square inches; Reference Length = 9.6 inches; Moment Reference Point, x = 0 inches (Model Nose)

M	AOA	q, psf	C_A	C_S	C_N	AF	NF	PM
0.8	0	1450	0.631	-0.0004	0	460	0	9
0.8	2	1450	0.6375	0.0004	0.1373	465	100	-4134
0.8	4	1450	0.6564	0.0034	0.2749	478	200	-8193
0.85	0	1500	0.6685	0	0	504	0	0
0.85	2	1500	0.6629	-0.003	0.1372	500	103	-4298
0.85	4	1500	0.6875	0.0008	0.2769	518	209	-8357
0.9	0	1550	0.7147	0	0	557	0	0
0.9	2	1550	0.7103	0.0029	0.1445	553	113	-3875
0.9	4	1550	0.7323	0.0182	0.3137	571	244	-8630
0.95	0	1600	0.8478	-0.0005	-0.0003	682	0	12
0.95	2	1600	0.8588	0	0.1521	691	122	-4788
0.95	4	1600	0.8867	0	0.3265	713	263	-9776
1.05	0	1700	1.3259	0	0	1133	0	0
1.05	2	1700	1.3181	0.0006	0.1583	1126	135	-5564
1.05	4	1700	1.3614	-0.0003	0.3261	1163	279	-10905
1.1	0	1750	1.3153	-0.0001	0	1157	0	1
1.1	2	1750	1.3111	-0.0003	0.1531	1153	135	-5244
1.1	4	1750	1.3479	-0.0012	0.3149	1186	277	-10315
1.2	0	1800	1.3684	0	-0.0004	1238	0	34
1.2	2	1800	1.3599	0.0005	0.155	1230	140	-5368
1.2	4	1800	1.3864	-0.0015	0.3105	1254	281	-10417

Appendix E. Test Matrix

Table E-1. Test Matrix

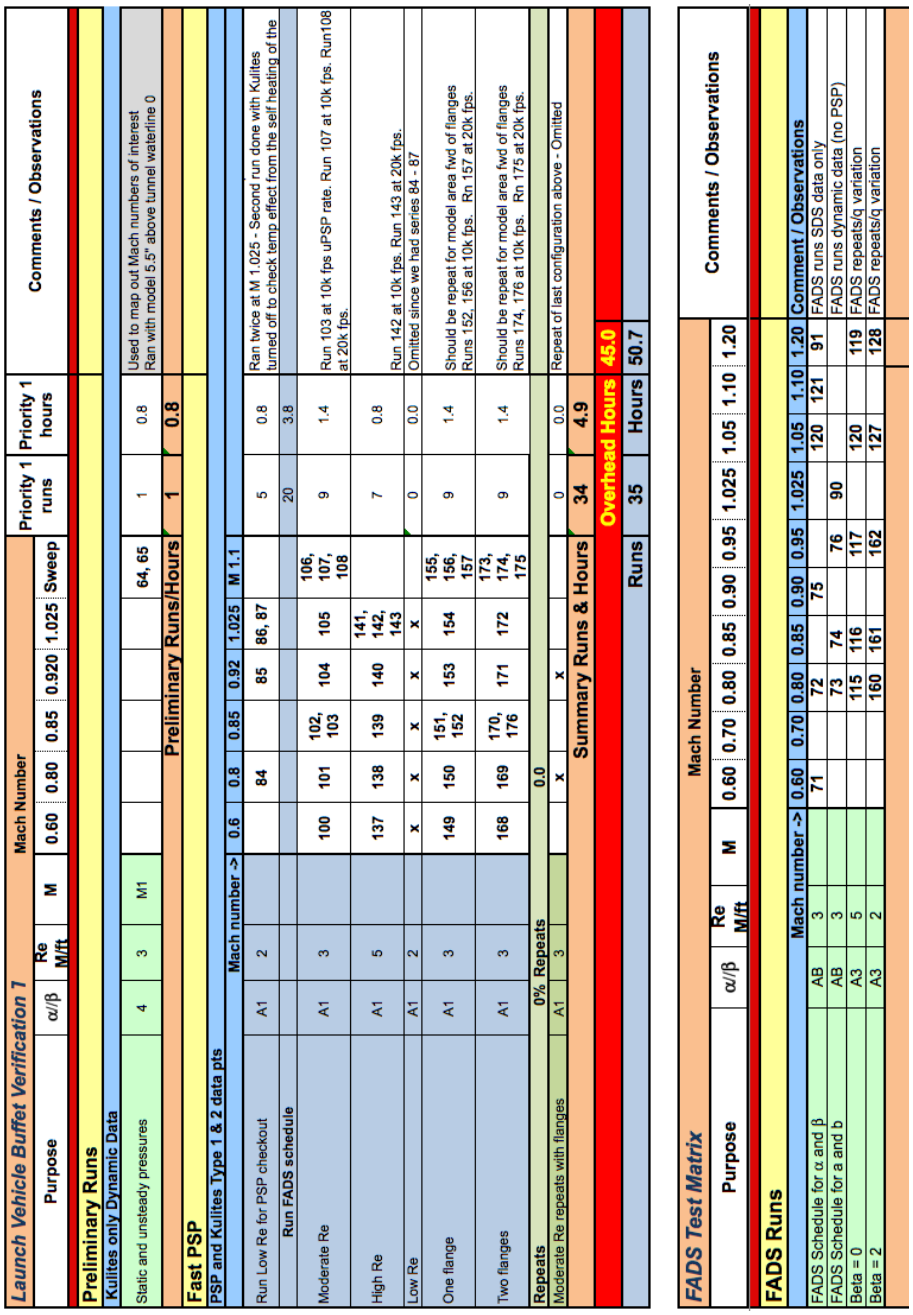

Launch Vehicle Buffet Verification 7				Mach Number							Priority 1 runs	Priority 1 hours	Comments / Observations
Purpose	α/β	Re M/ft	M	0.60	0.80	0.85	0.920	1.025	Sweep				
Preliminary Runs													
Kulites only Dynamic Data													
Static and unsteady pressures	4	3	M1						64, 65		1	0.8	Used to map out Mach numbers of interest Ran with model 5.5" above tunnel waterline 0
Preliminary Runs/Hours											**1**	**0.8**	
Fast PSP													
PSP and Kulites Type 1 & 2 data pts													
Mach number ->				**0.6**	**0.8**	**0.85**	**0.92**	**1.025**	**M 1.1**				
Run Low Re for PSP checkout	A1	2			84		85	86, 87			5	0.8	Ran twice at M 1.025 - Second run done with Kulites turned off to check temp effect from the self heating of the
Run FADS schedule											20	3.8	
Moderate Re	A1	3		100	101	102, 103	104	105	106, 107, 108		9	1.4	Run 103 at 10k fps uPSP rate. Run 107 at 10k fps. Run108 at 20k fps.
High Re	A1	5		137	138	139	140	141, 142, 143			7	0.8	Run 142 at 10k fps. Run 143 at 20k fps.
Low Re	A1	2		x	x	x	x	x			0	0.0	Omitted since we had series 84 - 87
One flange	A1	3		149	150	151, 152	153	154	155, 156, 157		9	1.4	Should be repeat for model area fwd of flanges Runs 152, 156 at 10k fps. Rn 157 at 20k fps.
Two flanges	A1	3		168	169	170, 176	171	172	173, 174, 175		9	1.4	Should be repeat for model area fwd of flanges Runs 174, 176 at 10k fps. Rn 175 at 20k fps.
Repeats				**0.0**									
0% Repeats					x		x				0	0.0	Repeat of last configuration above - Omitted
Moderate Re repeats with flanges	A1	3											
Summary Runs & Hours											**34**	**4.9**	
Overhead Hours												**45.0**	
Runs											**35**	**Hours**	**50.7**

FADS Test Matrix				Mach Number										Comments / Observations
Purpose	α/β	Re M/ft	M	0.60	0.70	0.80	0.85	0.90	0.95	1.025	1.05	1.10	1.20	
FADS Runs														
Mach number ->				**0.60**	**0.70**	**0.80**	**0.85**	**0.90**	**0.95**	**1.025**	**1.05**	**1.10**	**1.20**	**Comment / Observations**
FADS Schedule for α and β	AB	3		71		72		75		120	121	91		FADS runs SDS data only
FADS Schedule for a and b	AB	3				73	74		76	90				FADS runs dynamic data (no PSP)
Beta = 0	A3	5				115	116		117		120		119	FADS repeats/q variation
Beta = 2	A3	2				160	161		162		127		128	FADS repeats/q variation

Appendix F. Data File/Folder Structure

The data should be stored point by point. Each data system shall store the data from each data point in a folder whose file name includes run and point number, an identifier for the type of data, and the configuration code.

Data Files

1. SDS Files - file name (0294 is the Test Number, xxx is the Run number, yyy is the point or sequence number): **11-0294Rxxx.txt –** Content of the files is as follows:

TEST	RUN	POINT	CONFIGNO	ACQYEAR	ACQMONTH	ACQDAY
ACQHOUR	ACQMIN	ACQSEC	CMPYEAR	CMPMONTH	CMPDAY	CMPHOUR
CMPMIN	CMPSEC	DATAREV	LREF	BREF	SREF	XMRC
YMRC	ZMRC	XBMC	YBMC	ZBMC	XTRAN	YTRAN
ZTRAN	NFBAL	PMBAL	SFBAL	YMBAL	CNB	CPMB
CYB	CYMB	GAMMA	RGAS	PTINF	PINF	TTINF
TINF	MACH	RHOINF	VINF	QINF	SPHUMIDITY	
DEWPOINT	REFT	RED	THETAQ1	BETA	ALPHA	P001
P002	P003	P004	P005	P006	P007	P008
P009	P010	P011	P012	P013	P014	P015
P016	P017	P018	P019	P020	P021	P022
P023	P024	P025	P026	P027	P028	P029
P030	P031	P032	P033	P034	P035	P036
P037	P038	P039	P040	P041	P042	P043
P044	P045	P046	P047	P048	P049	P050
P051	P052	P053	P054	P055	P056	P057
P058	P059	P060	P061	P062	P063	P064
P065	P066	P067	P068	P069	P070	P071
P072	P073	P074	P075	P076	P077	P078
P079	P080	P081	P082	P083	P084	P085
P086	P087	P088	P089	P090	P091	P092
P093	P094	P095	P096	P097	P098	P099
P100	P101	P102	P103	P104	P105	P106
P107	P108	P109	P110	P111	P112	P113
P114	P115	P116	P117	P118	P119	P120
P121	CP01-01	CP02-01	CP02-02	CP02-03	CP02-04	CP03-01
CP03-02	CP03-03	CP03-04	CP04-01	CP04-02	CP04-03	CP04-04
CP05-01	CP05-02	CP05-03	CP05-04	CP06-01	CP06-02	CP06-03
CP06-04	CP06-05	CP06-06	CP06-07	CP06-08	CP07-01	CP07-02
CP07-03	CP07-04	CP07-05	CP07-06	CP07-07	CP07-08	CP08-01
CP08-02	CP08-03	CP08-04	CP08-05	CP08-06	CP08-07	CP08-08
CP09-01	CP09-02	CP09-03	CP09-04	CP09-05	CP09-06	CP09-07
CP09-08	CP10-01	CP10-02	CP10-03	CP10-04	CP11-01	CP11-02
CP11-03	CP11-04	CP12-01	CP12-02	CP12-03	CP12-04	CP13-01
CP13-02	CP13-03	CP13-04	CP14-01	CP14-02	CP14-03	CP14-04
CP15-01	CP15-02	CP15-03	CP15-04	CP15-05	CP15-06	CP15-07
CP15-08	CP16-01	CP16-02	CP16-03	CP16-04	CP16-05	CP16-06

CP16-07	CP16-08	CP17-01	CP17-02	CP17-03	CP17-04	CP18-01
CP18-02	CP18-03	CP18-04	CP19-01	CP19-02	CP19-03	CP19-04
CP20-01	CP20-02	CP20-03	CP20-04	CP20-05	CP20-06	CP20-07
CP20-08	CP21-01	CP21-02	CP21-03	CP21-04	CP21-05	CP21-06
CP21-07	CP21-08	CP22-01	CP22-02	CP22-03	CP22-04	CP23-01
CP23-02	CP23-03	CP23-04				

2. Pressure Sensitive Paint
   - 2.1. Grid files
     - 2.1.1. Configuration 1 – Model_11.grid
     - 2.1.2. Configuration 2 – Model_11_1f.grid (1 flange)
     - 2.1.3. Configuration 3 – Model_11_2f.grid (2 flanges)
   - 2.2. Pressure files containing pressure time histories at above grid points
     - 2.2.1. 0xxxyy.time (xxx is Run Number, yy is point or sequence number)
3. Kulite® data—folder names: xxx (xxx is Run Number)
   - 3.1. Sub folders:
     - 3.1.1. cond - Matlab files containing the test conditions by point/sequence numbers; e.g. R0083_S0001.pbp (Run 83, sequence 1)
     - 3.1.2. Proc - Processed Matlab files by point or sequence number; e.g., t11-0294T83p1proc.mat (Run 83, sequence 1)
     - 3.1.3. raw - time history and run information files
       - 3.1.3.1. t11-0294T89p1t1.fast - high-rate data at 102 kHz
       - 3.1.3.2. t11-0294T89p1t1.slow - slow rate data at 10 kHz
       - 3.1.3.3. t11-0294T89p1t1.info - test conditions and sampling information
     - 3.1.4. TimePlot - Sample time-history plots of 20 sensors
       - 3.1.4.1. Time_RXX_SY_DAQZ_low_P.png - image of time histories at 10 kHz of selected sensors from Run XX, point/sequence Y, front-end system Z (numbered 1, 2, and 3)
       - 3.1.4.2. Time_RXX_SY_DAQZ_high_PW.png - image of time histories at 10 kHz of selected sensors from Run XX, point/sequence Y, front-end system Z (numbered 1, 2, and 3), W is a page number for the plots (1 through 3)

REPORT DOCUMENTATION PAGE

Form Approved
OMB No. 0704-0188

1. REPORT DATE *(DD-MM-YYYY)*	2. REPORT TYPE	3. DATES COVERED *(From - To)*
01- 11 - 2016	Technical Memorandum	August 2014 - July 2016

4. TITLE AND SUBTITLE

Investigation of Unsteady Pressure-Sensitive Paint (uPSP) and a Dynamic Loads Balance to Predict Launch Vehicle Buffet Environments

5a. CONTRACT NUMBER

5b. GRANT NUMBER

5c. PROGRAM ELEMENT NUMBER

6. AUTHOR(S)

Schuster, David M..; Panda, Jayanta; Ross, James C.;
Roozeboom, Nettie H.; Burnside, Nathan J.; Ngo, Christina L.;
Kumagai, Hiro; Sellers, Marvin; Powell, Jessica M.; Sekula, Martin K.;
Piatak, David J.

5d. PROJECT NUMBER

5e. TASK NUMBER

5f. WORK UNIT NUMBER

869021.05.07.09.60

7. PERFORMING ORGANIZATION NAME(S) AND ADDRESS(ES)

NASA Langley Research Center
Hampton, VA 23681-2199

8. PERFORMING ORGANIZATION REPORT NUMBER

L-20771 NESC-RP-14-00962

9. SPONSORING/MONITORING AGENCY NAME(S) AND ADDRESS(ES)

National Aeronautics and Space Administration
Washington, DC 20546-0001

10. SPONSOR/MONITOR'S ACRONYM(S)

NASA

11. SPONSOR/MONITOR'S REPORT NUMBER(S)

NASA/TM-2016-219352

12. DISTRIBUTION/AVAILABILITY STATEMENT

Unclassified - Unlimited
Subject Category 16 Space Transportation and Safety
Availability: NASA STI Program (757) 864-9658

13. SUPPLEMENTARY NOTES

14. ABSTRACT

This NASA Engineering and Safety Center (NESC) assessment investigated innovative test techniques for acquiring launch vehicle buffet data. This assessment used a combination of unsteady pressure-sensitive paint (uPSP) and a dynamic loads balance to investigate the potential of these innovative and emerging test techniques to more accurately predict launch vehicle buffet environments.

15. SUBJECT TERMS

Unsteady Pressure-Sensitive Paint; NASA Engineering and Safety Center; Space Launch System; Buffet Forcing Function; Computational Fluid Dynamics

16. SECURITY CLASSIFICATION OF:			17. LIMITATION OF ABSTRACT	18. NUMBER OF PAGES	19a. NAME OF RESPONSIBLE PERSON
a. REPORT	b. ABSTRACT	c. THIS PAGE			STI Help Desk (email: help@sti.nasa.gov)
					19b. TELEPHONE NUMBER *(Include area code)*
U	U	U	UU	102	(443) 757-5802